

# **Anisotropic colloids:**

**bulk phase behavior and  
equilibrium sedimentation**

---

**Cover:**

front - final configurations from simulations of hard spheres in gravity (top-left), platelets in a cubatic phase (top-right), a worm-like phase of bowls (bottom left) and dumbbells in a plastic crystal (bottom right).

back and bookmarker - a worm-like phase of bowls, showing the complete stacks.

PhD thesis, Utrecht University, the Netherlands, September 2009.

ISBN: 978-90-393-5166-6

A digital version of this thesis is available at <http://www.colloid.nl>

# **Anisotropic colloids:** **bulk phase behavior and** **equilibrium sedimentation**

---

Anisotrope colloïden  
met en zonder zwaartekracht

(met een samenvatting in het Nederlands)

Proefschrift

ter verkrijging van de graad van doctor aan de Universiteit Utrecht op gezag van de rector magnificus, prof. dr. J.C. Stoof, ingevolge het besluit van het college voor promoties in het openbaar te verdedigen op maandag 28 september 2009 des middags te 2.30 uur

door

Mattheus Antonius Theodorus Marechal

geboren op 11 augustus 1981 te Hilversum.

**Promotor:** Prof. dr. ir. M. Dijkstra

# Contents

<b>1</b>	<b>Introduction</b>	<b>1</b>
1.1	Simulations	5
1.2	Free energy calculations	6
<b>2</b>	<b>Crystallization of colloidal hard spheres under gravity</b>	<b>9</b>
2.1	Introduction	10
2.2	Model	11
2.3	Results and discussion	12
2.4	Conclusions	21
<b>3</b>	<b>On the stability of orientationally disordered crystal structures of colloidal hard dumbbells</b>	<b>23</b>
3.1	Introduction	24
3.2	Model	26
3.3	Methods and Results	26
3.3.1	Plastic crystal: hcp vs. fcc	26
3.3.2	aperiodic vs. periodic crystal	30
3.4	Summary and discussion	37
3.A	Bond switch moves at close packing	39
3.B	Off-lattice bond switch moves	40
<b>4</b>	<b>Hard dumbbells in gravity: structure and crystallization</b>	<b>43</b>
4.1	Introduction	44
4.2	Model	46
4.2.1	Initial configuration	47
4.2.2	Bond switch moves	49
4.3	Methods	50
4.4	Results	51
4.4.1	Structure	51
4.4.2	Crystallization	54
4.4.3	Plastic crystal: hcp or fcc?	60
4.5	Summary and discussion	63
<b>5</b>	<b>Phase behavior and structure of a new colloidal model system of bowl-shaped particles</b>	<b>65</b>
5.1	Introduction	66
5.2	Experiment	67

5.3	Simulation methods	68
5.3.1	Model	68
5.3.2	Fluid phase	69
5.3.3	Columnar phases	70
5.3.4	Crystals	71
5.4	Results	73
5.4.1	Stacks	73
5.4.2	Packing	76
5.4.3	Free energies	80
5.4.4	Phase diagram	80
5.5	Summary and discussion	82
5.A	Overlap algorithm	84
<b>6</b>	<b>Phase behavior of cusp-free platelets</b>	<b>87</b>
6.1	Introduction	88
6.2	Model	88
6.3	Methods	89
6.4	Results	91
6.5	Summary	97
	<b>References</b>	<b>99</b>
	<b>Summary</b>	<b>104</b>
	<b>Samenvatting voor een breder publiek</b>	<b>106</b>
	<b>Acknowledgements</b>	<b>110</b>
	<b>Curriculum Vitae</b>	<b>112</b>

---

## Introduction

---

According to textbook definitions, colloids are particles within a size range of a nanometer to a micron that are moving around in a solvent. Surprisingly many user products fall under that definition: Milk, latex paint, mayonnaise and ice creams, to name just a few. Obviously, a better understanding of colloids could improve some of these products. Aside from these applications, colloids are also useful to gain fundamental understanding of atomic systems. As Perrin [1] showed, the motion of the colloids is caused by collisions with the molecules of the solvent, which cause the colloids to move in an irregular fashion, so called Brownian motion. This actually proved the existence of atoms and molecules, the first (and probably still foremost) fundamental insight into atoms that was gained by studying colloids. The Brownian motion allows the particles to explore phase space and find the most favorable configurations, as described by the same statistical physical theories that were derived for atoms. For example, for colloids hydrostatic equilibrium holds in the same way that it does for air molecules, except that according to Archimedes' principle, the mass is reduced (to the buoyant mass  $m_B$ ) by the mass of the volume of solvent that a particle displaces. At large altitudes the number density profile ( $\rho(z)$ ) of the colloids follows the barometric height formula,

$$\rho(z) = \rho_0 \exp(-m_B g z / k_B T), \quad (1.1)$$

where  $z$  is the height in the sample,  $g$  is the gravitational acceleration,  $k_B$  is Boltzmann's constant,  $T$  is the temperature and  $\rho_0$  is an (unknown) prefactor. This expression holds only when the colloids are acting like an ideal gas, when the density is sufficiently low i.e. at sufficiently large heights. Using this expression Perrin [2] was able to calculate a fundamental property of atoms from the number density of colloids as a function of height: Boltzmann's constant and therefore Avogadro's number. This example also shows one of the major advantages over studying colloids as atoms rather than atoms themselves: the number density of the colloids was measured simply by counting the colloids under a microscope. Although microscopes have advanced a lot since Perrin's days, the fact still remains that colloids are observable under a light microscope, while atoms are not.

Another advantage of colloids over atoms, is the tunability of the colloid-colloid interactions. Colloids, as a rule, are charged objects, since the surface of a colloid always absorbs some charged molecules and, as is also often the case, some ions (usually protons)

dissociate from the surface. The (counter) ions in the solvent, screens the bare Coulomb colloid-colloid interactions, making them decay (slightly faster than) exponentially:

$$\phi(r) = \epsilon \frac{\exp(-(r - \sigma)/l_D)}{r}, \quad (1.2)$$

where  $\epsilon$  is the strength of the interaction,  $l_D$ , is the decay length of the charged induced interactions, often called the screening length or the Debye length,  $r$  is the distance between the colloids and  $\sigma$  is their diameter (this expression holds only for spherical colloids). By adding or removing ions, the screening length can be tuned and by changing the charge of the particle,  $\epsilon$  can be tuned. In fact, for interactions between two particles of a different type, one positively and one negatively charged,  $\epsilon$  can be negative. Furthermore, there are numerous other interactions which can be added, for instance attractive tunable range interactions by adding non-adsorbing polymers and even type-specific interactions by attaching carefully selected strands of DNA to the surface of the particles. In the present thesis however, we study colloids for which most of the interactions are removed: our model particles interact via hard-core interactions, that is, interactions that only prevent the particles from interpenetrating. Hard spheres have been a favorite model for theoreticians and simulators alike, because it is a system which only depends on packing fraction (the volume of the particle times the number of particles per unit volume or the fraction of the volume that is filled by the particles). The phase behavior of hard spheres is well known: The stable phase is a fluid up to a volume fraction,  $\phi \equiv vN/V = 0.494$  and a crystal for volume fractions above 0.545 [3–5], where  $v = \pi\sigma^3/6$  is the volume of a colloid and  $N$  is the number of particles in a volume  $V$ . In between these packing fractions, there is coexistence between the fluid and the crystal phase. The type of crystal has been under debate for a long time, until it was proven that the stable crystal is the face-center-cubic crystal (FCC) using computer simulations [6]. However, the difference in stability between FCC and the other candidate, hexagonally close packed (HCP), is so small, that even relatively large crystallites will usually consist of almost equal mixtures of FCC and HCP. Hard spheres can be used as a zeroth order approximation to the interactions between atoms. In principle, interactions can then be added a posteriori using some form of perturbation theory. With colloids, this highly theoretical model particle can actually be obtained experimentally. By adding many screening ions, and by coating the surface of the colloids with an uncharged polymer brush, the particles can interact (almost) hard core-like over a distance that is larger than the screening length. In this case, it is important to adjust the refractive index of the solvent to match the refractive index of the colloids and hence minimize the Van der Waals attractions. At high salt conditions, the interaction decays so fast, that  $\phi(r)$  is essentially zero when  $r$  is larger than a certain distance  $\sigma_{\text{eff}}$ , and infinity for  $r < \sigma_{\text{eff}}$ . In other words, even if no polymer brush is present, the colloids can be made to interact almost like hard spheres with a certain effective diameter  $\sigma_{\text{eff}}$ .

Since a spherical colloid can be used as a model for a single atom, a next step in complexity is the study of colloidal molecules. The simplest molecule is a dimer, such as nitrogen, and its model colloid is the dumbbell, a pair of fused spheres whose center-to-center distance is smaller than their diameter. The synthesis of these particles is briefly considered in Chapters 3 and 4, which are dedicated to simulations of hard dumbbells.

One can keep on adding more (fused) spherical cores obtaining trimers, quadrumers etc. Furthermore, one can also go to more complex shaped colloids, which cannot be thought of as a collection of (overlapping) spheres. Colloidal particles have been synthesized in an incredibly large variety of shapes: disks, rods, crosses, bowls, capsules, icecones, snowmen, etc. In this thesis we perform simulations on a few of those shapes: as mentioned, dumbbells in Chaps. 3 and Chap. 4, bowls in Chap. 5 and finally discs in Chap. 6. The molecular analogs of these are the nitrogen molecule, molecular bowls and molecular discs, where the last two are applied in the field of molecular liquid crystals. Liquid crystals

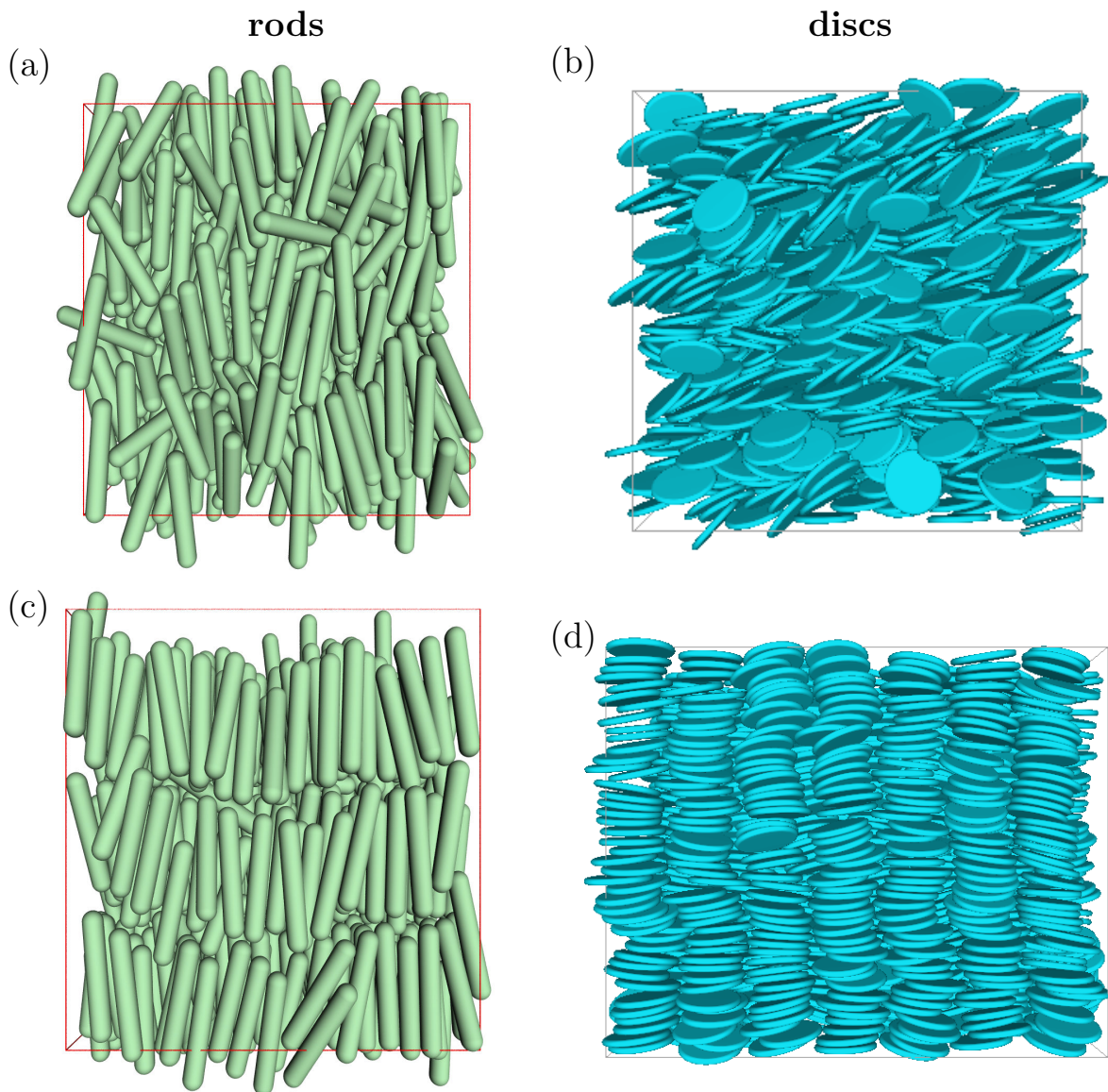


**Figure 1.1:** Configurations of liquid crystals: Nematic phases formed by rods (a) and discs (b). When the packing fraction is increased, the nematic phases of rods and discs transform into the smectic (c) and columnar (d) phases respectively. We study discs in Chap. 6; rods have been studied extensively in previous work [7].

are phases that are somewhere in between a liquid and a crystal phase, because there is ordering in one or more of the spatial or orientational degrees of freedom of the particles, while other degrees of freedom are fluid-like. Examples are the nematic phase, where the particles are aligned, but free to translate, the smectic phase in which the particles are aligned and confined to layers, but the movement within the layers is fluid-like, and the columnar phase, where particles are aligned and confined to (usually) hexagonally arranged columns, but there is no ordering within the column. Sufficiently thin discs exhibit nematic and columnar liquid crystal phases, as described in Chap. 6, while the liquid crystalline phase behavior of the bowls is restricted to the columnar phase (see Chap. 5). Typical configurations of nematic and smectic phases of rods and nematic and columnar phases of discs are shown in Fig. 1.1.

One aspect of colloids is not yet explicitly mentioned, but which was implicit in the experiment of Perrin. Perrin could do his experiments on a sample cell with a height of a tenth of a millimeter. If he would have done his experiments on atoms, (were he able to see them), he would have to have a sample container which is higher than the decay length of the barometric height profile,  $k_B T / mg \simeq 10\text{km}$  for air molecules, which would never have fit inside his laboratory. For micron sized colloids on the other hand,  $k_B T / m_B g$  is about a micron. The buoyant mass of the colloids,  $m_B$ , is equal to the volume of a colloid times the difference between the mass density of the constitutive material of the colloid and the mass density of the solvent,  $\Delta\rho$ , for which we took  $\Delta\rho \simeq 1\text{kg/l}$ . Although, smaller colloids can easily be synthesized, the individual colloids become more difficult to distinguish when they become much smaller than a micron, as Perrin already mentioned in Ref. [1]. By carefully choosing the solvent and the colloidal material, one can lower the mass density difference by one or two orders of magnitude. However, the gravitational length will never become much larger than a hundred times the diameter of the colloid; it is usually smaller than the height of the container. Therefore, gravitational effects will always be important for experiments on micron-sized colloids on earth (there have been a few experiments on colloids in space precisely for this reason). Here, we see the advantage of simulations: we can selectively turn the gravitational field on and off, allowing us to first study the phase behavior in the absence of gravity as was done in previous work for hard spheres and in Chap. 3 for hard dumbbells. Subsequently, we can turn the gravitational field on, and study both hard spheres (see Chap. 2) and hard dumbbells (Chap. 4) under gravity.

Our method of choice to study colloidal particles is computer simulations. For atoms the disadvantages of simulations, notably that one can simulate only a limited number of particles (up to a few hundred thousand at present) for a short time (up to nanoseconds), are made up for by the fact that more information, such as the positions of the individual atoms, can be obtained in simulations than in experiments. Colloids, unlike atoms, can be tracked in real space and hence their positions can be obtained. However, the tunability of colloids, that was mentioned in the previous section, also has its disadvantages: Even for simple charged colloidal spheres, quantities like the diameter, charge, screening length and even packing fraction all need to be measured (resulting in uncertainties), while for simulations these are input parameters. This fact has been exploited in Ref. [8], where the interaction potential of a colloid has been obtained by fitting simulation results of hard spheres that also interact with the potential (1.2) for various  $\epsilon$  to the experimental

results. A well known expression can then be used to obtain the (effective) charge of the colloids. The limited time window of the simulations is much less an issue for colloidal systems because colloids move much slower than atoms, such that, for instance, systems of (not too many) micron-sized colloids can be simulated almost real time. Finally, computer simulations can be run on a fast personal computer, while experiments usually require a set up, that is quite a bit more expensive to acquire and maintain. Nevertheless, simulations and experiments (and theory) can not function separately for colloidal systems, (which can be seen from the many joint publications) since experiments often require simulations and theory to understand the fundamental processes that occur, while simulations and theory need verification from experiments.

In this thesis, we will be interested mainly in the phase behavior of anisotropic colloids. The rest of this introductory chapter is reserved for a brief introduction into the simulations methods and free energy calculations we performed. In Chap. 2 we will first study hard spheres in gravity. In the next chapter we will study our first anisotropic model particle, the hard dumbbell. The insights gained in these two chapters will be used in Chap. 4, which is dedicated to hard dumbbells in gravity. We will then proceed to study the bulk phase behavior of hard bowls in Chap. 5 and compare to experimental results, which we will also briefly describe. Finally, in Chap. 6 we will calculate the phase diagram of a cusp-free model for platelets or discs.

## 1.1 Simulations

In this section we will give a short introduction to the two simulation methods we have used in this thesis. Almost all of the work has been done using Monte Carlo simulations, although in Chap. 6 molecular dynamics has also been used. In statistical physics of continuously moving particles a static quantity  $A$  i.e. a quantity that does not depend on the momenta of the particles, is measured by the following integral:

$$\langle A \rangle = \int d\mathbf{r}^N A(\mathbf{r}^N) e^{-\beta\Phi(\mathbf{r}^N)} / \mathcal{N}, \quad (1.3)$$

where  $\mathbf{r}^N$  are the positional and (in the case of anisotropic colloids) angular coordinates of all particles,  $\beta = 1/k_B T$ ,  $\Phi$  is the potential energy of the system and  $\mathcal{N}$  is a normalization factor:  $\mathcal{N} = \int d\mathbf{r}^N \exp(-\beta\Phi(\mathbf{r}^N))$ . In principle, this integral can be evaluated using so-called Monte Carlo integration: Values for all coordinates of the particles are generated that are distributed randomly over the whole phase space. The integrands of Eq. (1.3) and  $\mathcal{N}$  are summed over all these trial configurations until sufficient precision is achieved for Eq. (1.3). For many systems though, the exponent in the integrand is very small for most of the randomly generated  $\mathbf{r}^N$  and only a few terms will give an appreciable contribution to the integral Eq. (1.3). An example is a dense fluid of hard spheres, where almost all of the randomly generated configurations will cause an overlap and therefore have a zero contribution to the integral. The solution to this problem, is to sample phase space according to the Boltzmann probability  $\exp(-\beta\Phi(\mathbf{r}^N))$ , by so-called Metropolis sampling. In this method the phase space is explored by performing so-called Monte Carlo moves. In such a move, the state of the system, characterized by the coordinates  $\mathbf{r}_o^N$  ( $o$  stands for “old”), is changed slightly, usually by displacing or rotating a single particle by a

small amount. Thus a new state  $\mathbf{r}_n^N$  is created, which is accepted or rejected with the probability

$$\max \left\{ 1, \exp \left( -\beta [\Phi(\mathbf{r}_n^N) - \Phi(\mathbf{r}_o^N)] \right) \right\}. \quad (1.4)$$

If the new state is rejected, it is replaced by the old state. It can be shown that an ensemble of configurations that was Boltzmann distributed, remains Boltzmann distributed after successive application of Monte Carlo moves, and even that a poorly chosen initial configuration will be converted into a Boltzmann distributed ensemble by these moves. In our simulations, integral (1.3) is evaluated simply by averaging  $A(\mathbf{r}^N)$  over all generated configurations  $\mathbf{r}^N$ . We will refer to this method, Monte Carlo integration combined with Metropolis sampling, as Monte Carlo simulation (MC) in the remainder of this thesis.

One might think that the above method is overly complicated, as the motion of the particles is described by Newton's laws. The corresponding equations of motion can be integrated numerically to obtain the trajectories of all particles. This method is called molecular dynamics (MD) and is also widely used in computer simulations. The integration of the equations of motion is usually stepwise, where the positions and velocities of the particles at a certain time  $t$  are obtained from the positions and the velocities at a time  $t - \Delta t$ , where  $\Delta t$  is the fixed time step, that is used in the discretization of the equations of motion. For hard particles, this way of integrating the equations of motion breaks down, because the forces are only nonzero during the instantaneous collisions. These collisions will in general not occur at the time of an integration step, so they will be missed, leading to overlaps. Instead, we take a different route, where the positions and velocities only need to be evaluated at the time of a collision event. For every pair of particles, we look for a collision by moving the particles forward using the known analytical free motion until a collision is found. For hard spheres the prediction of the time of a collision is analytical, for anisotropic particles that rotate, the collision must be sought numerically (see Chap. 6 for more details on this numerical search). We then sort the collisions in order of the time that they occur and cycle through them one by one. After each collision the future collisions of the colliding particles need to be recalculated and reinserted into our list of collisions, in such a way that it remains time ordered. In practice, we use a binary sort tree for this purpose. Since the time advances by processing events in this type of molecular dynamics simulation, it is called an event driven molecular dynamics simulation.

## 1.2 Free energy calculations

In theory, using (event driven) MD or MC, all the measurable properties of the particles can be obtained. In this thesis, we will mainly be interested in systems that undergo phase transitions, and we wish to locate these phase transitions. In principle, we can initiate a simulation in one of the phases, change the pressure or number density and simply observe whether the system changes phase or not. Unfortunately, in order for a phase transition to occur, the system usually has to overcome a considerable free energy barrier, which is determined by the interfacial free energy required to create an interface between the coexisting phases. Or, in other words, the states on the path through phase space, that connects the two phases, are exceedingly rare. For crystallization in gravity,

this is not such a large problem because the flat wall at the bottom of our sediments promotes layering, which is a first step in crystallization in this system. In the absence of such a wall, we can usually not directly determine the transition point. Instead, we calculate the chemical potential  $\mu$  and the pressure  $P$  of both phases, and we find the pair of densities at which the chemical potentials and the pressures of the respective phases are equal. We can calculate the chemical potential in a single simulation, but only when the number density is low [9]. This method was used for the isotropic fluid to nematic phase transition of discs in Chap. 6. For higher densities, we need some way of calculating the free energy,  $F = U - TS$ , where  $U$  is the energy of the system,  $T$  is the temperature and  $S$  the entropy. The chemical potential can then be obtained using  $\mu = (F + PV)/N$ . Usually, only free energy derivatives can be measured in Monte Carlo and molecular dynamics simulations. The exceptions are the simulations that have been biased to allow the system to go through the gateway states that lie in between the two phases: umbrella sampling, Wang Landau sampling, and multicanonical Monte Carlo. In these simulations one can measure how often the simulation is in one of the two phases compared to the other phase, which is proportional to the free energy difference between the phases. We used multicanonical Monte Carlo simulations to calculate the free energy difference between the FCC and the HCP stacking of a plastic crystal phase of dumbbells in Chap. 3. In all other cases, we relate the free energy of a phase to the free energy of a reference state, usually a noninteracting variant of the phase of interest or the phase that coexists with the phase of interest. Suppose that there is a path through parameter space that connects the phase of interest to this reference state and that we can parametrize this path by a parameter  $\lambda$ , where  $\lambda = 0$  denotes the reference state and  $\lambda = 1$  the state of interest (for details about the integration paths we employed, see for instance Chap. 3). Then, the free energy of the state of interest  $F_1$  can be related to the free energy of the reference state  $F_0$  by

$$F_1 = F_0 + \int_0^1 d\lambda \frac{\partial F_\lambda}{\partial \lambda}, \quad (1.5)$$

where we measure  $\partial F_\lambda / \partial \lambda$ , the derivative of the free energy with respect to  $\lambda$ , in our simulations for many values of  $\lambda$  along the path. Therefore, to calculate a phase diagram, in which the coexistence densities are plotted against the aspect ratio of an anisotropic colloid, many simulations have to be run, to calculate the free energy derivatives at a sufficient number of points along the various integration paths.



---

## Crystallization of colloidal hard spheres under gravity

---

Using grand canonical Monte Carlo simulations, we study the crystallization of colloidal hard spheres under gravity. More specifically, we investigate the nature of the freezing transition as a function of gravity and chemical potential of the hard spheres. We find a discontinuous freezing transition where several fluid layers close to the bottom of the sample freeze simultaneously, i.e. at the same chemical potential. We also find that the number of layers that freezes at the same chemical potential decreases for higher gravitational field strength. Upon increasing the chemical potential further, the crystalline film thickness increases continuously.

## 2.1 Introduction

The bulk phase behavior of hard spheres has been studied in great detail and is well-understood by now. In particular, it was shown by computer simulations that such a system shows a purely entropy-driven phase transition from a disordered fluid phase to a face-centered-cubic (fcc) crystal phase at sufficiently high densities [3–5]. Although the fcc phase is the most stable phase, the free energy difference with respect to the metastable hexagonal-close-packed (hcp) structure is only very small and is on the order of  $10^{-4}k_B T$  per particle at the melting transition [6]. Here we define  $k_B$  as Boltzmann’s constant and  $T$  the temperature. The crystallization of hard spheres at flat walls has also been subject of many studies. It has been shown that a smooth hard wall causes pronounced layering of the fluid phase at the wall, which can lead eventually to prefreezing and complete wetting by the hard sphere crystal upon increasing the density towards bulk coexistence [10–12]. Confining the hard-sphere system between two parallel hard walls leads to an intriguing sequence of capillary freezing and capillary melting transitions upon increasing the distance between the two walls and the formation of many different crystal structures like square, triangular, rhombic, buckling and prism phases [13, 14]. Prefreezing [15] and epitaxial crystal growth [15, 16] was also observed for walls with a surface pattern that is similar in symmetry as one of the crystal planes. Using templates that are characteristic for the hcp crystal structure, i.e., templates that induce the ABAB stacking of the hexagonal layers perpendicular to the wall, the hcp crystal, that is metastable in bulk, has been grown experimentally in suspensions of colloidal particles [17, 18]. These suspensions can serve as excellent experimental realizations of the hard-sphere system as the effective interactions of the colloids can be tuned in such a way that the particles interact approximately as hard spheres. However, gravity is often non-negligible in colloidal suspensions, as the gravitational energy becomes comparable to the thermal energy for colloid sizes of about a micrometer. Hence, a spatial inhomogeneous suspension is obtained due to the gravitational field, which is characterized by a density profile  $\rho(z)$  that varies with altitude  $z$ . The parameter that is associated with a gravitational field is the so-called gravitational length and reads  $\ell/\sigma = (\beta m g \sigma)^{-1}$  where  $m$  is the effective or buoyancy mass of the colloidal particles,  $\beta = (k_B T)^{-1}$ ,  $\sigma$  the diameter of the colloids, and  $g$  the gravitational acceleration. Typically,  $\ell/\sigma$  is of the order of  $10^{-1} - 10^3$  for colloidal particles. The density profile  $\rho(z)$  follows from a competition between minimal energy (all colloids at the bottom) and maximum entropy (a homogeneous distribution in the available volume). In the case of a very dilute colloid concentration or at high altitude, where the suspension becomes sufficiently dilute, the system behaves like an ideal gas and the system obeys the Boltzmann distribution, yielding an exponential density profile with a decay length given by  $\ell$ . In 1910, Jean Perrin measured such a density profile under the microscope which enabled him to determine Boltzmann’s constant and hence, Avogadro’s number [2]. However when the interactions become important, the density profile becomes highly non-exponential. Density profiles for hard spheres have been calculated using density functional theory and simulations [19–26], and are measured by light scattering techniques [27, 28] and confocal microscopy in suspensions of colloidal hard spheres [29]. The measured concentration profiles obtained from a single experiment or simulation can be inverted to obtain the osmotic equation of state over a whole range

of densities [19, 27, 28, 30]. Crystallization in sedimentation profiles of hard spheres was studied using Monte Carlo simulations and density functional theory [20–24, 26]. The simulations in Ref. [20] show a discontinuous transition where two layers crystallize at the same gravitational field strength. Upon increasing the gravitational field further, the crystalline film grows continuously. However, density functional theory predicts a discontinuous crystal growth via layering transitions upon increasing gravity in contrast with the simulation results [20].

In this chapter we investigate in more detail the nature of the freezing transition in suspensions of hard spheres as a function of chemical potential while keeping the gravitational field strength fixed. In Ref. [20], crystallization was studied as a function of gravity. However, in order to study the phase behavior of colloids in an external field, it is more convenient to treat the system grand-canonically and to study the freezing transition as a function of chemical potential for a fixed value of the gravitational field strength [31]. Moreover, keeping the gravitational length of the particles fixed is closer to the experimental situation as the experimental  $\ell$  is determined by system parameters that are often constant in an experiment. To be more specific,  $\ell$  depends on the gravitational acceleration, which is often equal to the value on earth, and on the buoyancy mass  $m$ , which is related by Archimedes' principle to  $m = m_0 - \tilde{\rho}v$  with  $\tilde{\rho}$  the mass density of the solvent,  $m_0$  the bare mass of the colloidal particles, and  $v$  the particle volume. Our results show a discontinuous freezing transition where a number of layers freezes at the same chemical potential. Upon increasing the chemical potential further, the crystalline film thickness increases continuously. It is important to stress that Monte Carlo simulations gives only information about the equilibrium structure and not on the crystallization kinetics. The chapter is organized as follows. In Sec. 2.2 we describe the model. In Sec. 2.3, we present our Monte-Carlo simulation results and we end with some concluding remarks in Sec. 2.4.

## 2.2 Model

We consider a system of hard spheres with diameter  $\sigma$  in a gravitational field oriented along the  $z$ -direction. In addition, the spheres are confined between two smooth hard parallel walls at  $z = 0$  and  $z = H$ . The spheres are subjected to the external potential:

$$\phi(z) = \begin{cases} mgz & \sigma/2 \leq z \leq H - \sigma/2 \\ \infty & \text{otherwise} \end{cases} \quad (2.1)$$

where  $z$  is the vertical coordinate,  $g$  is the gravitational acceleration, and  $m$  the buoyant mass of the hard spheres. The height  $H$  is chosen such that the density at  $z = H - \sigma/2$  is sufficiently small, i.e.,  $\rho\sigma^3 < 10^{-6}$  and thus the system can be considered to be infinite in the  $z$ -direction. The lateral dimensions of the box are  $L_x = 9 a_0 n$  and  $L_y = 10 a_0 n\sqrt{3}/2$  with  $n$  an integer. Note that the lateral dimensions of the simulation box are nearly equal, which minimizes the finite-size effects for the fluid phase and accommodates a hexagonal crystalline layer (the (111) plane of a fcc crystal) with lattice constant  $a_0$ . We employ periodic boundary conditions in the lateral dimensions and we use  $n = 2$  in our simulations.

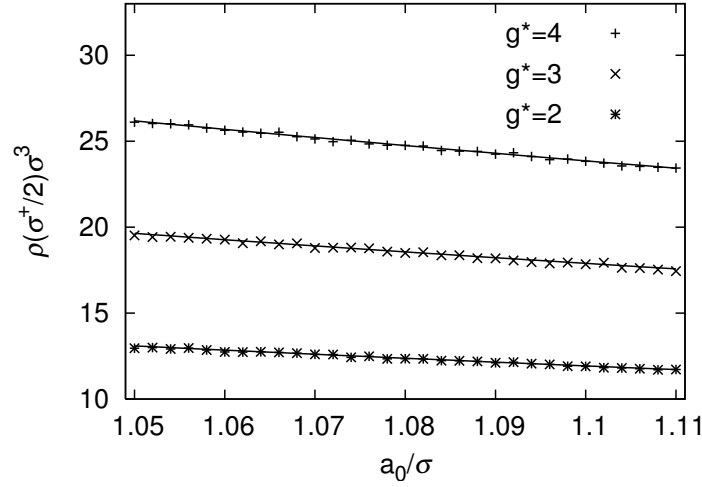


**Figure 2.1:** The contact density  $\rho(\sigma^+/2)\sigma^3$  of a crystalline sediment of hard spheres as a function of the lattice constant  $a_0$  of the crystal at the bottom of the sample for varying gravity  $g^* = mg\sigma/k_B T = 2, 3$ , and  $4$ . The error in the data is smaller than the size of the symbols. The solid lines denote the pressure at the bottom of the sample given by  $\beta P(z=0)\sigma^3 = g^* \rho_A^*$ , where  $\rho_A^* \equiv N\sigma^2/A$ .

## 2.3 Results and discussion

First, we perform Monte Carlo (MC) simulations in the canonical ensemble, i.e., we fix the number of particles  $N = 2004$ , the area  $A \equiv L_x \times L_y = 18a_0 \times 10\sqrt{3}a_0$  in the  $x$ - and  $y$ -direction, and the height  $H$  of the box. Moreover, we fix the strength of the gravitational field or the inverse gravitational length  $g^* \equiv mg\sigma/k_B T = (\ell/\sigma)^{-1}$ . The thermodynamic parameter that was defined in Ref. [20] is the mean area  $\rho_A^* \equiv N\sigma^2/A$ , which equals the number of particles per unit area of the bottom of the sample. The pressure at the bottom of the sample, i.e., at  $z = 0$ , is directly related to  $\rho_A^*$ , as the pressure is determined by the gravitational force of all the spheres per unit area, i.e.,  $\beta P(z=0)\sigma^3 = g^* \rho_A^*$ . In our simulations, we measure the dimensionless density profile:

$$\rho(z) = \frac{1}{A} \int \int dx dy \rho(x, y, z) = \frac{1}{A} \left\langle \sum_{i=1}^N \delta(z - z_i) \right\rangle, \quad (2.2)$$

where  $\rho(x, y, z)$  is the local density and the brackets denote an ensemble average. It is well-known that for any one-component fluid or crystal near a hard wall, the contact density  $\rho(\sigma^+/2)$  satisfies the sum rule  $\rho(\sigma^+/2) = \beta P(z=0)$ . The starting configurations that we use in our simulations consist of a face-centered-cubic (fcc) crystal structure with the (111) axis normal to the bottom of the sample and with varying lattice constant  $a_0$ . In Ref. [20], the contact theorem was employed to obtain the “correct”  $a_0$  for the crystalline sediment. These authors found that the sum rule was only satisfied for a lattice constant  $a_0 = 1.088\sigma$ . In Fig. 1, we plot the contact density  $\rho(\sigma^+/2)\sigma^3$  as a function of  $a_0$  for  $g^* = 2, 3$ , and  $4$ . For comparison, we also plot  $\beta P(z=0)\sigma^3$  denoted by the solid lines. Fig. 2.1 shows that the sum rule is satisfied for all values of the lattice constants we

considered, i.e.,  $1.04 \leq a_0/\sigma \leq 1.11$ . Hence, we are not able to obtain the “correct” lattice constant by requiring consistency of the bottom pressure with the contact density.

In order to solve this problem, we perform Monte Carlo simulations in the grand-canonical ensemble, i.e., we fix the chemical potential  $\mu^* \equiv \beta\mu - \ln(\Lambda^3/\sigma^3)$ , where  $\Lambda$  is the thermal wavelength, and the volume of the box. Due to particle removals and insertions in a grand-canonical Monte-Carlo simulation, the system equilibrates more easily to the equilibrium crystal structure by relaxing the stress and strain in the crystal and adapting the lattice constant. Hence one does not have to estimate the equilibrium value for the lattice constant beforehand as in the case of Monte Carlo simulations in the canonical ensemble. Moreover, it proves more convenient to study phase behavior in inhomogeneous systems in the grand canonical ensemble in order to ensure equal chemical potential in coexisting phases [31].

We perform grand-canonical Monte-Carlo simulations for varying values of gravity  $g^* = 1, 2, 3$ , and 4. The box shape is set by  $a_0 = 1.11$  and  $n = 2$ . We checked that simulation runs with larger box sizes and different box shapes show the same results within the statistical error. The crystal can adapt itself to the “correct” lattice constant by changing slightly the crystal orientation, as can be seen in Fig. 2.4. In each Monte Carlo cycle we perform with a probability  $\mathcal{P}_{\text{exch}}$  an attempt to exchange a particle with an ideal reservoir and otherwise an attempt to displace a particle. We use  $\mathcal{P}_{\text{exch}} = 0.5$  or 0.9. The maximum displacement in each direction was 0.1 if  $\mathcal{P}_{\text{exch}} = 0.5$  and 0.2 if  $\mathcal{P}_{\text{exch}} = 0.1$ . A simulation run consists of  $1.6 \cdot 10^{10}$  ( $\mathcal{P}_{\text{exch}} = 0.1$ ) or  $8 \cdot 10^9$  ( $\mathcal{P}_{\text{exch}} = 0.5$ ) MC cycles to thermalize the system and twice as many cycles for the production runs to sample the statistical averages of interest. The number of trial moves to displace a particle was always larger than  $8 \cdot 10^5$  per particle. We study both crystallization and melting. In the first case, the initial condition is a dilute cubic crystal which melted within  $10^6$  MC cycles. We also start with an fcc crystal phase to study melting. We checked that our simulation results did not depend on the starting configuration. However, the equilibration of the system is about 10 times longer near the freezing transition.

In Fig. 2.2, we show density profiles for hard spheres in a gravitational field with strength  $g^* = 1, 2, 3$ , and 4. The profiles were averaged in bins of width  $\delta z = 0.01\sigma$ . For each  $g^*$ , we show density profiles at  $\mu^* = 14$ , at a value of  $\mu^*$  just above the freezing transition of the first layer, and at  $\mu^* = 25$ . At  $\mu^* = 14$ , we find density profiles of a liquid phase with pronounced layering of the fluid phase at the lower wall. Upon increasing  $\mu^*$  just above the value at the freezing transition of the first fluid layer, we observe the formation of crystalline layers at the bottom:  $\rho(z)$  drops to zero between the density peaks close to the wall. At  $\mu^* = 25$ , we find for all  $g^*$  the formation of several crystalline layers at the wall. From Fig. 2.2 we observe that the number of crystalline layers decreases upon increasing  $g^*$  at fixed  $\mu^*$ . This trend is to be expected since an infinite number of crystalline layers are expected to be formed for zero gravity and a chemical potential  $\mu^*$  fixed at its bulk value, i.e.,  $\mu_{\text{coex}}^* = 16.071$ .

We now take a closer look at the crystallization of the fluid layers at the bottom wall.

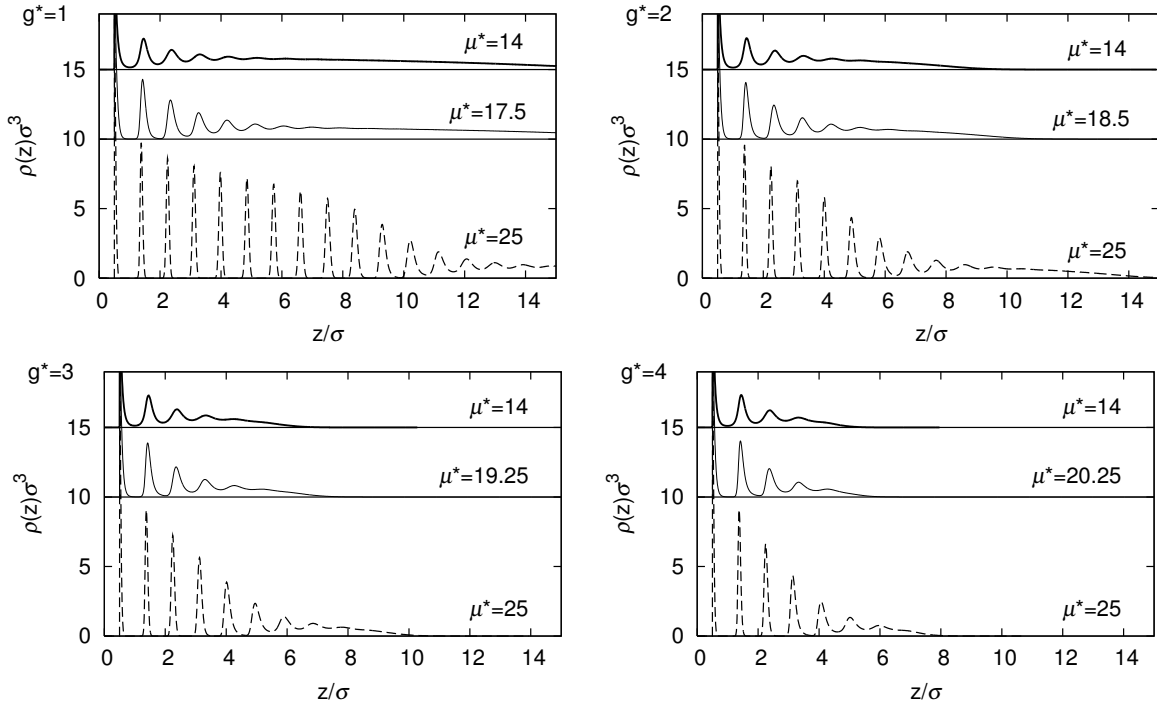


**Figure 2.2:** Density profiles  $\rho(z)$  for hard spheres in a gravitational field with strength  $g^* = 1$  (top, left), 2, 3, and 4 (bottom, right). For each  $g^*$ , density profiles are shown for a fluid phase ( $\mu^* = 14$ , thick solid line), just above the freezing transition of the first layer ( $14 \leq \mu^* \leq 25$ , thin solid line), and a fluid with crystalline layers at the bottom ( $\mu^* = 25$ , dashed line). The results are shifted vertically for clarity of display.

To this end, we measure the hexagonal bond order parameter profile:

$$\psi_6(z) = \frac{\left| \left\langle \sum_{i=1}^N \psi_{6,i} \delta(z - z_i) \right\rangle \right|}{\left\langle \sum_{i=1}^N \delta(z - z_i) \right\rangle}. \quad (2.3)$$

Here the hexagonal bond order parameter of particle  $i$  is defined as

$$\psi_{6,i} = \frac{1}{N_i} \sum_{j=1}^{N_i} e^{6i\theta_{ij}}, \quad (2.4)$$

where the sum over  $j$  is over the  $N_i$  nearest neighbors of particle  $i$ ,  $\theta_{ij}$  is the angle between  $\mathbf{r}_{ij} \equiv \mathbf{r}_i - \mathbf{r}_j$  and some arbitrary axis in the horizontal plane and  $i$  (without dot) is the imaginary number. Particles  $i$  and  $j$  were considered nearest neighbors when they satisfied  $x_{ij}^2 + y_{ij}^2 + 4z_{ij}^2 < (1.3a_0)^2$ . Due to the factor 4, this condition preferably selects nearest neighbors, which lie within one layer. Examples are plotted in Fig. 2.3 for the same state points as in Fig. 2.2. For  $\mu^* = 14$ , we find a flat hexagonal bond order parameter profile, i.e.,  $\psi_6(z) = 0$  for all values of  $z$ . For a value of  $\mu^*$  slightly above the freezing transition of the first layer, we observe clearly that the first and second layer crystallize at the same chemical potential for all values of  $g^*$  considered here. We also find a discontinuous jump

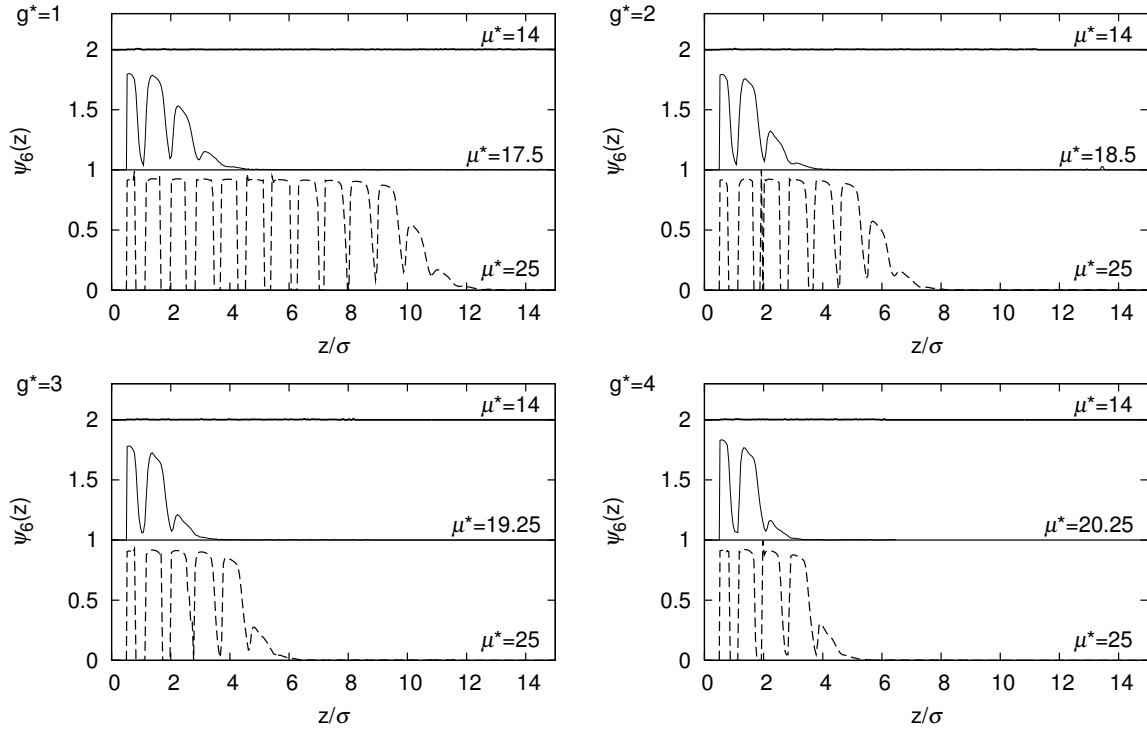


**Figure 2.3:** Hexagonal bond order parameter profiles  $\psi_6(z)$  for hard spheres in a gravitational field. Profiles are shown for the same state points as in Fig. 2.2. The results are shifted vertically for clarity of display. For  $\mu^* = 14$ , we find  $\psi_6(z) = 0$ .

in the hexagonal bond order of the third layer at this chemical potential, although the jump is much smaller than that of the first two layers. The jump in  $\psi_6$  of the third layer increases upon decreasing  $g^*$ . Upon increasing  $\mu^*$  further, the hexagonal bond order  $\psi_6$  of the  $n$ -th layer with  $n \geq 3$  increases continuously within each layer. First, the layer is fluid-like, i.e.,  $\psi_6$  is low. As  $\mu^*$  increases, we observe the presence of crystallites, which merge and form a crystal with many defects upon further increase of  $\mu^*$ . At very high chemical potential, the defects will be annealed out, resulting in a high value of  $\psi_6$ . In Fig. 2.4, we show typical configurations of the third layer of a fluid of hard spheres in a gravitational field with strength  $g^* = 4$  and increasing values of  $\mu^*$ .

The  $n$ th maximum of  $\psi_6$  is a measure for the crystalline order in the  $n$ th layer. These maxima are plotted for the first six layers in Fig. 2.5. Again our results suggest a discontinuous freezing transition of the first two layers at the same chemical potential, and, upon increasing  $\mu^*$ , additional layers crystallize continuously. We also observe a discontinuous jump in  $\psi_6$  of the third layer at the same  $\mu^*$ . If we adopt the criterion that a layer is crystalline if  $\psi_6(z_n) > 0.5$  with  $z_n$  the  $n$ th local maximum of  $\psi_6(z)$ , we can conclude that the number of layers that freeze at the same chemical potential equals 3 for  $g^* = 1$  and 2 for  $g^* = 2, 3$ , and 4. Our results show that the number of layers that crystallizes simultaneously, i.e. at the same  $\mu^*$ , increases for decreasing  $g^*$ . As already mentioned before, this finding can be explained by the fact that an infinite number of crystalline layers will be formed at zero gravity and at a chemical potential equal to its bulk value  $\mu_{\text{coex}}^*$ . It is tempting to argue that for low  $g^*$  three or more layers will crystallize at the

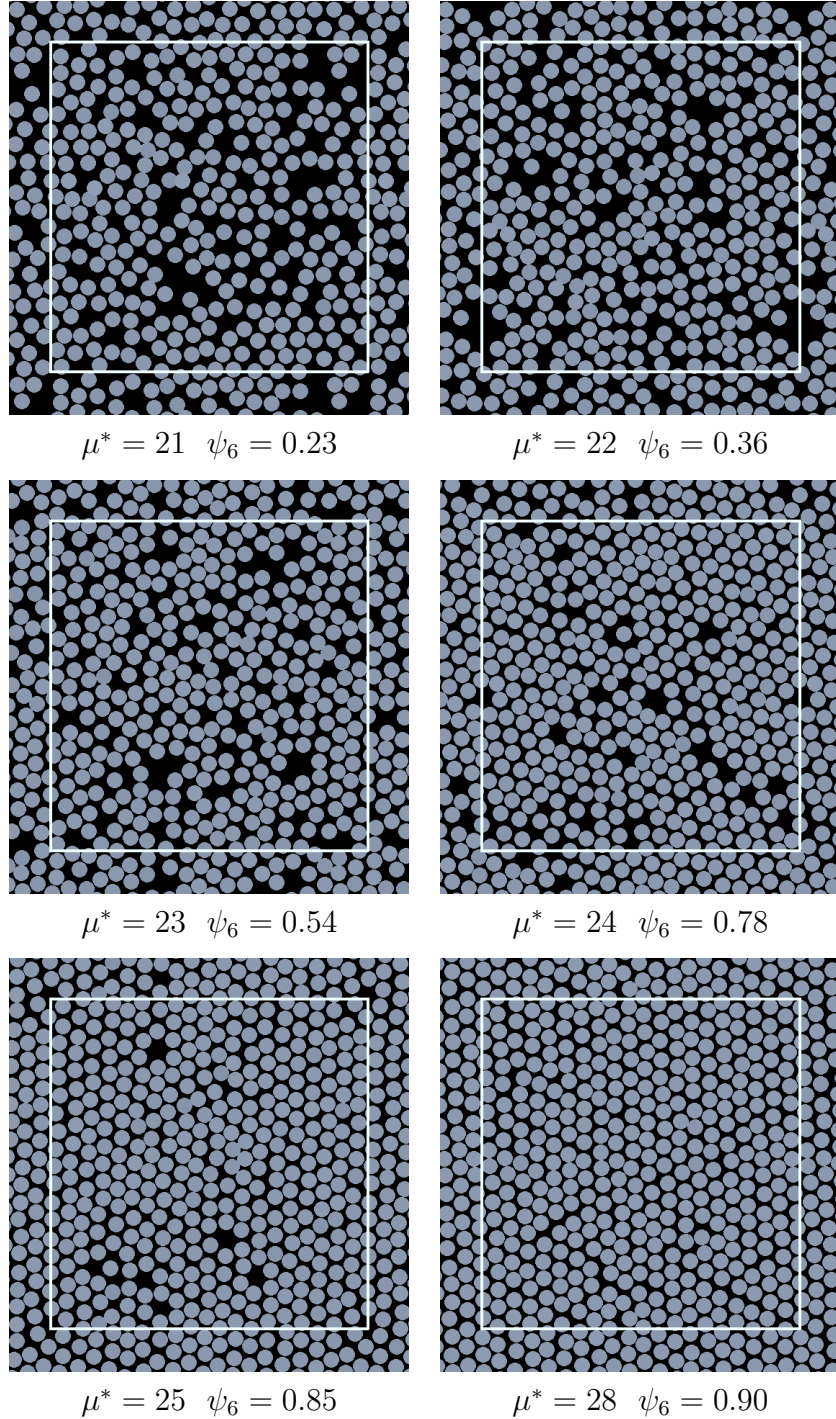


**Figure 2.4:** Typical configurations of the third fluid layer in a system of hard spheres in a gravitational field with strength  $g^* = 4$  at varying values of the chemical potential. The white rectangle denotes the horizontal box area. Some periodic images of the particles are shown as well.

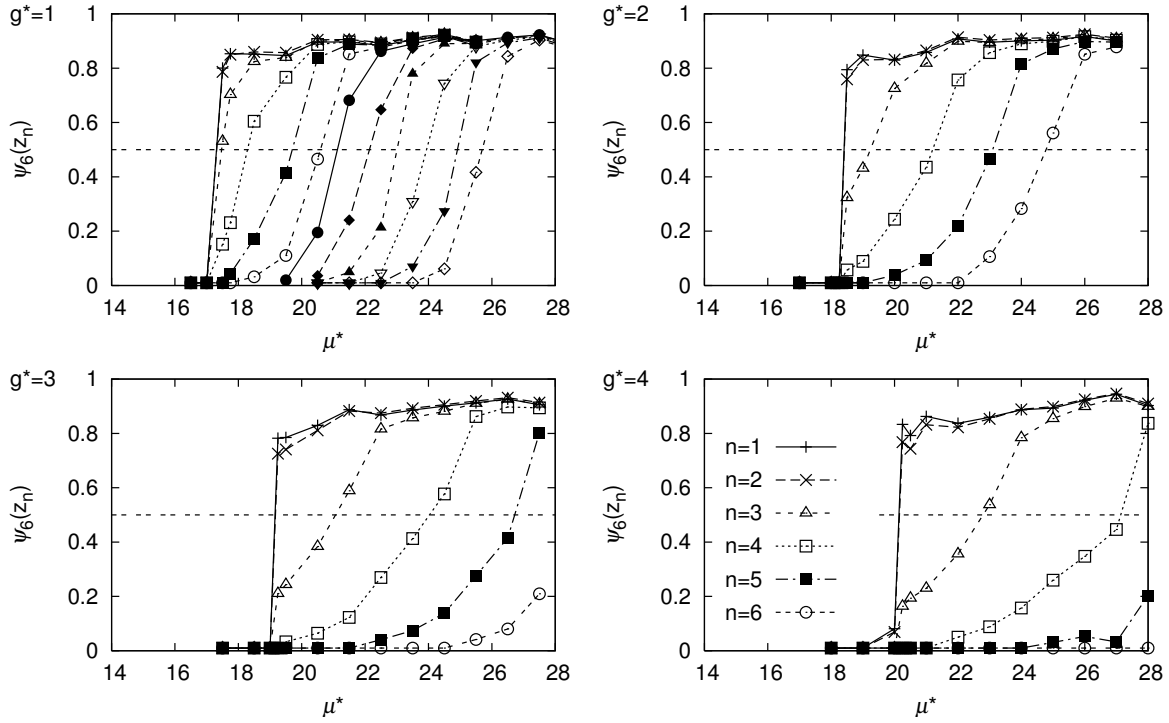


**Figure 2.5:** The maximum hexagonal bond order parameter in the  $n$ th layer as a function of chemical potential  $\mu^*$  for a system of hard spheres in a gravitational field with strength  $g^* = 1, 2, 3$ , and  $4$ . The horizontal dashed line denotes our crystallinity criterion  $\psi_6(z_n) > 0.5$ .

same  $\mu^*$ . A natural question to ask is whether the first and second layer always crystallize at the same  $\mu^*$ .

To this end, we perform simulations at  $g^* = 10$ . The resulting density profiles are plotted in Fig. 2.6. In Fig. 2.7, we plot the maximum hexagonal bond order parameter

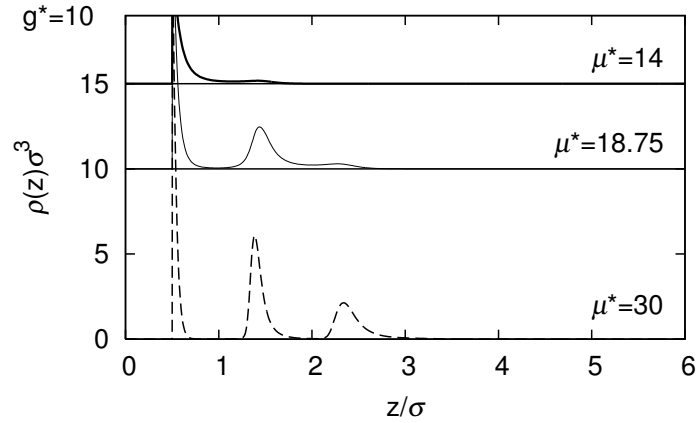


**Figure 2.6:** Density profiles  $\rho(z)$  for hard spheres in a gravitational field with strength  $g^* = 10$  at varying values of the chemical potential. The results are shifted vertically for clarity of display.

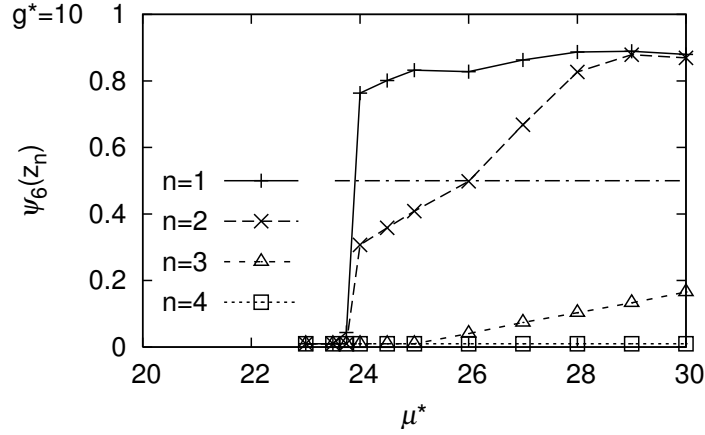


**Figure 2.7:** The maximum hexagonal bond order parameter in the  $n$ th layer as a function of chemical potential  $\mu^*$  for hard spheres in a gravitational field with strength  $g^* = 10$ . The horizontal dot-dashed line denotes our crystallinity criterion  $\psi_6(z_n) > 0.5$ .

for the first four layers as a function of  $\mu^*$ . Our results indicate a first-order freezing transition of the first layer, and a continuous freezing transition of the second and third layer at higher  $\mu^*$ . To summarize, we expect that the number of layers that crystallizes simultaneously at the same chemical potential with a first-order phase transition increases from 1 to  $\infty$  upon lowering the gravitational field strength.

In Fig. 2.8, we plot the freezing transitions for the first six layers as a function of  $g^*$  and

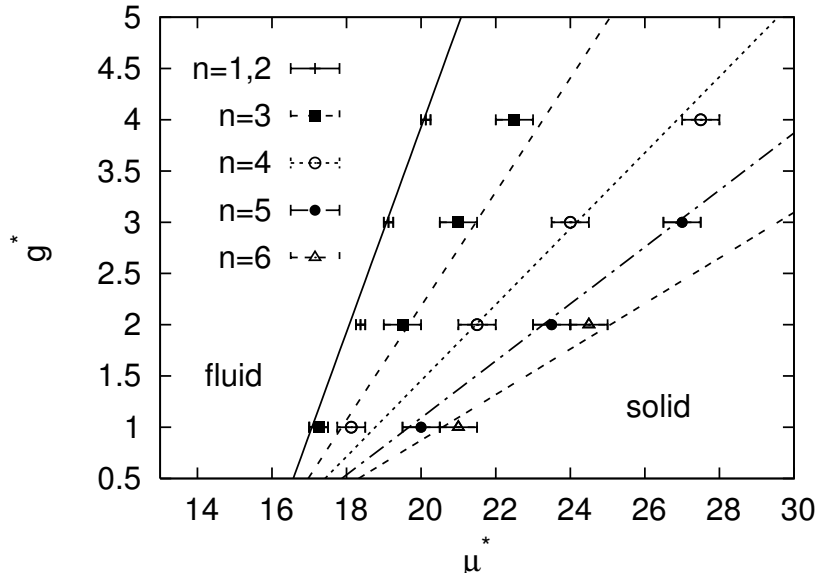


**Figure 2.8:** Phase diagram of the freezing transitions of the first six layers as a function of  $\mu^*$  and  $g^*$  as obtained from simulations (symbols). The lines denote our prediction for the freezing transitions  $\mu_{\text{int}}^*(z'_n) \simeq \mu_{\text{coex}}^* = 16.071$  with  $z'_n$  given by Eq. (2.6). The solid line denotes a first-order freezing transition, while the dashed lines denote continuous transitions.

$\mu^*$  using our crystallinity criterion  $\psi_6(z'_n) > 0.5$ . The total chemical potential at height  $z$  for a system of hard spheres in a gravitational field reads  $\mu^* = \mu_{\text{int}}^*(z) + g^*z/\sigma$ , where  $\mu_{\text{int}}^*(z)$  is the internal chemical potential i.e., the chemical potential the system would have, if there is no external potential. One expects that the fluid at height  $z$  crystallizes if  $\mu_{\text{int}}^*(z) \simeq \mu_{\text{coex}}^*$ . In Fig. 2.8 we compare our results for freezing of the first six layers with the estimate that the  $n$ th layer crystallizes when

$$\mu_{\text{int}}^*(z'_n) = \mu^* - g^*z'_n/\sigma \simeq \mu_{\text{coex}}^*, \quad (2.5)$$

where we use that  $z'_n$  is the  $z$ -position of the  $(n-1)$ th local minimum of  $\rho(z)$ , which corresponds to the minimum just below the  $n$ th layer. For the freezing transition of the first and second layer we use, however, that  $z'_n$  is given by the first local minimum, which lies in between the first and second layer:

$$z'_n/\sigma = \begin{cases} 1.0 & n = 1, 2 \\ 0.9 \times (n-1) & n > 2 \end{cases}. \quad (2.6)$$

Note that the predictions are denoted by dashed lines for  $n > 2$ , corresponding to a continuous freezing transition, while for  $n = 1, 2$  the first-order freezing transition is denoted by a solid line. As the simulation results for the freezing transition of the different fluid layers agree well with these predictions, we can conclude that the  $n$ th layer for  $n \geq 2$  is crystalline not because the chemical potential at this height is higher than  $\mu_{\text{coex}}^*$ , but because the chemical potential of the  $(n-1)$ th layer is sufficiently high that this layer is fully crystalline. This layer then acts as a template for the  $n$ th layer, resulting in crystallization of this layer [32].

For  $g^* = 10$ , Eq. (2.5) with  $z'_1/\sigma = 1$  as obtained from Eq. (2.6) for  $n = 1$  predicts that the first layer freezes at a chemical potential  $\mu^* = 26.07$ . Fig. 2.7 shows, however, that the crystallization of the first layer occurs at  $\mu^* \simeq 24$  which corresponds to a height  $z'_1/\sigma = 0.8$ . This is closer to the position of the first layer itself, rather than the minimum between the first and the second layer. Reassuringly, the crystallization of the second layer does occur at  $\mu^* \simeq 26$ . Apparently, our prediction (2.6) only holds for a phase transition from a fluid phase to a stable ordered phase consisting of two crystalline layers, while it fails for  $g^* = 10$ , where we observe a transition from a fluid phase to a phase with only one frozen layer. Hence, one would also expect that if the freezing transition involves a phase with 3 or more crystalline layers (at  $g^* \leq 1$ ) the freezing transition occurs at a different  $\mu^*$  than predicted by (2.6). The value of  $\mu^*$  at the discontinuous freezing transition will probably correspond to a (weighted) average of all the layers that crystallize. However, the error bars in Fig. 2.8 are too large to confirm this conjecture.

In order to compare our results to earlier work we calculate the pressure at the bottom  $P_0^* = \beta P(z=0)\sigma^3$  of the sample and the pressure on the first layer  $P_1^* = \beta P(z=z'_1)\sigma^3$ :

$$P_0^* = \frac{\langle N \rangle \sigma^2 g^*}{A} \quad (2.7)$$

and

$$P_1^* = \frac{(\langle N - N_1 \rangle) \sigma^2 g^*}{A}, \quad (2.8)$$

	Exp. [29]	Sim. [20]	Our work			
$g^*$	1.2	2.625	1.0	2.0	3.0	4.0
$P_0^*$	14.0	14.25	12.6	13.4	14.3	15.3
$P_1^*$	-	-	11.8(3)	11.6(2)	11.6(3)	11.5(1)

**Table 2.1:** The pressure at the bottom  $P_0^* = \beta P(z=0)\sigma^3$  and the pressure on the first layer  $P_1^* = \beta P(z=z_1)\sigma^3$  at the freezing transition of the first layer for gravity  $g^* = 1, 2, 3$ , and 4. For comparison, we also show results from experiments [29] and simulations [20].

where  $N_1$  is the number of particles in the first layer. Tbl. 2.1 displays  $P_0^*$  and  $P_1^*$  at the freezing transition of the first (and second layer) of our simulations. In Ref. [33], it was argued that the first bottom layer will crystallize when  $\beta P(z = \sigma/2)\sigma^3$  reaches the bulk pressure at coexistence  $\beta P_{\text{coex}}\sigma^3 = 11.56$  [9]. However, we observe that  $P_0^*$  depends on  $g^*$  and is always  $> \beta P_{\text{coex}}\sigma^3$ , while  $P_1^*$  is independent of  $g^*$  and equals  $\beta P_{\text{coex}}\sigma^3$  within the error bars. A similar result was obtained using density functional theory and kinetic theory [21, 22], where a linear behavior between  $\langle N \rangle \sigma^2 / A$  and  $g^*$  was found for the freezing transition. For comparison, we also show  $P_0^*$  for previous simulations [20] and experiments [29], which are in reasonable agreement with our simulations.

Finally, we investigate the lattice constant of the bottom layer as a function of  $\mu^*$  and

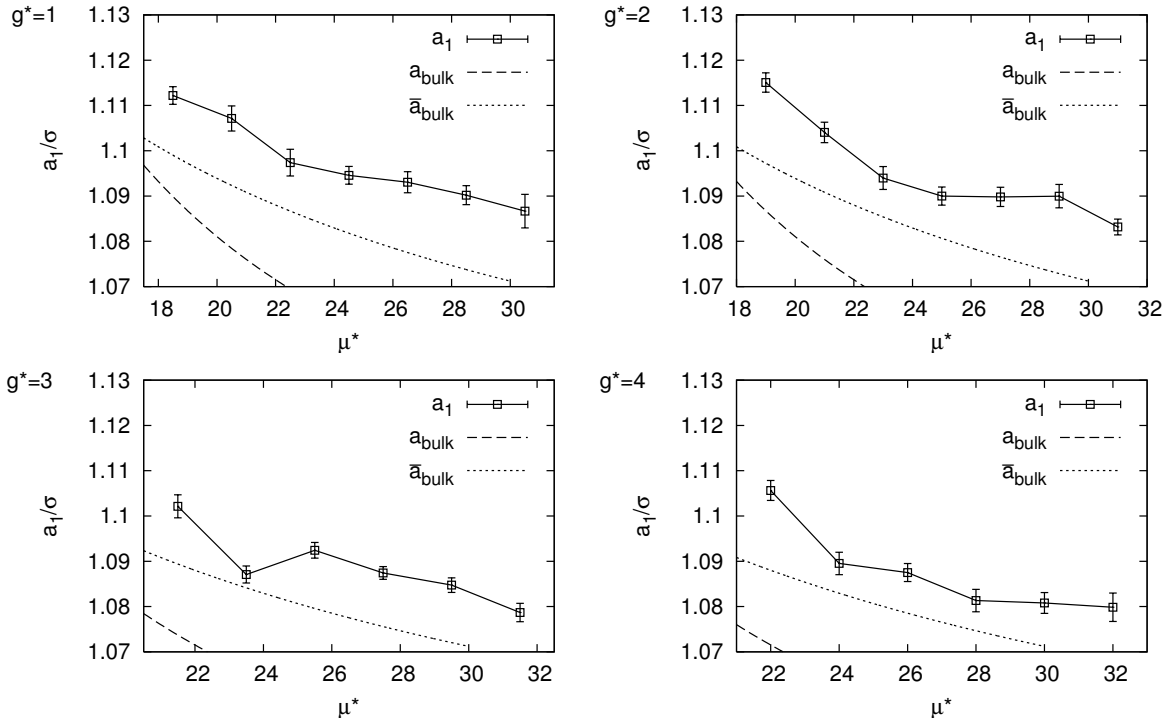


**Figure 2.9:** Lattice constant of the first layer  $a_1$  as function of the chemical potential for varying gravities:  $g^* = 1, 2, 3, 4$  as obtained from simulations ( $\square$ ). The dashed lines denote the lattice constant of a bulk crystal at  $\mu^*$ , while the short-dashed lines show an averaged lattice constant given by Eq. (2.11).

$g^*$ . In our simulations, we determine the lattice constant of the  $n$ th layer by:

$$a_n = \sqrt{\frac{2A}{\sqrt{3}\langle N_n \rangle}}, \quad (2.9)$$

where we assumed a triangular symmetry for the crystal layer and where  $\langle N_n \rangle$  is the number of particles in layer  $n$ . In practice,  $\langle N_n \rangle$  is calculated by

$$\langle N_n \rangle = A \int_{z_n}^{z_{n-1}} \rho(z) dz. \quad (2.10)$$

We plot in Fig. 2.9 the lattice constant of the first layer  $a_1$  as a function of the chemical potential  $\mu^*$  for gravitational field strengths  $g^* = 1, 2, 3$ , and 4. For comparison, we also plot the lattice constant of a bulk crystal at  $\mu^*$  using Speedy's equation of state [34]. We clearly observe in Fig. 2.9 that the simulation results for  $a_1$  are much higher than those of the corresponding bulk crystal. Upon closer inspection, we find that the lattice constants  $a_n$  for  $n > 1$  are all equal to  $a_1$  within the statistical error for all values of  $\mu^*$  and  $g^*$  we considered. This finding is remarkable as the pressure varies enormously with height. As the lattice constants in all the layers are the same, all layers must adjust to each other. Consequently, one might expect that the lattice constant is determined by an average over all layers which have a chemical potential  $\mu_{\text{coex}}^* \leq \mu \leq \mu^*$ :

$$\bar{a}_{\text{bulk}}(\mu^*) = \frac{\int_{\mu_{\text{coex}}^*}^{\mu^*} a_{\text{bulk}}(\mu) d\mu}{\mu^* - \mu_{\text{coex}}^*} \quad (2.11)$$

Fig. 2.9 shows that the agreement between the simulations and this expression has been improved. However, this expression still underestimates the observed lattice constant systematically. This effect is caused by “crystalline” layers with a high  $\psi_6$ , for which  $\mu_{\text{int}}(z) < \mu_{\text{coex}}^*$ . Ignoring these layers with a relatively low  $\mu_{\text{int}}(z)$  and hence a large lattice constant of the corresponding bulk crystal underestimates  $\bar{a}_{\text{bulk}}$  given by (2.11).

## 2.4 Conclusions

We have investigated the nature of the freezing transition in sedimenting colloidal hard spheres. Our results provide evidence for a first-order freezing transition where several fluid layers close to the bottom of the sample freeze at the same chemical potential. If the chemical potential is increased further, additional fluid layers will solidify continuously. We have determined a phase diagram of the freezing transitions of the first six fluid layers as a function of chemical potential and gravity using computer simulations, and we show that our simulation results agree well with a simple prediction given by (2.5) with (2.6). A better understanding of the mechanisms of crystallization is important both for a better insight in colloidal crystallization, as well as for advanced applications. For instance, sedimentation is often used as a method to grow large colloidal crystals for (photonic) applications [35–40]. We also note that the solidification of hard spheres under gravity has implications for granular matter systems [21, 22, 33].



---

## On the stability of orientationally disordered crystal structures of colloidal hard dumbbells

---

We study the stability of orientationally disordered crystal phases in a suspension of colloidal hard dumbbells using Monte Carlo simulations. For dumbbell bond length  $L/\sigma < 0.4$  with  $L$  the separation of the two spheres of the dumbbell and  $\sigma$  the diameter of the spheres, we determine the difference in Helmholtz free energy of a plastic crystal with a hexagonal-close-packed (hcp) and a face-centered-cubic (fcc) structure using thermodynamic integration and the lattice-switch Monte Carlo method. We find that the plastic crystal with the hcp structure is more stable than the one with the fcc structure for a large part of the stable plastic crystal regime. In addition, we study the stability of an orientationally disordered aperiodic crystal structure in which the spheres of the dumbbells are on an random-hexagonal-close-packed (rhcp) lattice, and the dumbbells are formed by taking random pairs of neighboring spheres. Using free energy calculations, we determine the fluid-aperiodic crystal and periodic-aperiodic crystal coexistence regions for  $L/\sigma > 0.88$ .

### 3.1 Introduction

Originally, hard dumbbells were studied as a suitable model for simple nonspherical diatomic or polyatomic molecules, like nitrogen and carbondioxide. In particular, the structure and thermodynamics of the fluid phase of hard dumbbells were investigated, since the structure of molecular liquids is mainly determined by excluded volume effects [41]. Additionally, in order to understand the stable crystal structures in molecular systems, the solid-fluid equilibria of hard dumbbells have been studied intensively by density functional theory [42, 43] and computer simulations [44–46]. However, for simple nonspherical molecules effects other than size and shape can play an important role, such as dispersion forces, Coulombic, and quadrupolar interactions. This might explain the stability of the  $\alpha$ -N<sub>2</sub> crystal phase of nitrogen which is not a stable crystal structure for hard dumbbells [44]. Still, hard dumbbells can be regarded as a reference system for simple molecules, in the same way as hard spheres can serve as a reference system for monatomic fluids.

Recently, new routes to synthesize colloidal dumbbells have become available and the interest in dumbbells has been revived [47–49]. However, the size distributions of these dumbbells are relatively large and often the quantities that can be synthesized are very small. A new method has been proposed to synthesize large quantities of monodisperse colloidal dumbbells for which the aspect ratio can be tuned very easily [50]. In this method, the anisotropic particles are formed by destabilizing a dispersion of colloidal silica spheres resulting in an initial aggregation of the spheres, i.e. dumbbell formation. Subsequently, a layer of silica is grown around these cores to obtain a dumbbell of any length-to-diameter ratio  $L^* = L/\sigma$ , where  $L$  is the distance between the centers of the spheres and  $\sigma$  is the diameter of the dumbbell. By adding salt to the solvent, the dumbbell interactions can be tuned from hard to long-range repulsive interactions. Moreover, the interest in colloidal dumbbells has been triggered by their potential use in photonic applications. In a photonic band gap crystal, light of certain frequencies cannot propagate, irrespective of its direction or polarization. Photonic band gap calculations show, however, that a complete band gap is not possible in a simple system of spherical particles, although for an fcc crystal of air spheres in a background with a high dielectric contrast a full band gap can be obtained [51]. Such an fcc crystal of air spheres can be obtained by infiltration of an fcc crystal of (polymer latex) spheres with a material with a large dielectric constant and subsequent removal of the spheres. Unfortunately, the band gap opens up at high frequencies, where absorption or disorder have a large effect on the transmission [51]. It has been shown that complete band gap at relatively low frequencies can be opened by using anisotropic particles [52, 53]. For instance, it has been shown that dumbbells of tangent spheres on a face-centered-cubic (fcc) or base-centered-cubic lattice exhibit a complete band gap between the second and third band [52]. Unfortunately, these crystal structures are not stable in the bulk for hard dumbbells, but it does show that anisotropic particles are promising for photonic applications. The availability of this new model system of colloidal dumbbells and their potential use for photonic applications warrants a more detailed study of the phase behavior of these particles.

Previous computer simulation studies of hard dumbbells have shown the stability of at least three different solid phases. For small anisotropies and low densities, the dumbbells form a plastic crystal phase in which the particles are on an fcc lattice, but are free to

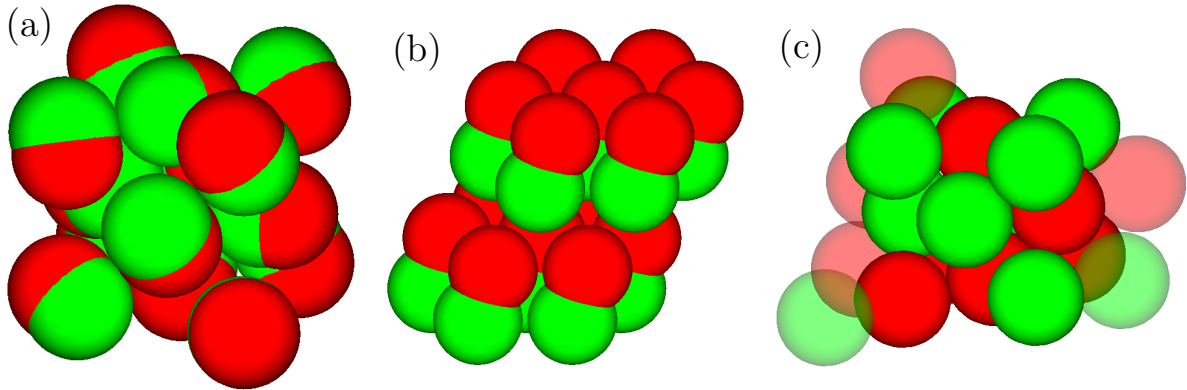


**Figure 3.1:** Snapshots of a few dumbbells in the stable crystal phases. Shown are the plastic crystal phase at  $L = 0.2\sigma$  (a), the CP1 phase at  $L = 0.6\sigma$  (b) and the aperiodic phase at  $L = 0.9\sigma$  (c). One of the spheres of a dumbbell is colored red, the other sphere is green. For clarity of display we show a cubic fcc unit cell of spheres in the aperiodic phase, which is actually part of a larger randomly stacked hexagonal close packed crystal. If the other sphere of the dumbbell was not part of the unit cell, it is shown as a transparent sphere.

rotate, see Fig. 3.1. At sufficiently high density, the orientationally ordered crystal phase (called CP1 in Ref. [44], see Fig. 3.1) becomes stable for all anisotropies. In the ordered solid phase, the dumbbells are arranged into two-dimensional hexagonal close-packed layers in such a way that the spheres of each dumbbell also form a hexagonal close-packed layer. The orientations of the dumbbells are parallel with an angle of  $\arcsin(L^*/\sqrt{3})$  between the dumbbell axis and the normal of the hexagonal layers. The hexagonal layers of dumbbells are stacked in an ABC sequence, so that the spheres form an fcc crystal structure at  $L^* = 1$ . At large anisotropies, the particles can freeze into an aperiodic crystal in which not only their orientations but also the centers-of-masses of the dumbbells are disordered, see Fig. 3.1, although the spheres of each dumbbell are on an rhcp lattice at  $L^* = 1$  and at close packing. When  $L^*$  is smaller than the lattice constant the spheres must be slightly off-lattice and then the crystal is truly aperiodic in all the coordinates. Monte Carlo simulations have shown that the aperiodic crystal is more stable than the ordered solid in a two-dimensional system of hard dimers [54–57]. The stability of an aperiodic crystal structure for a three-dimensional system of hard dumbbells has been proven by free energy calculations and theory in Ref. [58], but only for  $L^* = 1$ .

In the present chapter we first address the question of whether the fcc or hexagonal-close-packed (hcp) structure of the plastic crystal has the lowest free energy for hard dumbbells. The fcc and hcp structures both consist of hexagonally close-packed layers, but they differ in the way the planes are stacked. The stacking sequence for fcc is ABC, while it is ABAB for hcp. The question of which configuration is the most stable structure for hard spheres has been a longstanding issue in the literature. However, it is now well-accepted that the fcc crystal is more stable, although the free energy difference is very small,  $< 10^{-3}k_B T$  per particle, with  $k_B T$  the thermal energy,  $k_B$  Boltzmann’s constant and  $T$  the temperature [6, 59–61]. In this chapter, we show that the hcp structure is more stable for hard dumbbells for a large part of the stable plastic crystal regime. Furthermore, the free energy difference is more than an order of magnitude larger than in the case of

hard spheres.

In the second part of this chapter, we study the stability of an orientationally disordered aperiodic crystal structure for  $L^* > 0.88$ . We confirm that the aperiodic crystal structure is stable for hard dumbbells and we determine the fluid-aperiodic crystal and aperiodic-periodic crystal coexistence regions using free energy calculations. However, to the best of our knowledge, we are not aware of any atomic counterpart of the aperiodic crystal phase of hard dumbbells, or any evidence of a colloidal aperiodic crystal structure. We hope that our findings will stimulate a more detailed experimental investigation of the phase behavior of (colloidal) dumbbells.

## 3.2 Model

We consider a system of hard dumbbells consisting of two fused (i.e. overlapping) hard spheres of diameter  $\sigma$  with the centers separated by a distance  $L$ . We define the reduced bond length or anisotropy of the dumbbell by  $L^* \equiv L/\sigma$ , such that the model reduces to hard spheres for  $L^* = 0$  and to tangent spheres for  $L^* = 1$ . We study the phase behavior of hard dumbbells using computer simulations for  $0 \leq L^* \leq 1$ . We focus our attention on the plastic crystal phase for  $L^* < 0.4$  and the aperiodic crystal phase for  $L^* > 0.9$ . Below we describe the simulation methods that we employ to study the plastic crystal and the aperiodic crystal structures.

## 3.3 Methods and Results

### 3.3.1 Plastic crystal: hcp vs. fcc

We calculate the free energy of both the fcc and the hcp plastic crystal phase by thermodynamic integration using the Einstein crystal as a reference state [9]. The Einstein integration scheme that we employ here involves the usual integration over a path through parameter space which connects the system of interest with the noninteracting Einstein crystal, without crossing a first order phase transition. This means that the Einstein crystal must have the same symmetries as the plastic crystal phase. In particular, the dumbbells must be free to rotate, while the centers-of-masses are fixed to their ideal lattice positions using a harmonic spring with dimensionless spring constant  $\lambda$ . The potential energy function for the harmonic coupling of the particles to their ideal lattice positions reads

$$\beta U(\mathbf{r}^N, \mathbf{u}^N; \lambda) = \lambda \sum_{i=1}^N (\mathbf{r}_i - \mathbf{r}_{0,i})^2 / \sigma^2, \quad (3.1)$$

where  $\mathbf{r}_i$  and  $\mathbf{u}_i$  denote, respectively, the center-of-mass position and orientation of dumbbell  $i$  and  $\mathbf{r}_{0,i}$  the lattice site of particle  $i$ , and  $\beta = 1/k_B T$ . The usual thermodynamic integration path for hard spheres consists of a gradual increase of  $\lambda$  from 0, i.e., the system of interest, to  $\lambda_{\max}$ , where  $\lambda_{\max}$  is sufficiently high that the system reduces to a non-interacting Einstein crystal. However, this method fails in the case of freely rotating hard dumbbells as the system will never reach the limit of a non-interacting Einstein crystal due to the rotational degrees of freedom of the dumbbells: if the lattice constant

is smaller than  $\sigma + L$ , the dumbbells will collide while rotating even if their centers of mass are fixed at their lattice sites. We therefore combine the usual Einstein integration method with the thermodynamic integration technique that was introduced recently for hard spheres by Fortini *et al.* [62], which is based on penetrable potentials that allows us to change gradually from a non-interacting system to a system of freely rotating hard dumbbells. We changed the dumbbell-dumbbell potential energy function to

$$\beta U_{\text{soft}}(\mathbf{r}^N, \mathbf{u}^N; \gamma) = \sum_{i < j} \sum_{\eta, \mu} \beta \varphi(|\mathbf{r}_{i\eta} - \mathbf{r}_{j\mu}|, \gamma) \quad (3.2)$$

with

$$\beta \varphi(r, \gamma) = \begin{cases} \gamma(1 - A(r/\sigma)^2) & r < \sigma \\ 0 & \text{otherwise} \end{cases}, \quad (3.3)$$

where  $\mathbf{r}_{i\eta}$  with  $\eta = \pm 1$  are the positions of the two spheres of dumbbell  $i$ ,  $A$  is an adjustable parameter that is kept fixed during the simulation at a value  $A = 0.9$ , and  $\gamma$  is the integration parameter. The limit  $\gamma \rightarrow \infty$  reduces to the hard-core interaction, but convergence of the thermodynamic integration is already obtained for  $\gamma_{\text{max}} = 200$ . In Ref. [62] it was shown that in order to minimize the error and maximize the efficiency of the free energy calculation, the potential must decrease as a function of  $r$  and must exhibit a discontinuity at  $r$  such that both the amount of overlap and the number of overlaps decrease upon increasing  $\gamma$ . Here, we have chosen this particular form of the potential because it can be evaluated very efficiently in a simulation. We start at a very high value of  $\gamma_{\text{max}} = 200$  where the particles behave as hard dumbbells. Subsequently, we turn on the springs that couple the dumbbells to the lattice by increasing  $\lambda$  from 0 to  $\lambda_{\text{max}}$ . We then decrease  $\gamma$  to 0 such that the system becomes an ideal Einstein crystal. By integrating over both paths and adding the free energy of the noninteracting Einstein crystal, one obtains the Helmholtz free energy  $F$  of a plastic crystal of hard dumbbells,

$$\beta F(N, V, T) = \beta F_{\text{Einst}}(N, V, T) - \int_0^{\lambda_{\text{max}}} d\lambda \left\langle \frac{\partial \beta F}{\partial \lambda} \right\rangle_{\gamma_{\text{max}}} + \int_0^{\gamma_{\text{max}}} d\gamma \left\langle \frac{\partial \beta F}{\partial \gamma} \right\rangle_{\lambda_{\text{max}}}, \quad (3.4)$$

where  $\langle \partial \beta F / \partial \lambda \rangle = \langle \sum_{i=1}^N (\mathbf{r}_i - \mathbf{r}_{0,i})^2 / \sigma^2 \rangle$ , and  $\langle \partial \beta F / \partial \gamma \rangle = \langle \beta U_{\text{soft}}(\mathbf{r}^N, \mathbf{u}^N; \gamma) / \gamma \rangle$ . The Helmholtz free energy of the noninteracting Einstein crystal plus the center of mass correction terms [9] reads:

$$\beta F_{\text{Einst}} = -\frac{3(N-1)}{2} \ln \left[ \frac{\pi}{\lambda_{\text{max}}} \right] + N \ln \left[ \frac{\Lambda_t^3}{\sigma^3} \right] + N \ln \left[ \Lambda_r \right] + \ln \left[ \frac{\sigma^3}{V N^{1/2}} \right]. \quad (3.5)$$

where  $\Lambda_t = (h^2 / 2\pi m k_B T)^{1/2}$  denotes the de Broglie wavelength and  $\Lambda_r = (h^2 / 8\pi^2 I k_B T)^{1/2}$  with  $m$  the mass and  $I$  the moment of inertia. We determine the Helmholtz free energy  $F_{\text{fcc}}$  and  $F_{\text{hcp}}$  of the fcc and hcp plastic crystal, respectively, as a function of the reduced density  $\rho^*$  and anisotropy  $0.1 \leq L^* < 0.4$ . We define the dimensionless density as

$$\rho^* = \frac{d^3 N}{V} \quad \text{and} \quad P^* = \frac{d^3 P}{k_B T} \quad (3.6)$$

where  $d^3 / \sigma^3 = 1 + \frac{3}{2} L^* - \frac{1}{2} (L^*)^3$  is the volume of a dumbbell divided by that of a sphere with diameter  $\sigma$ , so  $d$  is the diameter of a sphere with the same volume as the dumbbell. The

initial configurations for the plastic crystal are generated by placing the dumbbells on an fcc or hcp lattice and by picking random directions for the dumbbells until the dumbbells do not overlap anymore. For state points close to the plastic crystal–cpl coexistence region, we use isobaric-isothermal (NPT) simulations to generate initial configurations. We perform simulations of 864 particles for the fcc and 900 particles for the hcp plastic crystal. We use a 20-point Gauss-Legendre integration for both the  $\gamma$ – and  $\lambda$ –integration.

We find that for  $L^* = 0.05$  and  $L^* = 0.1$  at low densities, the free energy difference is very small  $< 0.001k_B T$  per particle. As the free energies of the fcc and hcp plastic crystal are almost equal, subtracting the free energies will give rise to large errors in the free energy differences. Moreover, we find that the result of the  $\gamma$  integration depends on the precise details of the numerical integration method. This dependence is small compared to the free energy of either phase, but it is a significant error relative to the free energy *difference* between the phases. In order to circumvent this problem, we measure directly the free energy difference in a single simulation using the so-called lattice-switch multicanonical Monte Carlo method [61]. This method has been used successfully to calculate the difference in free energies of the fcc and hcp phase for hard spheres [59–61]. Below, we discuss briefly the method and its extension to dumbbells. For a detailed description of the method, we refer the reader to Ref. [61].

The lattice-switch Monte Carlo method is based on a lattice-switch transformation that maps an fcc configuration onto an hcp configuration, and vice versa. This enables us to sample in a single simulation both crystal structures and to measure the difference in free energies by measuring the probability to find the system in one of the two phases. To this end, we express coordinate  $\mathbf{r}_i$  of particle  $i$  in terms of its displacement  $\Delta\mathbf{r}_i$  from its ideal lattice position  $\mathbf{R}_i^{(\alpha)}$  in phase  $\alpha$ , i.e.,  $\mathbf{r}_i = \mathbf{R}_i^{(\alpha)} + \Delta\mathbf{r}_i$ . A lattice switch from lattice  $\alpha$  to lattice  $\beta$  is then defined by  $\mathbf{r}_i = \mathbf{R}_i^{(\alpha)} + \Delta\mathbf{r}_i \rightarrow \mathbf{R}_i^{(\beta)} + \Delta\mathbf{r}_i$ , for particles  $i = 1, \dots, N$ . In the present work, we fixed the orientations of the dumbbells during the lattice switch. The states for which we can perform the lattice switch without causing any overlaps are rare. We therefore bias the sampling to favor the gateway states that allows us to perform the lattice switch. We define an order parameter that measures how close we are to those gateway states

$$\mathcal{M}(\{\Delta\mathbf{r}\}) = \mathcal{M}(\{\Delta\mathbf{r}\}, \text{hcp}) - \mathcal{M}(\{\Delta\mathbf{r}\}, \text{fcc}), \quad (3.7)$$

where  $\mathcal{M}(\{\Delta\mathbf{r}\}, \alpha)$  denotes the number of overlaps in the configuration where the particle positions are given by the set of displacements  $\{\Delta\mathbf{r}\}$  in phase  $\alpha$ . For an fcc structure,  $\mathcal{M} \geq 0$ , while an hcp structure corresponds to  $\mathcal{M} \leq 0$ . If  $\mathcal{M} = 0$ , there will be no overlaps in both the fcc and hcp structure, and a lattice switch will be successful. By assigning multicanonical weights  $\exp[\eta(\mathcal{M})]$  to each macrostate  $\mathcal{M}$  we can bias the system towards the switching states, where  $\mathcal{M} = 0$ .

We first measure the probability distribution  $\mathcal{P}(\mathcal{M})$  of being in state  $\mathcal{M}$  for an unbiased system, i.e., multicanonical weights  $\eta(\mathcal{N}) = 0$ . Subsequently, we use the  $\mathcal{P}(\mathcal{M})$ , to define the multicanonical weights in the biased sampling for the next simulation using

$$\eta(\mathcal{M}) = -\ln(\mathcal{P}(\mathcal{M})) + C_0, \quad (3.8)$$

where  $C_0$  is an arbitrary constant. In this simulation we measure the biased probability distribution, correct for the bias to obtain the new estimate for  $\mathcal{P}(\mathcal{M})$  and use the above

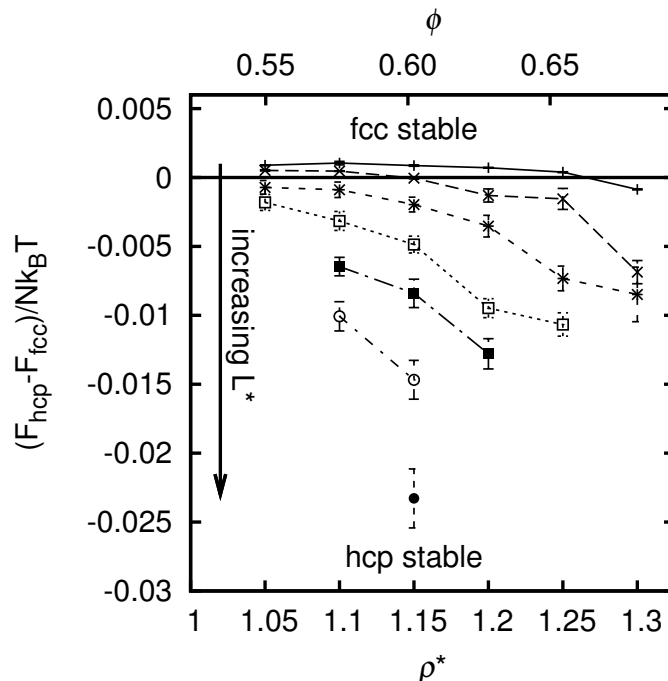


**Figure 3.2:** The difference in the Helmholtz free energies of the hcp plastic crystal  $F_{\text{hcp}}$  and the fcc plastic crystal  $F_{\text{fcc}}$  as a function of  $\rho^*$  and  $\phi = (\pi d^3/6)N/V$  for different  $L^* = 0.05, 0.1, \dots, 0.35$  from top to bottom. The free energy difference at  $L^* = 0.05$  and the one at  $L^* = 0.1$  with  $\rho^* < 1.2$  are results from the lattice-switch Monte Carlo calculations (error bars are smaller than the symbols), while all other points are obtained using the Einstein integration method.

expression to get the new weights. We repeat this process, until the measured probability distribution in the biased simulation is essentially flat. We then use these weights in a long simulation to calculate the final  $\mathcal{P}(\mathcal{M})$ .

The probability  $\mathcal{P}(\mathcal{M})$  can either be measured directly in a simulation by the number of times a macrostate is visited, i.e. the visited-state (VS) method, or one can measure in a simulation the bias corrected transition probability matrix  $\rho(\mathcal{M} \rightarrow \mathcal{N})$  of going from state  $\mathcal{M}$  to  $\mathcal{N}$  and use the “detailed balance” condition

$$\mathcal{P}(\mathcal{M}) \rho(\mathcal{M} \rightarrow \mathcal{N}) = \mathcal{P}(\mathcal{N}) \rho(\mathcal{N} \rightarrow \mathcal{M}), \quad (3.9)$$

in order to obtain  $\mathcal{P}(\mathcal{M})$ , i.e. the transition probability (TP) method.

We use the lattice-switch Monte Carlo method to measure directly the Helmholtz free energy in a simulation of 1728 particles. We expect the finite size effects to be small for this system size. We use the transition probability method to determine the set of multicanonical weights. In Fig. 3.2, we show the Helmholtz free energy difference  $F_{\text{hcp}} - F_{\text{fcc}}$  using the Einstein crystal thermodynamic integration method and the lattice-switch Monte Carlo method as a function of  $\rho^*$  (and packing fraction  $\phi \equiv (\pi d^3/6)N/V$ ) for varying  $L^*$ .

Fig. 3.2 clearly shows that the stability of hcp with respect to fcc increases upon increasing  $L^*$ . It is striking that even for  $L^* = 0.05$ , hcp is more stable for sufficiently

high densities, since it is well-known that the fcc phase is the most stable one for hard spheres. For  $L^* > 0.1$ , the hcp plastic phase is stable for all densities that we considered. Furthermore, the absolute value of the Helmholtz free energy difference increases by more than an order of magnitude upon increasing  $L^*$ . The maximum value of the Helmholtz free energy difference per particle, that we find, is  $0.023(2)k_B T$  for  $L^* = 0.35$ , which is more than a factor of 20 larger than the free energy difference for hard spheres at close packing.

### 3.3.2 aperiodic vs. periodic crystal

We now turn our attention to the stability of the aperiodic crystal phase with respect to the periodic crystal structure. At large anisotropies and sufficiently high densities, we expect the aperiodic crystal phase to be stable, because for those parameters the aperiodic phase has a close packed density which is almost as high as the close packed density of the CP1 phase, while the degeneracy increases the entropy of the aperiodic phase compared to the entropy of the CP1 phase.

#### Aperiodic crystal phase

In an aperiodic crystal at close packing and  $L^* = 1$ , the individual spheres of the dumbbells are arranged on a close-packed fcc lattice, while the dumbbells, which can be considered as bonds between two sites, are chosen randomly. In the remainder of the chapter, such an arrangement is referred to as a bond configuration. If there are  $\Omega_{\text{aper}}$  possible bond configurations that all have the same free energy  $F_{\text{conf}}$ , the total free energy of the aperiodic crystal reads

$$\beta F = -\ln \Omega_{\text{aper}} + \beta F_{\text{conf}}. \quad (3.10)$$

Ignoring the slight variation of  $F_{\text{conf}}$  for now, we average  $F_{\text{conf}}$  over several typical aperiodic bond configurations and use this value. Furthermore, we approximate  $\Omega_{\text{aper}}$  by the multiplicity at close packing and  $L^* = 1$ . We note, however, that  $\Omega_{\text{aper}}$  may depend on density and  $L^*$ , which we ignore here for simplicity.

In order to determine the multiplicity of the aperiodic crystal  $\Omega_{\text{aper}}$  at close packing and  $L^* = 1$ , we introduce a method that allows us to switch from the aperiodic crystal phase to a reference phase of which the degeneracy is known, and vice versa. By measuring the probability that the system is in either of the two phases, we can determine the multiplicity of the aperiodic phase:

$$\Omega_{\text{aper}} = \mathcal{P}_{\text{aper}} / \mathcal{P}_{\text{ref}} \times \Omega_{\text{ref}}, \quad (3.11)$$

where the subscript “ref” denotes the periodic reference phase.

For the reference phase, we use the so-called CP3 phase, which is the phase where all the dumbbells are arranged into two-dimensional hexagonal layers with all the particles, as in the CP1 phase, aligned in the same direction within the hexagonal layer, while the tilt angle alternates between successive layers. However, in order to form a close packed crystal, the particles in different hexagonal layers can point in three different directions, yielding a certain degeneracy for the CP3 phase as well. The degeneracy of CP3 can

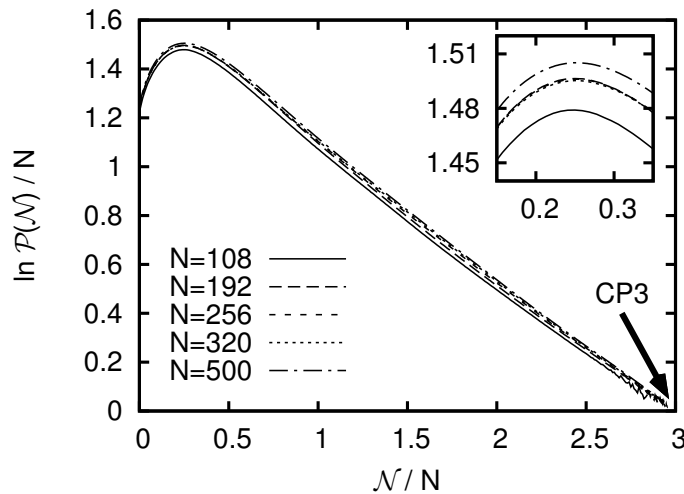


**Figure 3.3:** The probability distribution  $\ln \mathcal{P}(\mathcal{N})$  of the parallel bond order parameter  $\mathcal{N}$  for systems with varying particle numbers  $N$ . The inset shows an enlarged view of the region where  $\mathcal{P}(\mathcal{N})$  is maximal.

be calculated by considering all  $3^{N_z}$  possibilities for the directions of the  $N_z$  hexagonal layers, and by correcting for the number of possibilities that are identical if one takes into account the periodic boundary conditions in the  $z$ -direction.

In order to measure the probability ratio as defined in Eq. (3.11), we first define an order parameter that enables us to distinguish the CP3 phase from the aperiodic phase. We define the parallel bond order parameter  $\mathcal{N} \equiv \frac{1}{4} \sum_{i=1}^{2N} \sum_{j=1}^6 f_{ij}$ , where the first sum runs over all sites  $i$  of the lattice and the second sum runs over the 6 nearest neighbors  $j$  of site  $i$  within the same layer. If the dumbbell, which has a sphere on site  $i$ , is parallel to the dumbbell that has a sphere on site  $j$ ,  $f_{ij} = 1$ , otherwise  $f_{ij} = 0$ . Since every bond is counted twice and the number of parallel bonds can change by a minimum of two, the factor 4 ensures that  $\mathcal{N}$  changes by at least 1 if we change the bond configuration. For the CP3 phase,  $\mathcal{N} = 2N \times 6/4 = 3N$ , since all six neighbors of all  $2N$  sites are parallel in this phase.

We now introduce a MC move which allows us to generate a new configuration of bonds with a different value of  $\mathcal{N}$ . This bond switch move involves disconnecting and reconnecting bonds until a new configuration is found. We refer the reader for more technical details to App. 3.A. We now employ the bond switch move for a random hcp crystal phase with  $L^* = 1$ . We use multicanonical Monte Carlo to measure the probability ( $\mathcal{P}(\mathcal{N})$ ) of being in state  $\mathcal{N}$  using weights  $\eta(\mathcal{N})$ , which are refined using the VS method. The probability ratio reads simply,

$$\frac{\mathcal{P}_{\text{aper}}}{\mathcal{P}_{\text{CP3}}} = \frac{\sum_{\mathcal{N} < 3N} \mathcal{P}(\mathcal{N})}{\mathcal{P}(\mathcal{N} = 3N)}. \quad (3.12)$$

In Fig. 3.3, we plot the probability distribution  $\mathcal{P}(\mathcal{N})$  of the parallel bond order parameter  $\mathcal{N}$  for systems with varying particle numbers  $N$ . We note that the probability distribution  $\mathcal{P}(\mathcal{N})$  has a maximum of about  $\exp[1.5N]$  at  $\mathcal{N}/N \simeq 0.25$ . In Fig. 3.4, we plot the degeneracy of the aperiodic crystal phase as a function of the number of particles  $N$ . For

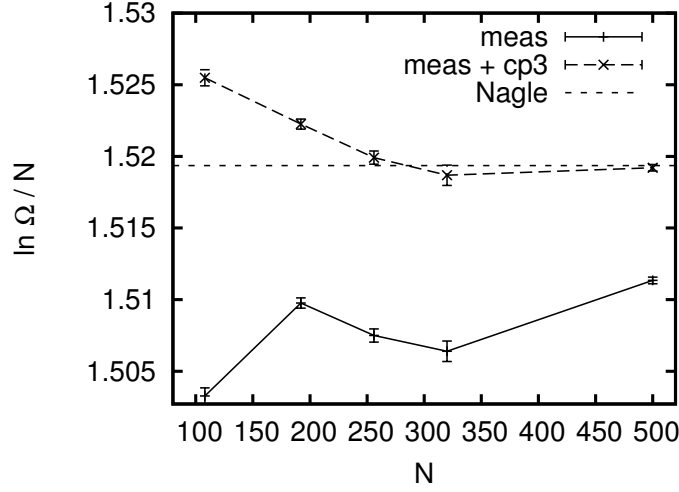


**Figure 3.4:** The logarithm of the degeneracy of the aperiodic crystal as a function of the number of particles  $N$ . “meas” denotes the measured free energy difference between CP3 and the aperiodic phase, in “meas + CP3” the degeneracy of CP3 is included and “Nagle” denotes the theoretical result  $\ln(4.5693) \simeq 1.519$  [63].

comparison, we also plot the theoretical result of Ref. [63], and we find good agreement for  $N \geq 256$ .

We determine  $F_{\text{conf}}$  at  $L^* = 1$  using the Einstein integration method as described above for the plastic crystal phase. However, we include an additional coupling of the orientation of dumbbell  $i$ , i.e.,  $\mathbf{u}_i$ , to an aligning field. The potential energy function that we use to achieve both couplings reads:

$$\beta U(\mathbf{r}^N, \mathbf{u}^N; \lambda) = \lambda \sum_{i=1}^N (\mathbf{r}_i - \mathbf{r}_{0,i})^2 / \sigma^2 + \sum_{i=1}^N \lambda (1 - |\cos(\theta_{i0})|) + \beta U_{\text{soft}}(\mathbf{r}^N, \mathbf{u}^N; \gamma), \quad (3.13)$$

where  $\theta_{i0}$  is the angle between  $\mathbf{u}_i$  and the ideal tilt vector of particle  $i$ . The ideal tilt vectors of all particles are measured in an NPT simulation. The free energy of the hard dumbbell system  $\beta F(N, V, T)$  can now be related to the known free energy of an Einstein crystal by thermodynamic integration

$$\begin{aligned} \beta F(N, V, T) = & \beta F_{\text{Einst}}(N, V, T) - \int_0^{\lambda_{\text{max}}} d\lambda \left\langle \sum_{i=1}^N (\mathbf{r}_i - \mathbf{r}_{0,i})^2 / \sigma^2 \right\rangle_{\gamma_{\text{max}}} \\ & - \int_0^{\lambda_{\text{max}}} d\lambda \left\langle \sum_{i=1}^N \lambda (1 - |\cos(\theta_{i0})|) \right\rangle_{\gamma_{\text{max}}} + \int_0^{\gamma_{\text{max}}} d\gamma \left\langle \beta U_{\text{soft}}(\mathbf{r}^N, \mathbf{u}^N; \gamma) / \gamma \right\rangle_{\lambda_{\text{max}}}. \end{aligned} \quad (3.14)$$

The Helmholtz free energy of the noninteracting Einstein crystal plus the center of mass

phase	$L^*$	$\rho^*$	$f_{\text{exc}}$
aper	1	1.15	13.887(7)
CP1	1	1.181	14.176(2)
CP1 <sup>†</sup>	1	1.15	13.45
CP1	0.95	1.216	14.555(3)
CP1 <sup>†</sup>	0.95	1.181	11.28
CP1	0.88	1.2283	14.172(3)
CP1 <sup>†</sup>	0.88	1.181	10.71

**Table 3.1:** Excess free energies,  $f_{\text{exc}} \equiv (F - F_{\text{id}})/(Nk_B T)$ , of the aperiodic and periodic phase, where  $F_{\text{id}}$  is the ideal gas free energy. <sup>†</sup>calculated using thermodynamic integration (3.17).

correction terms [9] reads:

$$\begin{aligned} \beta F_{\text{Einst}} = & -\frac{3(N-1)}{2} \ln \left[ \frac{\pi}{\lambda_{\text{max}}} \right] + N \ln \left[ \frac{\Lambda_t^3}{\sigma^3} \right] \\ & + N \ln[\Lambda_r] + \ln \left[ \frac{\sigma^3}{V N^{1/2}} \right] - N \ln(J(\lambda_{\text{max}})), \end{aligned} \quad (3.15)$$

where

$$J(\lambda) = \int_0^1 e^{\lambda(x-1)} dx = \frac{1 - e^{-\lambda}}{\lambda}. \quad (3.16)$$

We perform the Einstein crystal thermodynamic integration method for an aperiodic crystal with  $L^* = 1$  averaging over ten different bond configurations, see Tbl. 3.1. The initial configurations of aperiodic crystal structures for these and all other simulations of aperiodic crystals were obtained in two steps. First, we generated ten configurations of dumbbells with  $L^* = 1$  at close packing, using moves similar to bond switch moves. Secondly, starting at  $L^* = 1$ , then decreasing  $L^*$  in steps of 0.01, we measured the average configuration in an  $NPT$  simulation with reduced pressure,  $P^* = d^3 P/k_B T = 100$ , which was stored to be used as initial configuration for the simulation at the next  $L^*$  and for all further simulations of the aperiodic phase.

The Helmholtz free energy of the hard dumbbell systems for lower  $L^*$  and arbitrary density  $\rho^*$  is obtained by the following thermodynamic integrations,

$$\beta F(\rho_1^*, L^*) = \beta F(\rho_0^*, L^*) + \int_{\rho_0^*}^{\rho_1^*} d\rho \left\langle \frac{N\beta P(\rho, L)}{\rho^2} \right\rangle \text{ and} \quad (3.17)$$

$$\beta F(\rho^*, L_1^*) = \beta F(\rho^*, L_0^*) + \int_{L_0^*}^{L_1^*} dL \left\langle \frac{\partial \beta F(\rho^*, L)}{\partial L} \right\rangle. \quad (3.18)$$

The integrand in Eq. (3.17) is calculated using standard  $NPT$  simulations, in which we measure the density and average over 5 different bond configurations. Alternatively, we use bond switch moves in  $NPT$  simulations of  $N - 1$  dumbbells and 2 hard spheres to calculate the density, see App. 3.B. In Figs. 3.5 and 3.6, we show the equation of state for 5 different aperiodic crystal structures at  $L^* = 1$  and  $L^* = 0.92$ , respectively. These

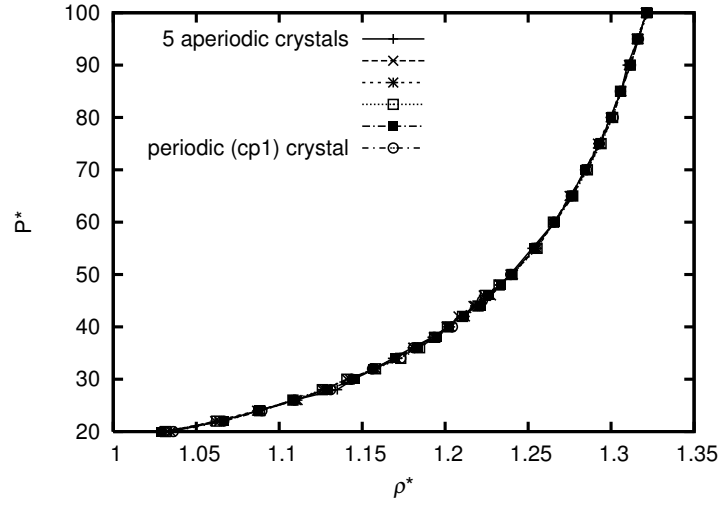


**Figure 3.5:** The dimensionless pressure  $d^3P/k_BT$  as a function of dimensionless density  $d^3N/V$  for five different bond configurations of the aperiodic phase (aper) and for the periodic CP1 phase at  $L^* = 1$ . The 6 curves are indistinguishable.

were obtained in simulations without bond switch moves. We observe that the equations of state of all five aperiodic crystal structures are almost indistinguishable.

The derivative of the free energy with respect to the elongation  $L^*$  in Eq. (3.18) is

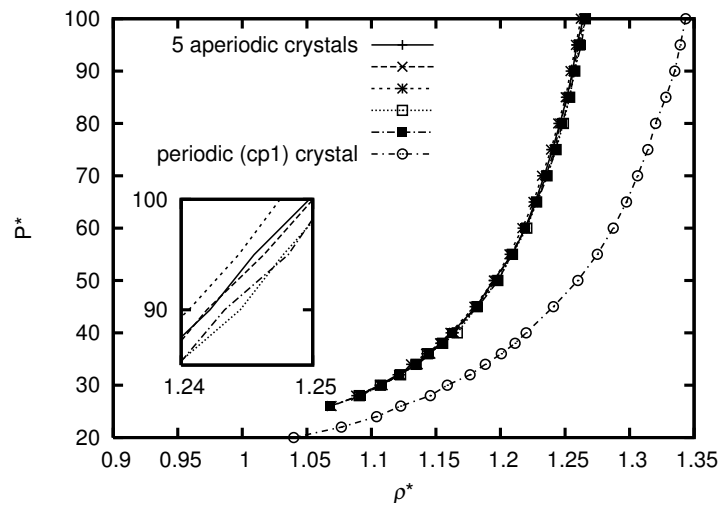


**Figure 3.6:** The dimensionless pressure  $d^3P/k_BT$  as a function of dimensionless density  $d^3N/V$  for five different bond configurations of the aperiodic phase (aper) and for the periodic CP1 phase at  $L^* = 0.92$ . The inset shows an enlargement to be able to distinguish the pressures of the different configurations of the aperiodic phase

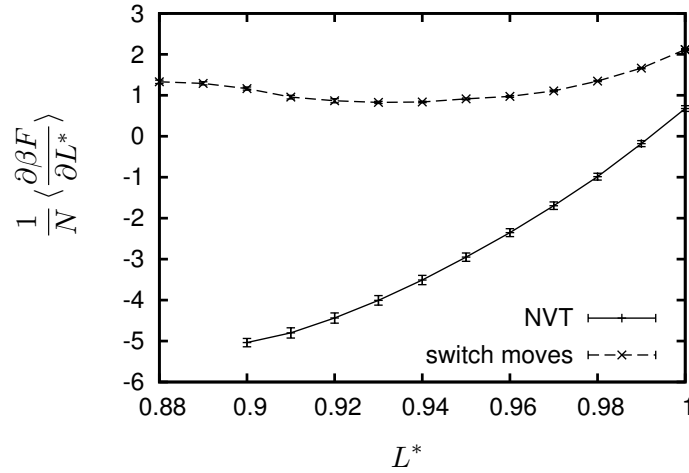


**Figure 3.7:** The derivative of the free energy  $\langle \frac{\partial \beta F}{\partial L^*} \rangle$  (per dumbbell in units of  $k_B T$ ) with respect to  $L^*$  at  $\rho^* = 1.15$  for the aperiodic phase. “NVT” are the results obtained from standard *NVT* simulations and averaged over 10 different bond configurations. “bond switch moves” denotes the results obtained from single simulations with bond switch moves.

determined using [64]

$$\left\langle \frac{\partial \beta F(\rho^*, L)}{\partial L} \right\rangle = -\frac{1}{2} \lim_{r \downarrow \sigma} \left\langle \sum_{i < j} \sum_{\eta, \mu} \delta(|\mathbf{r}_{i\eta} - \mathbf{r}_{j\mu}| - r) \frac{\mathbf{r}_{i\eta} - \mathbf{r}_{j\mu}}{|\mathbf{r}_{i\eta} - \mathbf{r}_{j\mu}|} \cdot (\eta \mathbf{u}_i - \mu \mathbf{u}_j) \right\rangle - \frac{3N(1 - (L^*)^2)}{2 + 3L^* - (L^*)^2} \frac{\beta P}{\rho}, \quad (3.19)$$

where the latter term arises as the free energy derivative is determined at fixed  $\rho^*$ , rather than at fixed  $\rho \equiv \sigma^3 N/V$ . Using a similar expression, the pressure in this term is calculated:

$$\frac{\beta P}{\rho} = 1 + \frac{1}{3N} \lim_{r \downarrow \sigma} \left\langle \sum_{i < j} \sum_{\eta, \mu} \delta(|\mathbf{r}_{i\eta} - \mathbf{r}_{j\mu}| - r) \frac{\mathbf{r}_{i\eta} - \mathbf{r}_{j\mu}}{|\mathbf{r}_{i\eta} - \mathbf{r}_{j\mu}|} \cdot (\mathbf{r}_i - \mathbf{r}_j) \right\rangle. \quad (3.20)$$

This expression is the equivalent of the virial expression for the pressure of hard spheres,  $\beta P/\rho = 1 + 4\phi \lim_{r \downarrow \sigma} g(r)$ , where  $\phi = (\pi\sigma^3/6) N/V$  is the packing fraction. We checked that the integration of  $\langle \partial \beta F / \partial L \rangle$  yields the same results within the statistical error as those obtained from the Einstein integration method. Both the virial expression for the pressure and the expression for  $\langle \partial \beta F / \partial L \rangle$  require an extrapolation of  $r$  to  $\sigma$ . This can only be done reliably if the function to extrapolate is nearly linear, which corresponds to restricting the function to a very small interval range near  $\sigma$ . To get sufficient accuracy on this small interval we need to run long simulations. For this reason we do not use the virial expression for the pressure to obtain the equation of state, instead, we use *NPT* simulations. We perform standard *NVT* simulations to measure  $\langle \partial \beta F / \partial L \rangle$  and we average over the ten initial configurations mentioned above. Alternatively, we use bond switch moves in *NVT* simulations of  $N - 1$  dumbbells and 2 hard spheres to calculate

$\langle \partial \beta F / \partial L \rangle$ , see App. 3.B. Fig. 3.7 shows that  $\langle \partial \beta F / \partial L \rangle$  is negative and that its absolute value decreases with  $L^*$  if no bond switch moves are used. However, if bond switch moves are employed,  $\langle \partial \beta F / \partial L \rangle$  is actually positive and its dependence on  $L$  is much reduced and nonmonotonic. Although  $\langle \partial F / \partial L^* \rangle / N$  is rather large (in absolute value) compared to  $k_B T$ , the free energy difference as calculated by the integral in Eq. (3.18) is never very large for the aperiodic phase. This is because the integration interval is no larger than the small region ( $0.9 \lesssim L \leq 1$ ) where the aperiodic phase is stable.

### Periodic crystal structure (CP1)

In order to obtain the lattice direction and lattice constant for the CP1 phase, we perform NPT simulation with a variable box shape [65], as the lattice direction changes as a function of density and  $L^*$  [44]. We employ these configurations in the Einstein crystal thermodynamic integration method as described in Eqs. (3.13)-(3.15) to obtain the Helmholtz free energy for varying  $L^*$ , see Tbl. 3.1. We perform NPT simulations to obtain the equation of state for varying  $L^*$ . We plot the equation of state for the CP1 phase in Fig. 3.5 and we find that the equation of state is indistinguishable from the equations of state of the different bond configurations of the aperiodic crystal structure for  $L^* = 1$ . For comparison, we plot the equation of state of the CP1 phase for  $L^* = 0.92$  in Fig. 3.6. We clearly see that the pressure  $P^*$  is higher for the aperiodic crystal structure than for the CP1 phase, as the dumbbells fit less efficiently in the aperiodic crystal structure upon decreasing  $L^*$ . We obtain the Helmholtz free energy as a function of  $\rho^*$  by integrating the equation of state of CP1 for varying  $L^*$ , see Eq. (3.17).

### Fluid phase

We employ the equation of state of Tildesley and Street for the fluid phase of hard dumbbells, which is known to be very accurate [41].

### Phase diagram

We determine the fluid-plastic crystal, fluid-aperiodic crystal and the aperiodic-CP1 crystal coexistence by employing the common tangent construction to the free energy curves. The resulting phase diagram, together with the data from Refs. [44, 45] for  $L^* < 0.9$ , is shown in Fig. 3.8. We checked that the phase boundaries for the fluid-hcp plastic crystal and the hcp plastic crystal-cp1 coexistences hardly change compared to the results from [44, 45] for the fcc plastic crystal phase. We find for  $L^* > 0.92$ , a fluid-aperiodic crystal phase coexistence at low densities and an aperiodic-CP1 crystal phase coexistence region at higher densities. The stable region of the aperiodic crystal phase increases upon increasing  $L^* \rightarrow 1$ . If we measure  $\langle \partial F / \partial L \rangle$  and  $P$  in simulations that include bond switch moves, the coexistence lines shift slightly, such that the aperiodic phase is stable in a larger region of the phase diagram, at the cost of the stability of the CP1 phase and, to lesser extent, the fluid phase, see Fig. 3.9. In Tbl. 3.2 the resulting coexistence data of both methods are tabulated.

If we compare our densities of the fluid-aperiodic crystal coexistence,  $\rho_{\text{fluid}}^* = 0.976$  and  $\rho_{\text{aper}}^* = 1.085$  with Ref. [58], we find a small deviation from their simulation results,

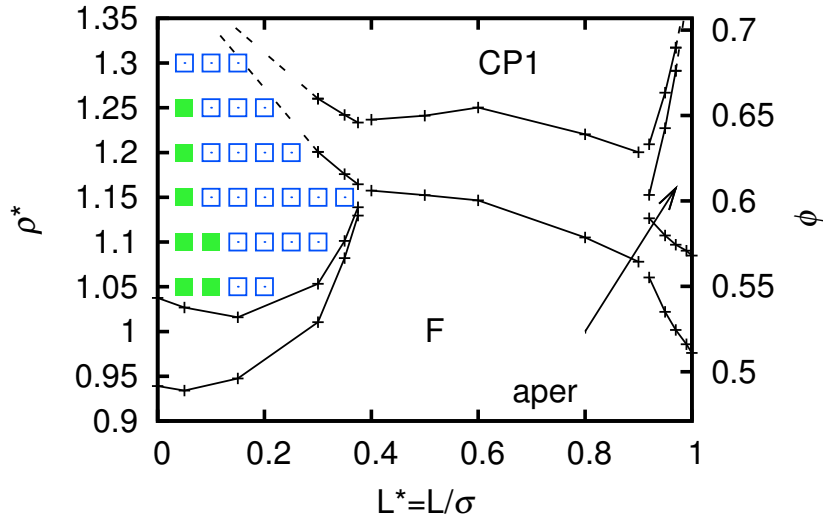


**Figure 3.8:** The phase diagram of hard dumbbells in the  $\rho^*$  (and packing fraction  $\phi$ ) versus  $L^* = L/\sigma$  representation. F denotes the fluid phase and CP1 the periodic crystal. The aperiodic phase (aper) is stable only in a narrow region of the phase diagram. The stable fcc type plastic crystal is denoted by filled squares, the hcp plastic crystal phase is denoted by empty squares. The coexistence densities for  $L < 0.9$  are taken from Refs. [44, 45].

$\rho_{\text{fluid}}^* = 0.990$  and  $\rho_{\text{aper}}^* = 1.105$ , while the theoretical results obtained from an extension of the Wertheim theory [66],  $\rho_{\text{fluid}}^* = 0.983$  and  $\rho_{\text{aper}}^* = 1.094$ , agree slightly better with our coexistence densities. We wish to note here that it is surprising that such a simple theory predicts the fluid–solid equilibrium very accurately, as many theories fail to predict the freezing transition of molecular fluids.

### 3.4 Summary and discussion

In this chapter we have studied the phase behavior of hard dumbbells. First, we have investigated whether the fcc or the hcp structure of a plastic crystal of hard dumbbells has the lowest free energy. We calculated the Helmholtz free energies of the hcp and fcc plastic crystal using the Einstein integration method and the lattice-switch multicanonical Monte Carlo method. We have shown that the hcp structure is more stable for hard dumbbells for a large part of the stable plastic crystal regime. This should be contrasted with hard spheres ( $L^* = 0$ ) for which fcc is more stable than hcp for all densities. The free energy difference between hcp and fcc increases with  $L$ . The maximum free energy difference is about  $0.02Nk_B T$ , a factor of 20 higher than that of hard spheres. The fact that this difference grows with  $L$  might be explained by the difference in available volume for a dumbbell in a fcc or hcp crystal structure. If one considers a perfect frozen fcc or hcp crystal structure with a subset of particles that are moveable, one can expand the entropy of the fcc or hcp crystal structure into the volume available for a single moveable dumbbell, two, three, four, etc. moveable dumbbells in the cage formed by all the frozen particles [67, 68]. For hard spheres the available volume for a single sphere is identical for

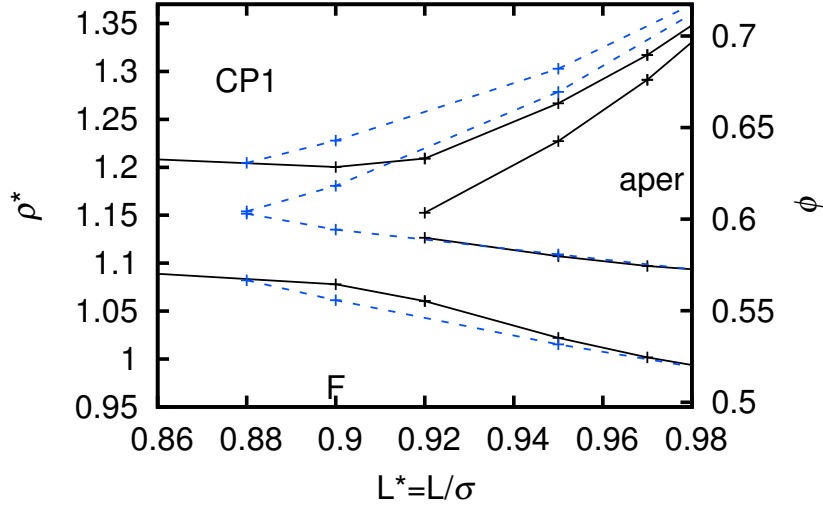


**Figure 3.9:** The large- $L$  part of the phase diagram of dumbbells with (dashed line) and without bond switch moves (solid line) in  $\rho^*$  (and packing fraction  $\phi$ ) versus  $L^* = L/\sigma$  representation. The lines are a guide to the eye. The stability of the aperiodic phase (aper) increases if bond switch moves are included. CP1 denotes the periodic crystal and F the fluid phase.

using standard MC simulations

$L^*$	phase 1	phase 2	$\rho_1 d^3$	$\rho_2 d^3$	$\beta P d^3$	$\mu^*$
0.92	fluid	aper	1.060	1.127	32.89	40.21
0.92	aper	CP1	1.153	1.209	37.66	44.40
0.95	fluid	aper	1.022	1.107	28.04	35.84
0.95	aper	CP1	1.227	1.267	54.72	58.48
0.97	fluid	aper	1.002	1.097	25.90	33.91
0.97	aper	CP1	1.291	1.317	86.88	83.60
1.00	fluid	aper	0.976	1.085	23.60	31.85

using bond switch moves

$L^*$	phase 1	phase 2	$\rho_1 d^3$	$\rho_2 d^3$	$\beta P d^3$	$\mu^*$
0.88	fluid	aper	1.082	1.152	35.15	41.94
0.88	aper	CP1	1.154	1.205	35.62	42.34
0.90	fluid	aper	1.061	1.135	32.34	39.50
0.90	aper	CP1	1.181	1.228	40.37	46.43
0.95	fluid	aper	1.015	1.109	27.12	34.94
0.95	aper	CP1	1.279	1.303	72.30	72.14
1.00	fluid	aper	0.977	1.083	23.67	31.92

**Table 3.2:** Reduced densities, pressures and chemical potentials  $\mu^* = \beta\mu - \ln(\Lambda_t^3 \Lambda_r / \sigma^3)$  of the fluid–aperiodic crystal and the aperiodic crystal–CP1 coexistences at various  $L^*$ , see also Fig. 3.9

hcp and fcc, but the available volume for a pair of spheres is larger at close packing for the hcp phase, which would suggest that hcp is more stable for hard spheres. However, the available volume for five moveable spheres is higher for fcc than for hcp, and hence the fcc phase is more stable. As it is not possible to calculate higher-body corrections, one cannot draw any definite conclusions for hard spheres on the basis of this expansion. For dumbbells with a finite anisotropy the free volume of a single dumbbell in the cage formed by its neighbors is different for fcc than for hcp. The difference in the available volume of a single moveable dumbbell increases with  $L^*$ , which might explain the increase in free energy difference as  $L$  increases. However, as we did not include any higher-body corrections, we have to take this with a grain of salt. Furthermore, we conclude that including the hcp phase does not change the fluid-plastic crystal phase boundary.

In the second part of this chapter, we studied the stability of an orientationally disordered aperiodic crystal structure for  $L^* > 0.88$ . We first determined the degeneracy of the aperiodic crystal phase using a bond switch move. Subsequently, we calculated the free energy by varying methods, such as the Einstein integration method, equation of state integration, and integration of the derivative of the Helmholtz free energy with respect to the elongation of the dumbbells. Using the free energy calculations, we have shown that the aperiodic crystal structure is stable for hard dumbbells for  $L^* \geq 0.92$  or, if bond switch moves were used,  $L^* \geq 0.88$  and we have determined the fluid-aperiodic crystal and aperiodic-periodic crystal coexistence. In conclusion, we have shown the stability of two new crystal structures, i.e., the hcp plastic crystal phase and the aperiodic crystal structure, in a system of hard dumbbells. We hope that our results stimulate new experiments on colloidal dumbbells with a focus on these new structures.

## Appendix 3.A Bond switch moves at close packing

A (biased) bond switch move at close packing is very similar to the configurational bias Monte Carlo (CBMC) method [9].

It consist of the following steps:

- **step 1:** Choose a site of the lattice at random. This site is called the loose end and its position is labeled  $\mathbf{r}(1)$ . Break the bond which connects the loose end to another site at  $\mathbf{r}(0)$ .
- **step 2 to n-1:** Pick a nearest neighbor of the loose end with probability  $\mathcal{P}_i$ . We use  $\mathcal{P}_i = \exp[-\beta u_i]/w_i$ , where  $u_i = \lambda_b |\mathbf{r}_i - \mathbf{r}(0)|^2$ , and  $w_i = \sum_k \exp(-\beta u_k)$ , the sum is over all the neighbors of the loose end and  $\mathbf{r}_i$  is the position of neighbor  $i$ . We disconnect the bond which paired this neighbor  $i$  with another site at  $\mathbf{r}(1)$ , which becomes the new loose end. In this way, the loose end will make a trajectory throughout the system.
- **step n:** After a certain number of steps, one of the neighbors of the loose end is site  $\mathbf{r}(0)$ . If this site is selected we connect the loose end to  $\mathbf{r}(0)$ . There are no loose ends anymore in the system and the bond switch move is complete. The length of the trajectory is determined by  $\lambda_b$ . An example of the entire bond switch move on

a hexagonal lattice is depicted in Fig. 3.10. We note that in our simulations bond switch moves are performed in 3 dimensions.

The bond switch move satisfies detailed balance as the probability to generate the new bond configuration starting with the old bond configuration equals the probability of generating the old configuration from the new configuration, since both probabilities are equal to products of the same factors  $P_i$ , the only difference being the order in which the factors occur.

## Appendix 3.B Off-lattice bond switch moves

For densities lower than close packing or if  $L^* < 1$  not all bond configurations are equally probable. However, if we are able to construct a bond switch move that visits configurations with a Boltzmann probability, i.e. that obeys detailed balance, we can take this into account. Two problems arise, when one applies the bond switch move as it was defined in the last section, to lower  $\rho^*$  and  $L^*$ . First of all, the connection and reconnection step needs to be adjusted, as spheres must be moved to detach from one dumbbell, and attach to another. Suppose that  $i$  is a single sphere at  $\mathbf{r}_i$  and  $j$  is a dumbbell with direction vector  $\mathbf{u}_j$  and center of mass position  $\mathbf{r}_j$  and that we wish to connect sphere  $\eta = \pm 1$  of dumbbell  $j$  to sphere  $i$ , turning particle  $i$  into a dumbbell with direction vector  $\mathbf{u}'_i$  and center of mass position  $\mathbf{r}'_i$  and particle  $j$  into a sphere at  $\mathbf{r}'_j$ . The way to do this is

$$\begin{aligned} \mathbf{u}'_i &= (\mathbf{r}_i - \mathbf{r}_{j\eta})/a, \\ \mathbf{r}'_i &= \mathbf{r}_{j\eta} + \frac{L}{2}\mathbf{u}'_i \quad \text{and} \\ \mathbf{r}'_j &= \mathbf{r}_{j\eta} - a\eta\mathbf{u}_j, \end{aligned} \tag{3.21}$$

where  $a = |\mathbf{r}_i - \mathbf{r}_{j\eta}|$ , see Fig. 3.11. Note, that the position of sphere  $\eta$  of the dumbbell is fixed during the move. Still, the first step of the bond switch move, disconnecting a dumbbell, will involve making an arbitrary choice for  $a$  and for the last step, connecting two spheres, we must choose the acceptance probability of a certain value for  $a$ . The second problem is that, although the spheres are now moved to connect and disconnect a dumbbell, the bond switch move will still fail due to overlaps with the particles which are not directly involved in the bond switch move. One can resolve this problem by combining

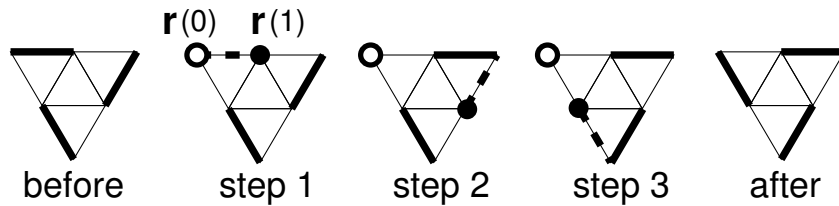


**Figure 3.10:** An example of the bond switch move on a hexagonal lattice. The dumbbells are denoted by thick lines, the loose spheres by circles:  $\mathbf{r}(0)$  by the open circle and the loose end,  $\mathbf{r}(1)$  by the filled symbol. The bond configuration is depicted at the instant just after the bond indicated by a dashed line has been disconnected and before a new bond is chosen.

the bond switch moves with displacement moves of the particles. However, in this case one has to make sure that each step in the bond switch move preserves detailed balance, while in App. 3.A only the entire bond switch move preserves detailed balance. To this end we accept the generated move with a probability of  $w(f)/w(r)$ , where  $w(f)$  is the weight  $w_i$  as occurring in a step in the bond switch move and  $w(r)$  is the weight of the reverse move.

In this case, the system consists of  $N-1$  dumbbells and 2 spheres during one part of the simulation and of  $N$  dumbbells during the other part. As a result, since the bond switch moves will consist of varying numbers of steps, the sampling, which can only occur when the system consists of only dumbbells, is biased. We, therefore, decided to use a system of  $N-1$  dumbbells and 2 spheres during the entire simulation. An additional advantage is that we do not have to bias the system anymore ( $\lambda_b = 0$ ), since the trajectory of the loose end throughout the system does not have to be closed. The results of these simulations will be nearly equal to the results of a simulations of  $N$  dumbbells provided that  $N$  is large enough and that the definitions of  $\partial F/\partial L$  and  $\rho^*$  are adjusted:  $\rho^* \equiv ((N-1)d^3 + 2\sigma^3)/V$  and we approximate  $\partial F/\partial L$  of  $N$  dumbbells to  $N/(N-1)$  times  $\partial F/\partial L$ , as measured in our system of  $N-1$  dumbbells and 2 spheres. In our simulations, we used  $N = 864$ , and we checked that  $\partial F/\partial L$  and  $\rho^*$  measured in a simulation of  $N-1$  dumbbells and 2 spheres *without* bond switch moves were nearly equal to the results of a simulations with  $N$  dumbbells, with a difference of the order of  $1/N$ .

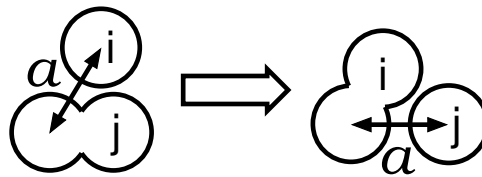


**Figure 3.11:** A typical bond switch move for a non-close-packed structure: particles are not positioned on a lattice.



---

## Hard dumbbells in gravity: structure and crystallization

---

We study the structure and phase behavior of hard dumbbells in gravity. The fluid is shown to layer near the wall, where subsequent layers of dumbbells align either preferably along or parallel to the wall. We observe coexistence of a fluid with a plastic crystal (PC) and an aligned crystal (CP1) in a single sediment for short dumbbells. For longer dumbbells, we observe a direct fluid CP1 coexistence, while for dumbbells of almost tangent spheres, the aperiodic phase appears in between the fluid and CP1. The coexistences are explained using a simple expression based on an approximation similar to the local density approximation, which was already applied to hard spheres in gravity in Chap. 2. The fluid–PC–CP1 coexistence could not be explained using this expression. We attributed this discrepancy to a lattice constant mismatch between the PC phase and the CP1 phase. Finally, we show using direct simulations that the plastic crystal stacks preferably in hcp for short dumbbells, as was already shown to be the case in a bulk plastic crystal in Chap. 3.

## 4.1 Introduction

The phase behavior of hard spheres in bulk, arguably the simplest system imaginable, is well understood by now. In particular, it was shown by computer simulations that such a system shows a purely entropy-driven phase transition from a disordered fluid phase to a face-centered-cubic (fcc) crystal phase at sufficiently high densities [3–5]. Although the fcc phase is the most stable phase, the free energy difference with respect to the metastable hexagonal-close-packed (hcp) structure is only very small and is on the order of  $10^{-3}k_B T$  per particle at the melting transition [6]. Here we define  $k_B$  as Boltzmann’s constant and  $T$  the absolute temperature. Historically, this system was mainly investigated as a model for simple atomic liquids. The advent of well controlled colloidal model systems has changed this. In fact, by screening the interactions between charged colloidal particles one can get interactions that are almost hard core-like. However, gravity is usually not negligible for colloids, which are much larger than atoms. Hence, a spatial inhomogeneous suspension is obtained due to the gravitational field, which is characterized by a density profile  $\rho(z)$  that varies with altitude  $z$ . The parameter that is associated with a gravitational field is the so-called gravitational length and reads  $\ell/\sigma = (\beta m g \sigma)^{-1}$  where  $m$  is the effective or buoyant mass of the colloidal particles,  $\beta = (k_B T)^{-1}$ ,  $\sigma$  the diameter of the colloids, and  $g$  the gravitational acceleration. Typically,  $\ell/\sigma$  is of the order of  $10^{-1} - 10^3$  for colloidal particles. The density profiles in the earliest measurements were obtained simply by counting the number of particles by eye at a certain height, for instance by Perrin [2], who used the resulting density profile to calculate Boltzmann’s constant  $k_B$  and hence Avogadro’s number. More recently density profiles have been measured by light scattering techniques [27, 28] and confocal microscopy in suspensions of colloidal hard spheres [29]. In light of these experiments on colloidal spheres and as a natural extension to the bulk hard sphere theoretical studies and simulations, one can add a gravitational field. Density profiles of hard spheres in gravity have been obtained using density functional theory and simulations [19–26].

In a sediment, the local density increases with depth and (before equilibrium is reached) with time, which leads to crystallization when the hard sphere freezing pressure is exceeded. In fact, in colloidal systems, this is probably the most widely used method to obtain crystals of micron-sized colloids [29]. Crystallization in sedimentation profiles of hard spheres was studied using Monte Carlo simulations and density functional theory [20–24, 26] and in more detail by us in Chap. 2. The simulations in Ref. [20] show a discontinuous transition where two layers crystallize at the same gravitational field strength. Upon increasing the gravitational field further, the crystalline film grows continuously. However, density functional theory predicts a discontinuous crystal growth via layering transitions upon increasing gravity in contrast with the simulation results [20]. Our Monte Carlo simulations in Chap. 2 supported the continuous layer-by-layer growth as found in the Monte Carlo simulations of [20]. Furthermore, we showed that the chemical potential,  $\mu$ , at which the  $n$ th layer crystallizes can be obtained from

$$\mu - mgz'_n = \mu_{\text{coex}}, \quad (4.1)$$

where  $\mu_{\text{coex}}$  is the chemical potential at bulk coexistence and  $z'_n$  is the height of layer  $n$ . One has some freedom of choosing this  $z'_n$ , depending on the definition of the interface.

For hard spheres the best choice was to choose  $z'_n$  in between the layer that crystallizes and the layer below, while  $z'_n = 1\sigma$  worked best for the initial simultaneous crystallization of layers 1 and 2 at  $1 < \sigma/\ell \leq 4$  and  $z'_n = 0.8\sigma$  for the crystallization of a single layer at the extreme case  $\sigma/\ell = 10$ .

Having calculated the structure and phase behavior of hard spheres in gravity, one possible next step is to investigate a more complicated particle shape. Dijkstra and Savenko [69] investigated the freezing transitions of hard rods in gravity for a  $L/D = 5$ , where  $L$  is the distance between the centers of the hemispherical end caps and  $D$  is the diameter of the caps and the cylinder. The authors find coexistences between up to four phases, a consequence of the rich phase diagram of hard rods, that features isotropic, nematic, smectic and crystal phases for this  $L/D$ . The coexistences were compared to a theoretical expression, that is similar to Eq. (4.1). However, since the calculations were performed in the canonical ensemble, the equations feature the number of particles per unit area instead of the chemical potential  $\mu$ .

While rods (in the form of viruses [70, 71]) are among the earliest colloidal systems to be studied, it is difficult to tune the aspect ratio of such systems. On the other hand it is difficult to obtain a narrow size distribution for synthetic rods. However, colloidal dumbbells can be synthesized that are monodisperse and whose aspect ratio can be tuned very easily [50]. In this method, the anisotropic particles are formed by destabilizing a dispersion of colloidal silica spheres resulting in an initial aggregation of the spheres, i.e. dumbbell formation. Subsequently, a layer of silica is grown around these cores to obtain a dumbbell of length-to-diameter ratio  $L^* = L/\sigma$ , where  $L$  is the distance between the centers of the spheres and  $\sigma$  is the diameter of the spheres. By adding salt to the solvent, the dumbbell interactions can be tuned from hard to long-range repulsive interactions. This method is especially suited for growing relatively long dumbbells. For very short dumbbells a very thick layer must be grown to sufficiently decrease  $L/\sigma$ , which results in difficulties in the synthesis, such as secondary nucleation i.e. a spontaneous nucleation and growth of silica spheres instead of growth on top of the existing cores. For short dumbbells another synthesis method is more suited [72, 73]. It is possible to swell polymer latex particles with a monomer. In suitable solvent conditions the swelling will become a bulge that protrudes from one side of the particle. By tuning the amount of monomer added, the protrusion can be grown to the same radius as the original polymer particle, such that a homonuclear dumbbell can be obtained. Subsequently, the monomer can be polymerized to solidify the particle.

In this chapter we investigate the phase behavior of dumbbells in gravity. The bulk phase diagram of dumbbells was mapped out for a large part by Vega et al. [44–46] and in Chap. 3 we investigated the phase diagram for large  $L$  which features, aside from the close packed crystal aligned CP1 also the aperiodic phase, where the spheres are on a lattice, but the dumbbells are randomly oriented. Furthermore, for small  $L$  we determined the type of plastic crystal: face centered cubic (fcc) or hexagonally close packed (hcp) by calculating free energy differences. Ref. [69] focused on coexistences between the fluid, various mesophases and one crystal phase for rods, due to their choice of  $L/D = 5$ . Instead, we will study in this work the direct fluid–aligned crystal coexistence and the fluid–disordered crystal–aligned crystal coexistence for dumbbells. The phase diagram of dumbbells is similar to short spherocylinders especially for  $L/\sigma \sim L/D \lesssim 0.6$  [46].

Therefore we expect that the results described in this chapter for dumbbells with  $L \leq 0.6\sigma$ , also apply quantitatively to short rods. The results for  $L \gtrsim 0.9\sigma$  certainly do not apply to rods, as spherocylinders do not order into an aperiodic phase. In this chapter, we show that at short  $L$  we obtain the expected fluid–plastic crystal–CP1 coexistence, at intermediate  $L$  a direct fluid–CP1 crystal coexistence and finally at large  $L$  a fluid–aperiodic crystal–CP1 coexistence. Furthermore, we show that although the free energy difference between the fcc and the hcp plastic crystal is small, we can observe by direct simulations in gravity that the hcp phase is more stable for  $L = 0.3\sigma$ .

## 4.2 Model

We consider a system of hard dumbbells consisting of spheres of diameter  $\sigma$ . The center-to-center distance between the spheres is  $L \leq \sigma$ . We denote the center-of-mass position and the orientation of dumbbell  $i$  by  $\mathbf{r}_i$  and  $\mathbf{u}_i$  respectively. The particles are subjected to a gravitational field oriented along the  $z$ -direction. In addition, the dumbbells are confined between two smooth hard parallel walls at  $z = 0$  and  $z = H$ . In other words, the dumbbells are subjected to the external potential:

$$\phi(z_i, u_{i,z}) = \begin{cases} mgz_i & z_i - L/2|u_{i,z}| > \sigma/2 \text{ and } z_i + L/2|u_{i,z}| < H - \sigma/2 \\ \infty & \text{otherwise} \end{cases} \quad (4.2)$$

where  $z_i$  is the vertical coordinate,  $u_{i,z}$  is the  $z$  component of the direction vector of particle  $i$ ,  $g$  is the gravitational acceleration, and  $m$  the buoyant mass of the hard dumbbells. All simulations in this chapter were performed at  $mg\sigma/k_B T = 2$ , so the gravitational length is equal to  $\ell = \sigma/2$ . The height  $H$  is chosen such that the number density (see Sec. 4.3) at  $z = H - \sigma/2$  is sufficiently small, i.e.,  $\rho(H - \sigma/2)d^3 < 10^{-6}$ , where  $d$  is the diameter of the sphere that has the same volume as a dumbbell and  $\rho(z)$  is the density at height  $z$ , and thus the system can be considered to be infinite in the  $z$ -direction. The lateral dimensions of the box are  $L_x = a_0 n$  and  $L_y = a_0 m\sqrt{3}/2$  with  $n, m$  integers. We choose  $n$  and  $m$  such that the lateral dimensions of the simulation box are nearly equal, which minimizes the finite-size effects for the fluid phase and still accommodates a hexagonal crystalline layer with lattice constant  $a_0$ . We employ periodic boundary conditions in the lateral dimensions in our simulations. Rather than fixing the number of particles we fix the chemical potential,  $\mu$ , by adding standard [9] particle insertion and deletion moves to our Monte Carlo simulations. We define a dimensionless chemical potential by

$$\mu^* = \beta\mu - \log(\mathcal{V}/\sigma^3) \quad (4.3)$$

where  $\mathcal{V}$  is the thermal volume. This definition is such that the dimensionless ideal gas chemical potential equals  $\log(N\sigma^3/V)$ . Equilibration of the number of crystalline layers was rather slow. This is caused by the glassy behavior at high chemical potentials, which are necessarily above the bulk coexistence chemical potentials. We often needed over  $10^7$  successive Monte Carlo moves per particle for equilibration. Equilibration was checked by comparing order parameter profiles.

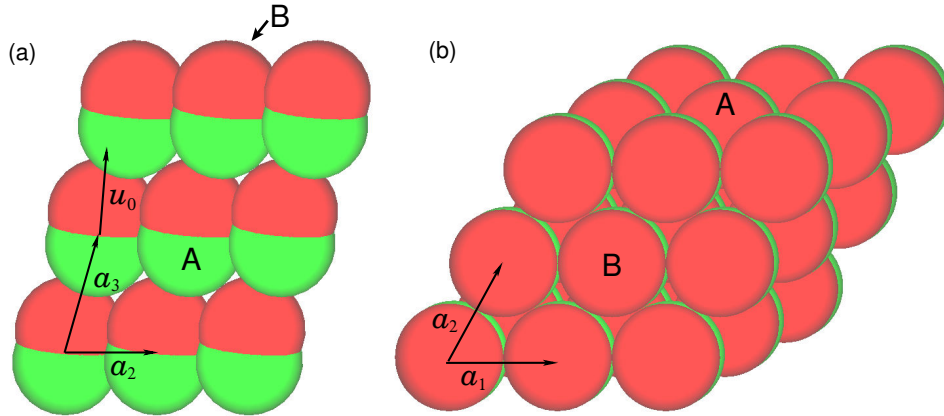


**Figure 4.1:** The CP1 crystal, its lattice vectors,  $a_1$ ,  $a_2$  and  $a_3$ , and the direction vector of the dumbbells,  $u_0$ . (a) Side view:  $\mathbf{a}_1$  points into the plane of view. (b) Top view. The A face of the crystal is spanned by  $a_1$  and  $a_3$ ; the B face is spanned by  $a_1$  and  $a_2$ . The A face is buckled i.e. one sphere of each dumbbell is closer to a plane spanned by  $a_1$  and  $a_3$ , than the other.

#### 4.2.1 Initial configuration

The close packed phase for hard dumbbells is the CP1 phase. Starting from an fcc crystal of spheres that lies on its (111) face (i.e. the  $z$ -direction is parallel to the  $[111]$  direction), CP1 can be obtained by shifting every second hexagonal layer of spheres downwards and sideways. This shift is such that each sphere of every second layer only overlaps with exactly one sphere of every first layer and remains in contact with its other neighbors. The overlapping spheres form dumbbells, that remain horizontally arranged in hexagonal layers. The other hexagonal layers of fcc are slightly deformed (buckled). The lattice vectors and the direction vector of CP1 at a given density are

$$\mathbf{a}_1 = \begin{pmatrix} a_0 \\ 0 \\ 0 \end{pmatrix} \quad \mathbf{a}_2 = \begin{pmatrix} a_0/2 \\ a_0\sqrt{3}/2 \\ 0 \end{pmatrix} \quad \mathbf{a}_3 = \begin{pmatrix} b_0 \\ b_0/\sqrt{3} \\ c_0 \end{pmatrix}, \quad \mathbf{u}_0 = \begin{pmatrix} \sqrt{3} \sin \theta_0/2 \\ \sin \theta_0/2 \\ \cos \theta_0 \end{pmatrix}, \quad (4.4)$$

where  $a_0$ ,  $b_0$  and  $c_0$  are lattice parameters and  $\theta_0$  is the angle between the  $z$ -axis and the equilibrium direction vector of the particles,  $\mathbf{u}_0$ . The CP1 crystal, its lattice vectors and  $\mathbf{u}_0$  are depicted in Fig. 4.1. For hard spheres the (111) hexagonal layers (rather than say (100) or (110)) lie parallel to a hard wall (see Chap. 2) which is a combined effect of a lower interfacial tension between the (111) face of an fcc hard sphere crystal and the wall, compared to other crystal planes [74, 75], and the gravitational energy, which is also slightly lower for the (111) face (the difference for the (100) face and the (111) face is  $mg a_0(1 - \sqrt{3}/2)/\sqrt{6}$  per particle for instance). The crystal–fluid interfacial tension does not play a major role in determining which crystal plane lies at the wall (and therefore also at the fluid–crystal interface), as this dependence on the crystal orientation of the crystal–fluid interface is weak.

When starting from a fluid configuration, we never observed the CP1 phase, although it is the stable bulk phase at high pressures for all aspect ratios. The CP1 phase is probably stable in gravity as well, since it is the close packed crystal phase. However,

the crystal probably does not nucleate spontaneously in our system, due to the slow dynamics which occurs at high pressures. This means that we have to make an educated guess as to which face of the CP1 phase lies at the wall. Unfortunately, the wall–crystal interfacial tensions have not been calculated for hard dumbbells. From the results for hard spheres we expect that one of the faces that corresponds to the (111) faces of fcc has the lowest interfacial tension. The gravitational energy expressions are a bit more cumbersome for this low symmetry crystal, therefore we only tabulate the results in Tbl. 4.1 for the lattice parameters measured near coexistence and for the close packed crystal for  $L/\sigma = 0.3, 0.6, 0.92$ . These results show that the gravitational effect on the orientation of the crystal at the wall is small, although, as it scales with the number of particles ( $N$ ), it will outweigh the interfacial tension effect, that does not scale with  $N$ , when the sediment is thicker than a certain number of layers. The fluid–crystal interfacial tension has been calculated for the fluid–CP1 coexistence [76], and is considerably more anisotropic than the interfacial tensions for hard spheres. In contrast to hard spheres, the CP1–melt interfacial tension is higher, when the hexagonal layer is in contact with the fluid, than it is when either of the buckled crystal planes is in contact with the fluid phase [76]. In light of these results, there are two likely candidates for the crystal plane at the wall, the buckled face (A), spanned by  $\mathbf{a}_1$  and  $\mathbf{a}_3$  and the flat hexagonal layer (B), spanned by  $\mathbf{a}_1$  and  $\mathbf{a}_2$ , see Fig. 4.1 (the third face, spanned by  $\mathbf{a}_1$  and  $\mathbf{a}_2$ , is equivalent to the A face). We suspect that the buckled A face at the wall is less stable because the crystal will be deformed, when the particles are pushed against the bottom wall. To check this idea, we ran a simulation starting with the A face at the wall at  $L = 0.6\sigma$ , which indeed deformed, although the deformed configuration proved to be mechanically stable. However, less stable layers form and the crystal melts into a fluid at higher chemical potential than the B candidate. From Tbl. 4.1, we see that for  $L = 0.3\sigma$  the A configuration has a lower gravitational energy than the B configuration, however the A oriented CP1 crystal melts directly into a plastic crystal at a chemical potential where the B configuration is stable. In the remainder of this chapter, we only consider simulations that were initiated in one or two initial configurations. The first initial configuration is a CP1 crystal with the hexagonal B plane at the wall, using the bulk lattice parameters at coexistence as listed in Tbl. 4.1. The second type of initial configuration is an empty simulation box ( $N = 0$ ). In this case, the number of particles will increase slowly due to exchange moves and initially the configuration of these particles will be fluid-like. Since the layers are able to shift upwards and sideways due to the periodic boundary conditions, we expect that all lattice parameters except  $a_0$  can be adjusted during the simulation. Whenever possible we started with the final configuration of a previous run, except when we consider the stability of hcp versus fcc of the plastic crystal phase. The crystallization of the aperiodic phase and the plastic crystal showed little to no hysteresis, similar to simulations of hard spheres under gravity as discussed in Chap. 2. In particular, the initial crystallization of a system starting with a fluid occurred at the same chemical potential as the melting of the last few layers when we started with a crystal phase within the statistical uncertainty.

$L/\sigma$	$a_0/\sigma$	$b_0/\sigma$	$c_0/\sigma$	$\theta_0$	$\Delta\Phi_z/(mgN\sigma)$	
					coex	cp
0.3	1.08	0.538	1.14	18.8°	-0.013	0.019
0.6	1.08	0.664	1.43	18.4°	0.0066	0.019
0.92	1.05	0.917	1.65	30.3°	0.0058	0.0051

**Table 4.1:** The lattice parameters at coexistence as a function of  $L$  and the gravitational energy difference between perfect crystals with the A and the B crystal plane (see Fig. 4.1) parallel to the bottom wall at coexistence (coex) and at close packing (cp). The gravitational energy difference is divided by  $Nmg\sigma$  to make it dimensionless. A positive energy difference implies that the A configuration is more stable.

### 4.2.2 Bond switch moves

The aperiodic phase consists of many arrangements of bonds between the particles (bond configurations) as described in Chap. 3. These arrangements are only strictly degenerate at  $L = \sigma$  and close packing i.e. only then the free energy of the dumbbells is the same for all bond configurations. As density and especially  $L$  is decreased, some of the arrangements become more frustrated than others by the fact that the bond length  $L$  between the spheres within a dumbbell is smaller than the distance between spheres of a neighboring dumbbell, which is equal to the lattice constant. For this reason when considering an aperiodic crystal at  $L < \sigma$ , it is paramount to implement a move which switches between bond configurations while preserving detailed balance. Such a bond switch move was introduced in Chap. 3 in order to sample the different arrangements of bonds according to their local free energies and therefore correctly calculate the free energy of the aperiodic crystal in the bulk. To implement bond switch moves that preserve detailed balance and still work at finite density it was necessary to add single spheres to the simulation. In short, the bond switch move consists of two steps: First, we connect a non-bonded sphere to a sphere of a neighboring dumbbell and we cut the bond of that dumbbell, effectively moving the sphere from one lattice site in the aperiodic phase to another (see Fig. 3.11 in Chap. 3). In the bond switch moves in bulk, the diameter of the spheres was set to  $\sigma$ .

As the CP1 phase can be viewed as a deformed version of fcc, it can transform into the aperiodic crystal phase using bond switch moves, provided that the layers can shift back to their positions in the fcc crystal phase. In our simulations in gravity, the top wall is far away so the layers can shift upward, when the loss of gravitational energy is overcome by the gain in entropy due to degeneracy. Furthermore, the periodic boundary conditions allow for a shift in the horizontal directions. We implemented the bond switch moves, as introduced in Chap. 3, for dumbbells under gravity and observed a successful transformation from CP1 to the aperiodic phase. There are a few differences between the implementation of these moves in gravity and in bulk (see Chap. 3), related to the (non-bonded) spheres that are required in order to be able to perform the bond switches. First, we subject the spheres to insertion and deletion moves and set their chemical potential to  $\mu^*/2 - \Delta\mu$ , where  $\mu^*$  is the reduced chemical potential of the dumbbells and  $\Delta\mu = 8$  ensures that the total fraction of single spheres is always small but nonzero. The (buoyant) mass  $m_s$  of the spheres was chosen to be half the mass of a dumbbell ( $m$ ), while the

diameters of the spheres ( $\sigma_s$ ) was chosen such that the volume of a sphere is equal to half the volume of a dumbbell. In this way the internal mass densities of spheres and dumbbells are equal and separation of the dumbbells and the spheres by gravity should be minimal, according to Archimedes' principle. Moreover, the acceptance ratio of the bond switch moves increases as the probability of creating an overlap with a particle that is not involved in the bond switch move is lower if we move a smaller particle.

### 4.3 Methods

In order to analyze our simulation results, we calculate two types of density profiles: One that measures the height distribution of the centers of mass of the dumbbells:  $\rho_{\text{com}}(z)^* = \langle \frac{d^3}{A} \sum_i \delta(z - z_i) \rangle$  and one that measures the height distribution of the individual spheres of each dumbbell:  $\rho_{\text{sphere}}^* = \langle \frac{d^3}{A} \sum_i \frac{1}{2} \sum_{\eta} \delta(z - z_{i,\eta}) \rangle$ , where  $d$  is the diameter of a sphere with the same volume as a dumbbell, which is given by  $\frac{\pi}{6}(\sigma^3 + 3L\sigma^2/2 - L^3/2)$ . Similarly, all order parameter profiles can either be defined for the center-of-mass of the dumbbells or for the individual spheres of each dumbbell. To lighten the notation, we use the following definitions to abbreviate the averaging over the delta functions in the definitions of the order parameter profiles:  $\langle A_i \rangle_{z,\text{com}} \equiv \langle \sum_i A_i \delta(z - z_i) \rangle / \langle \sum_i \delta(z - z_i) \rangle$  and  $\langle A_i \rangle_{z,\text{sphere}} \equiv \langle \sum_{i,\eta} A_{\{i,\eta\}} \delta(z - z_{i,\eta}) \rangle / \langle \sum_{i,\eta} \delta(z - z_{i,\eta}) \rangle$ , where  $A_i$  is any measurable property of particle  $i$  and  $A_{\{i,\eta\}}$  is a property of sphere  $\eta = \pm 1$  of dumbbell  $i$ . To study the orientational order of the dumbbells, we measure the tensor  $Q_{\alpha\beta}(z) = \langle \frac{3}{2} u_{i,\alpha} u_{i,\beta} - \frac{1}{2} \delta_{\alpha\beta} \rangle_{z,\text{com}}$ , with  $\alpha, \beta = x, y, z$ . We use the  $zz$  component of  $Q(z)$  to investigate the alignment along the  $z$  axis ( $Q_{zz}(z) = 1$ ) or perpendicular to  $z$  ( $Q_{zz} = -1/2$ ). We define the nematic order parameter at height  $z$ ,  $S_2(z)$ , as the largest eigenvalue of  $Q(z)$ . For a fluid with a uniaxial rotation symmetry of the director field, as in the case of a fluid of dumbbells near a wall, one can show that  $Q_{xx} = Q_{yy} = -\frac{1}{2}Q_{zz}$  and all other components of  $Q$  are zero, where  $z$  is the axis of the rotational symmetry. All dumbbells very close to the wall ( $z_i \simeq \sigma/2$ ) are oriented nearly parallel to the wall (otherwise they would overlap with the wall, see Eq. (4.2)). Therefore,  $S_2(\sigma/2) = Q_{xx}(\sigma/2) = -\frac{1}{2}Q_{zz}(\sigma/2) \simeq \frac{1}{4}$ . We use  $S_2(z)$  to distinguish between the CP1 phase ( $S_2 \simeq 1$ ) and the plastic crystal ( $S_2 = 0$ ). In the aperiodic phase, the bonds that connect two spheres in adjacent layers correspond to dumbbells that are upright and whose center of mass position is in between the layers. Therefore, the value of  $S_2(z)$  in between two layers is nonzero. Consequently, we can not use  $S_2(z)$  to distinguish between the CP1 phase and the aperiodic crystal. Instead, we define the bond directional order,  $S_{\text{bond}}(z) = |\langle \eta \mathbf{u}_i \rangle_{z,\text{sphere}}|$ . This order parameter is 1 for the perfect CP1 phase, since in a given layer of spheres  $\eta \mathbf{u}_i$  is always the same. In the aperiodic phase the bonds are randomly oriented, so  $S_{\text{bond}} = 0$ . To determine crystallization, we measure the hexagonal bond order parameter of dumbbell  $\gamma = i$  or sphere  $\gamma = \{i, \eta\}$  using

$$\psi_{6,\gamma} = \frac{1}{N_\gamma} \sum_{\lambda=1}^{N_\gamma} \exp(i6\theta(\mathbf{r}_{\gamma\lambda})), \quad (4.5)$$

where the bond angle  $\theta(\mathbf{r}_{\gamma\lambda})$  is defined as the angle between a reference axis and the center-of-mass displacement vector,  $\mathbf{r}_{\gamma\lambda} = \mathbf{r}_\lambda - \mathbf{r}_\gamma$  and the sum over  $\lambda$  runs over the  $N_\gamma$

nearest neighbors of  $\gamma$ . A particle is defined as a neighbor, when

$$x_{\gamma\lambda}^2 + y_{\gamma\lambda}^2 + (4z_{\gamma\lambda})^2 < (1.4\sigma)^2, \quad (4.6)$$

where  $x_{\gamma\lambda}$ ,  $y_{\gamma\lambda}$  and  $z_{\gamma\lambda}$  are the respective  $x$ ,  $y$  and  $z$  components of  $\mathbf{r}_{\gamma\lambda}$ . This criterion is chosen in such a way, that the neighbors  $\gamma$  are located primarily in the same layer as particle  $\lambda$

The center of mass hexagonal bond order profile is defined as

$$\psi_6^{\text{com}}(z) = |\langle \psi_{6,i} \rangle_{z,\text{com}}|. \quad (4.7)$$

This parameter considers (virtual) bonds between the center of mass of a dumbbell and the centers of mass of its neighbors. It is 1 if the centers of mass of all dumbbells at height  $z$  are hexagonally ordered. Similarly, the hexagonal bond order profile of the spheres is defined as

$$\psi_6^{\text{sphere}}(z) = |\langle \psi_{6,\{i,\eta\}} \rangle_{z,\text{sphere}}|. \quad (4.8)$$

In this case, bonds between sphere  $\eta$  of dumbbell  $i$  and neighboring spheres are considered. These neighbors can be part of another dumbbell or belong to the same dumbbell  $i$ .  $\psi_6^{\text{sphere}}(z) = 1$  if the spheres of the dumbbells are perfectly hexagonally ordered.

In bulk systems, plastic crystals were found to stack either like fcc or hcp. To distinguish between the two types of stacking we use the  $\psi_3$  order parameter, which was used in Ref. [77] to study crystallization in sediments of colloidal spheres. We require the local trigonal ordering in the layer above (+) or below (−) dumbbell  $i$  to define the trigonal bond orientational order parameter  $\psi_3^\pm$ :

$$\psi_{3,i}^\pm = \frac{1}{N_\pm} \sum_j^{N_\pm} \exp(3i\theta(\mathbf{r}_{ij})), \quad (4.9)$$

where the sum over  $j$  runs over the  $N_\pm$  neighbors of dumbbell  $i$  in the layer above (+) or below the particle (−). In this case, a particle is deemed a neighbor when its horizontal distance to particle  $i$  is smaller than  $1.1\sigma$  and its vertical distance is between  $0.65\sigma$  and  $1.4\sigma$ . If particle  $i$  is in a perfect fcc environment,  $\psi_{3,i}^+ = -\psi_{3,i}^-$ , while in an hcp environment  $\psi_{3,i}^+ = \psi_{3,i}^-$ . Accordingly, the  $\psi_3$  profiles that are sensitive to hcp resp. fcc are defined as follows

$$\left. \begin{array}{l} \psi_3^{\text{hcp}}(z) \\ \psi_3^{\text{fcc}}(z) \end{array} \right\} = \left\langle \frac{1}{2} |\psi_{3,i}^+ \pm \psi_{3,i}^-| \right\rangle_{z,\text{com}}. \quad (4.10)$$

## 4.4 Results

### 4.4.1 Structure

We perform Monte Carlo simulations of a fluid of hard dumbbells with elongation  $L = 0.3\sigma$ ,  $L = 0.6\sigma$  and  $L = 0.92\sigma$ . Here and in the remainder of the chapter we set the gravitational length  $\ell$  to  $\sigma/2$ . We measure the dimensionless density profiles for the center-of-mass of the dumbbells,  $\rho_{\text{com}}^*(z)$ , and for the individual spheres of each dumbbell,  $\rho_{\text{sphere}}^*(z)$  and the order parameter profile  $Q_{zz}(z)$ , that measures the alignment parallel

( $Q_{zz}(z) = 1$ ) and perpendicular  $Q_{zz}(z) = -1/2$  to the  $z$ -axis. In Fig. 4.2, we show these profiles for  $L = 0.3\sigma$  and  $\mu^* = 20$ , for  $L = 0.6\sigma$  and  $\mu^* = 40$  and for  $L = 0.92\sigma$  and  $\mu^* = 34$ , somewhat below the respective freezing transitions. From Fig. 4.2, we clearly observe pronounced layering in the density profiles, but the precise details depend heavily on  $L$ : For short dumbbells, the center of mass density profile resembles the density profiles obtained in sedimentation of hard spheres (with some effective diameter), while the density profile of the individual spheres of each dumbbell has a small bump at  $z = L$  that corresponds to upright particles. The  $Q_{zz}(z)$  profile in Fig. 4.3, shows oscillations that seem to be out of phase with the oscillations in the density profile. To be exact, there is a minimum in  $Q_{zz}(z)$  at a slightly lower  $z$ -position than a maximum in the center-of-mass density profile, and also a maximum in  $Q_{zz}(z)$  just below a minimum in  $\rho_{\text{com}}^*(z)$ . This is caused by the fact that upright dumbbells that stand on top of a layer have a slightly higher  $z$ -position (of their center of mass) than dumbbells that lie flat on the same layer. For very long dumbbells ( $L = 0.92\sigma$ ), the spheres of each dumbbell show the usual type of layering, while the center of mass profile has an unusual structure. From Fig. 4.2, we find density peaks in  $\rho_{\text{com}}^*(z)$  at intermediate values of  $z$  i.e.  $\frac{\sigma+L}{2}$ ,  $\frac{3(\sigma+L)}{2}$ , etc. (the position of the wall is at  $z = 0$  so the smallest possible  $z$ -position is  $\sigma/2$ ). In addition, Fig. 4.2 shows that the layering in  $\rho_{\text{com}}^*(z)$  correlates with the oscillations in  $Q_{zz}$ . The odd numbered density peaks in  $\rho_{\text{com}}^*(z)$  correspond to particles that are aligned on average perpendicular to  $z$  ( $Q_{zz}(z) = -1/2$ ), while the even numbered layers are aligned parallel to  $z$  ( $Q_{zz}(z) = 1$ ). This is caused by the fact that dumbbells with each sphere in a different layer are aligned along  $z$  and have a center-of-mass position that is in between two layers of spheres, while dumbbells with both spheres in the same layer have their direction vector perpendicular to the  $z$ -axis and their center-of-mass  $z$ -position in a layer. For intermediate length  $L = 0.6\sigma$ , the dumbbells show a complicated behavior that shows aspects of both the short dumbbell and the long dumbbell profiles.

We also measure the density profiles and hexagonal order parameter profiles for crystalline sediments of hard dumbbells with the same elongations as for the fluid:  $L/\sigma = 0.3$ ,  $0.6$  and  $0.92$ . Fig. 4.4 shows the formation of crystalline layers at the bottom of the sample, which can be seen from the negligible density in between the layers and the sharp peaks in the profiles. At  $L = 0.3\sigma$  the center-of-mass profile shows well defined layers that are about  $\sigma$  apart for all heights. A small jump in the  $\psi_6$  order parameter profile can be observed, which marks the transition from the CP1 crystal at low  $z$  to the plastic crystal further up in the sediment. It can be seen from Fig. 4.4 that peaks in the density profile of the plastic crystal (PC) are lower and less sharp, corresponding to larger fluctuations of the positions of the dumbbells. This also explains the slightly lower value of  $\psi_6^{\text{com}}$  for the plastic crystal. A similar jump in the hexagonal order parameter profile of the spheres,  $\psi_6^{\text{sphere}}(z)$ , can be observed for  $L = 0.92\sigma$ , corresponding to the CP1 to aperiodic crystal transition. Here the  $\rho_{\text{com}}^*(z)$  profile of the CP1 phase (only two layers of dumbbells) has an interlayer spacing of almost  $2\sigma$ , while the aperiodic crystal peaks are separated by half the diameter. Half of the peaks of the aperiodic phase are caused by the bonds which connect spheres within a layer of spheres and therefore the center of mass of the dumbbell is within the layer. The other half of the peaks is caused by inter-layer bonds. The center of mass profile of the aperiodic phase looks rather ragged i.e. the peaks heights differ, because the number of inter-layer bonds and the number of intra-layer bonds are not equal.

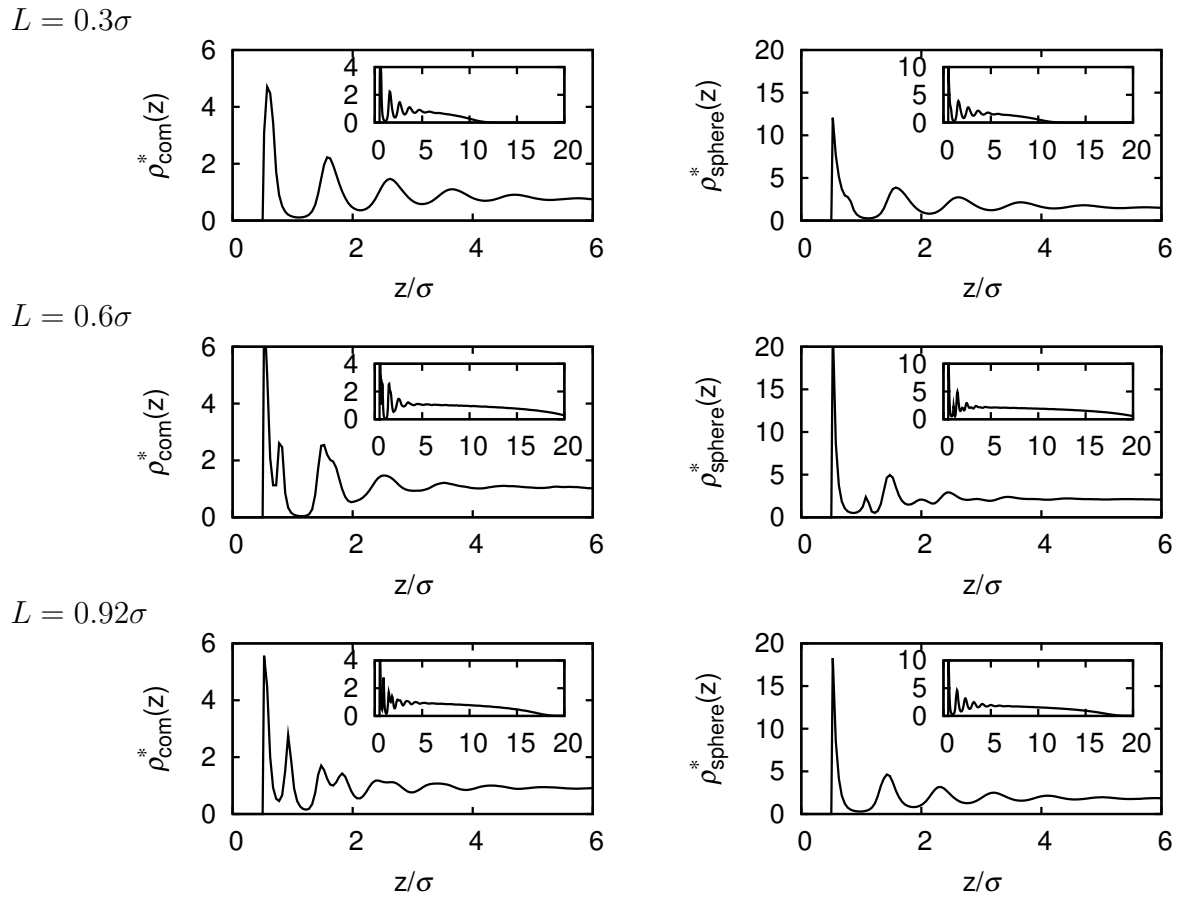


**Figure 4.2:** Dimensionless density profiles for the center of mass of the dumbbells  $\rho_{\text{com}}^*(z)$  and for the individual spheres of the dumbbells of a fluid at  $\mu^* = 20$  and  $L = 0.3\sigma$  (top),  $\mu^* = 40$  and  $L = 0.6\sigma$  and  $\mu^* = 34$  and  $L = 0.92\sigma$  (bottom). The insets show the decay of the profiles over the full sediment.

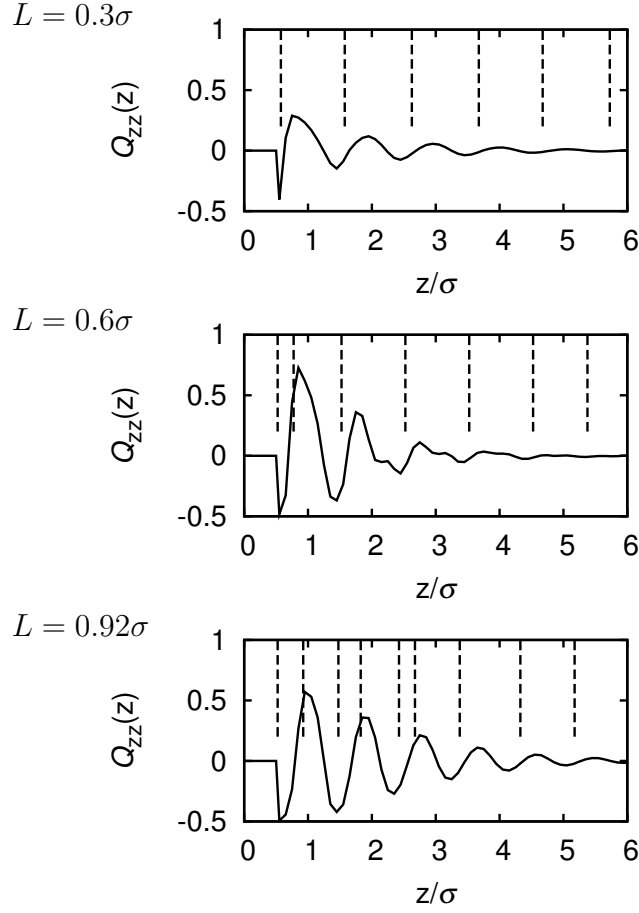


**Figure 4.3:** Orientational order parameter profiles  $Q_{zz}(z)$  of a fluid for the same parameters as in Fig. 4.2. The positions of the maxima of the center-of-mass density profiles,  $\rho_{\text{com}}^*(z)$  (see Fig. 4.2) are indicated by vertical dashed lines.

For these reasons, it is more convenient to use the hexagonal order parameter profile for the individual spheres, rather than the hexagonal order parameter profile for the centers of mass of the dumbbells. The  $\psi_6^{\text{spheres}}(z)$  profile shows pronounced ordering for both the CP1 and the aperiodic crystal phase. In conclusion, we find a triphasic coexistences both for small  $L$  and for large  $L$ , which is a nice consequence of the phase diagram of dumbbells compared to that of hard spheres. At the intermediate value of  $L = 0.6\sigma$  we observed a sediment containing only the CP1 phase and the fluid phase, as expected from the bulk phase diagram of hard dumbbells.

#### 4.4.2 Crystallization

We now study the crystallization of the fluid layers at the bottom wall. To this end, we measure the nematic order parameter profile  $S_2(z)$  at small  $L$  and the bond orientational profile at large  $L$ . Instead of showing the profiles themselves, we show the values of the relevant order parameters at the height of each layer (defined using the maxima of the profile) as a function of  $\mu$  in Fig. 4.5. We define the  $z$ -position of the  $n$ th layer,  $z_n$ , of the

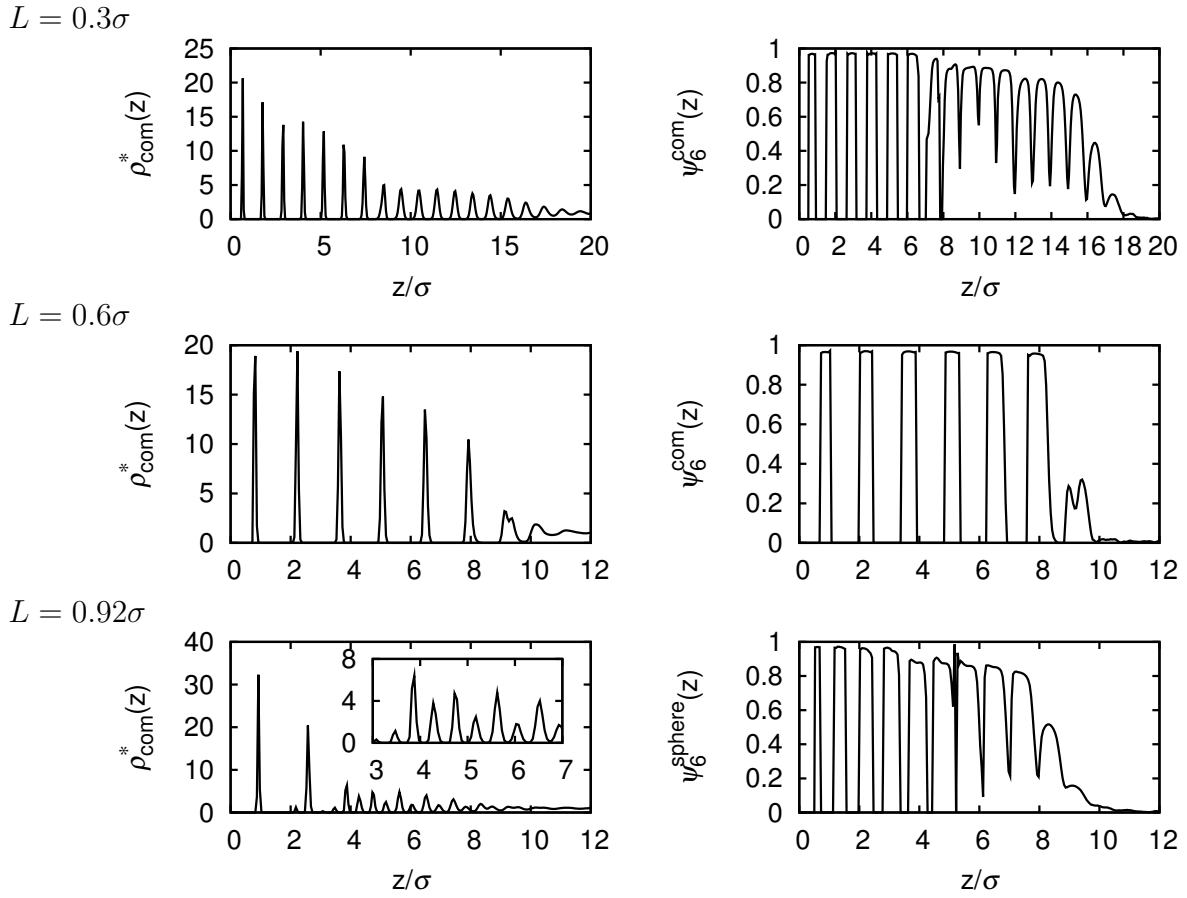


**Figure 4.4:** Center-of-mass density profile  $\rho_{\text{com}}^*(z)$  and hexagonal order parameter profile  $\psi_6^{\text{com}}(z)$  for dumbbells with  $L = 0.3\sigma$  at  $\mu^* = 55$  (top row), and with  $L = 0.6\sigma$  at  $\mu^* = 54$  (middle row), the center-of-mass density profile  $\rho_{\text{com}}^*(z)$  and hexagonal bond order profile  $\psi_6^{\text{sphere}}(z)$  of the individual spheres of dumbbells with  $L = 0.92\sigma$  at  $\mu^* = 54$  (bottom row). The inset in the bottom left plot is an enlargement of part of the  $\rho_{\text{com}}^*(z)$  profile, showing oscillations with a period  $\sim 0.5\sigma$  in the aperiodic crystal.

aperiodic phase as the position of  $n$ th maximum of  $\rho_{\text{sphere}}^*(z)$ , i.e. layer  $n$  is the  $n$ th layer of spheres for  $L = 0.92\sigma$ , while at  $L = 0.3\sigma$  and  $L = 0.6\sigma$  we number the layers of dumbbells via the maxima in the center-of-mass density profile,  $\rho_{\text{com}}^*(z)$  and, correspondingly,  $z_n$  is the  $z$ -position of the  $n$ th maximum in the center-of-mass profile. Fig. 4.5 shows that the initial crystallization of all crystal phases appears to be discontinuous, while the following layers freeze continuously, except for the CP1 crystal, where all layers seem to crystallize discontinuously. We define a layer at height  $z$  to be crystalline if  $\psi_6(z)$  is larger than 0.5, while we define a crystalline layer to be CP1 if the orientational parameter,  $S_2(z)$  or  $S_{\text{bond}}(z)$ , is larger than 0.5. Using these definitions, we find for  $L = 0.3\sigma$  that the first two layers crystallize at the same chemical potential from the fluid phase to the plastic crystal ( $\psi_6^{\text{com}} \simeq 0.8$  and  $S_2 < 0.5$ ) between  $\mu^* = 24.5$  and 25.0, and these two layers transform into a CP1 phase ( $\psi_6^{\text{com}} \simeq 0.95$  and  $S_2 \simeq 0.9$ ) between  $\mu^* = 31$  and 32. For  $L = 0.6\sigma$ , we observe that only a single fluid layer crystallizes into CP1 ( $\psi_6^{\text{com}} \simeq 0.9$  and  $S_2 \simeq 0.85$ ) between  $\mu^* = 41.50$  and 42.0. For very long dumbbells ( $L = 0.92\sigma$ ), two fluid layers (of spheres) crystallize simultaneously into the aperiodic crystal ( $\psi_6^{\text{spheres}} \simeq 0.8$  and  $S_{\text{bond}} \simeq 0$ ) between  $\mu^* = 38$  and 39, while one layer of dumbbells transforms into the CP1 crystal ( $\psi_6^{\text{spheres}} \simeq 0.95$  and  $S_2 \simeq 0.55$ ) between  $\mu^* = 48.5$  and 49.5. The nonzero value of  $S_2(z)$  for the first and second layer of the fluid and the plastic crystal is caused by particles parallel to the wall, and not by an alignment within the plane (see Methods section). Note, that also the first layer of the fluid on top of the CP1 crystal at  $L = 0.6\sigma$  has a nonzero value of  $S_2(z)$ , which implies that the dumbbells in this fluid layer are parallel to the fluid-CP1 interface.

The chemical potential at which the first few layers freeze,  $\mu_{\text{trans}}^*$ , is compared to the bulk coexistence chemical potential in Fig. 4.6 and tabulated in Tbl. 4.2. For  $L = 0.6\sigma$  and  $L = 0.92\sigma$ ,  $\mu_{\text{trans}}^*$  corresponds nicely to the bulk values, which gives confidence in the equilibration. However, for  $L = 0.3\sigma$  the PC-CP1 freezing transition is far off. To investigate this discrepancy, we investigate the structure of a fluid-PC-CP1 sediment at  $\mu^* = 35$ , where we did not expect to find any stable CP1 crystal phase. From the structure of one layer of plastic crystal we observe that the lattice direction of the plastic crystal conforms to that of the CP1 phase and to the simulation box. Furthermore, we find that the PC layer in contact with the CP1 crystal has a horizontal lattice constant of about  $1.18\sigma$ , which is significantly smaller than the lattice constant of the bulk plastic crystal at the PC-CP1 coexistence, which is about  $1.2\sigma$ . The other layers of the plastic crystal phase have a lattice constant of about  $1.24\sigma$ , similar to the lattice constant in the bulk at the fluid-PC coexistence. In other words, the plastic crystal forms two crystallites, one is adjusted to the fluid, while the other one is compressed due to presence of the CP1 crystal. Because of the small amount of layers, the free energy penalty for having a grain boundary inside the plastic crystal is considerable and perhaps enough to decrease the stability of the plastic crystal compared to the bulk. Furthermore, the diminished lattice constant of the lower plastic crystal compared to the bulk crystal at the PC-CP1 coexistence, explains why the height of the PC-CP1 freezing transition is affected more than the fluid-PC freezing transition.

To test that the unexpected lattice constants of the plastic crystal are not caused by the horizontal dimensions of the simulation box, we ran simulations with varying box dimensions corresponding to  $10 \times 10$ ,  $14 \times 16$  and  $20 \times 20$  particles in a layer of the initial

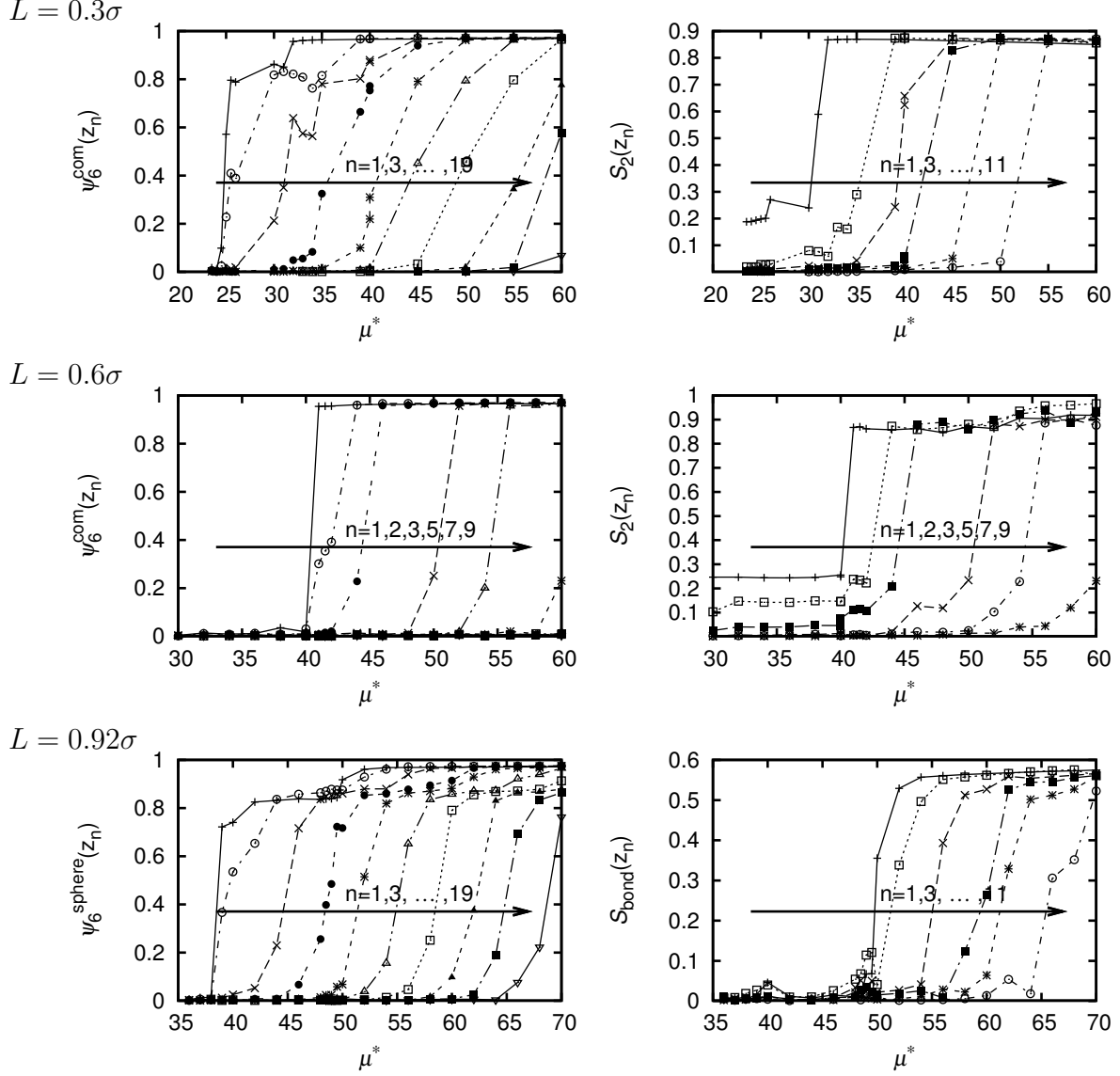


**Figure 4.5:** Order parameters at height  $z_n$  of layer  $n$ , where  $z_n$  is defined as the  $n$ th maximum of  $\rho_{\text{com}}^*(z)$  (top and middle row) or  $\rho_{\text{spheres}}^*(z)$  (bottom row). Accordingly, the layers are defined as layers of dumbbells for the top and the middle figures and as layers of spheres for the bottom figures. Top: center of mass hexagonal order parameter  $\psi_6^{\text{com}}(z_n)$  (left), nematic order parameter  $S_2(z_n)$  (right) at  $L = 0.3\sigma$ . Middle:  $\psi_6^{\text{com}}(z_n)$  (left) and  $S_2(z_n)$  (right) at  $L = 0.6\sigma$ . Bottom: hexagonal order parameter  $\psi_6^{\text{sphere}}(z_n)$  of the individual spheres of each dumbbell (left) and bond orientational order  $S_{\text{bond}}(z_n)$  (right) at  $L = 0.92\sigma$ . The order parameters of the second layer do not differ significantly from the order parameters of the first layer, except for  $L = 0.6\sigma$  (middle row). For clarity, we only show odd  $n$  for all values of  $L$ , augmented by  $n = 2$  for  $L = 0.6\sigma$ .

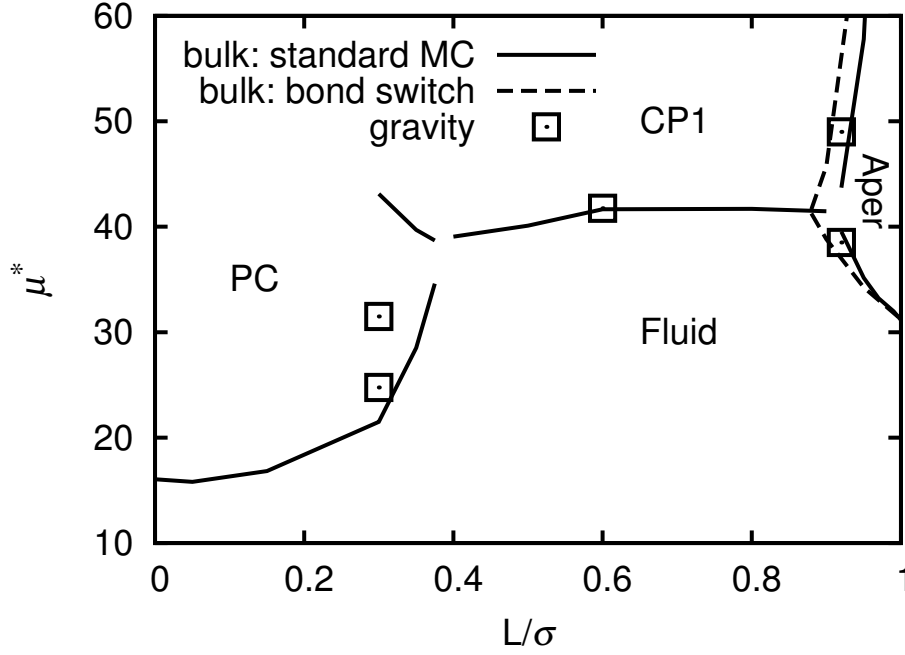


**Figure 4.6:** Bulk phase diagram for hard dumbbells in the  $\mu^*$ - $L/\sigma$  representation, where  $\mu^*$  is the bulk chemical potential nondimensionalized by Eq. (4.3) and the results indicated by the solid lines are obtained in standard Monte Carlo simulations without special moves, while bond switch moves were employed for the results indicated by the dashed lines. The squares denote the dimensionless chemical potentials ( $\mu^*$ ) at which the phase transitions occur in a gravitational field with strength  $g^* = \sigma/\ell$  equal to 2 (here and in the rest of the chapter). Fluid denotes the fluid phase, PC denotes the plastic crystal phase, CP1 the periodic crystal and Aper the aperiodic crystal phase.

CP1 crystal. The  $10 \times 10$  system is chosen in such a way, that the plastic crystal can only form layers of  $9 \times 9$  particles, which results in the right lattice constant for PC–CP1 coexistence. As expected, the CP1 phase is less stable in this case. However, if we scale up the system by a factor of two in both horizontal directions ( $20 \times 20$ ), we get the same results as for the  $14 \times 16$  system, which are shown in Figs. 4.4 and 4.5. This gives us some confidence that our results are not affected by finite size effects, but in stead are due to the mismatch between the plastic crystal and the CP1 lattice. In comparison, the aperiodic crystal has a lattice constant that is very similar to the lattice constant of the CP1 phase. Therefore, such a mismatch plays a smaller role, which can be seen from the excellent agreement between the freezing transition in bulk and in gravity. Another possibility for the anomalous behavior of the PC–CP1 transition is the slow thermalization. In order to speed up the equilibration of the aper–CP1 transition we introduced the bond switch moves. For the PC–CP1 transition at  $L = 0.3\sigma$  we were unable to implement such moves. However, if we the simulation for ten times more cycles, again at  $\mu^* = 35$ , we find no change in the number of crystalline layers and hence we do not attribute the deviation to thermalization problems.

Now, we compare our results for the freezing of the  $n$ th layer with the estimate that

layer  $n$  crystallizes when

$$\mu - mgz_n = \mu_{\text{coex}} \quad (4.11)$$

where  $\mu_{\text{coex}}$  is the chemical potential at bulk coexistence and  $z_n = \Delta z(n - 1)$ , where  $\Delta z$  is the thickness of a layer. According to this definition,  $z_n$  is the  $z$ -position in between layers  $n$  and  $n - 1$ . The thickness  $\Delta z$  is obtained from a fit of  $z_k$  as a function of the number of crystalline layers ( $N_{\text{layers}}$ ), where  $k$  is the top layer of the crystal of interest. The resulting layer thicknesses are tabulated in Tbl. 4.2. Note that for the plastic crystal and the aperiodic phase,  $k$  is not equal to  $N_{\text{layers}}$ , when there are also layers of the CP1 crystal phase present in the sediment. The expression for the chemical potential at which the  $k$ th layer crystallizes, Eq.4.11 for  $n = k$ , can be inverted to obtain the number of crystalline layers as a function of  $\mu$ :

$$N_{\text{layers}}(\mu) = \lfloor (\mu - \mu_{\text{coex}})/(mg\Delta z) \rfloor + 1, \quad (4.12)$$

where  $\lfloor x \rfloor$  is the largest integer smaller than  $x$ . The number of crystalline layers and the prediction (4.12) are plotted in Fig. 4.7. As before, we plot the number of layers of spheres in Fig. 4.7 at  $L = 0.92\sigma$ , while for the other values of  $L$  we plot the number of dumbbell layers. At  $L = 0.92\sigma$ , we used the average of the two bulk chemical potentials (one with bond switch moves and one without) for  $\mu_{\text{coex}}$  in Eq. 4.12. The agreement between the prediction (4.12) and the data is reasonable except for  $L = 0.3\sigma$ . Furthermore, the slope is correctly predicted for all  $L$ . For  $L = 0.3\sigma$ , the number of layers of CP1 ( $N_{\text{CP1}}$ ) is similarly affected by the mismatch between the plastic crystal lattice and the CP1 lattice as the PC-CP1 transition itself. To quantify this mismatch we fit Eq. (4.12) to  $N_{\text{CP1}}$  with  $\mu_{\text{coex}}$  as the only fit parameter; the result for the chemical potential  $\mu_{\text{coex}}$  was 31.4, while the chemical potential at bulk PC-CP1 coexistence is 43.12. It should be noted, that Eq. (4.12) with adjusted  $\mu_{\text{coex}}$  might not give the correct result for other values of the gravitational length  $\ell$ .

In experiments, the chemical potential is usually not readily available, although it has been obtained in a (mass) density matched suspension in ref. [78] using a variant of the Widom particle insertion method [79]. However, the pressure can be easily obtained by integrating the density profile from the ideal gas at the top of the sediment to the height of interest. We checked for hard spheres, for the center of mass profile of dumbbells and for  $\rho_{\text{sphere}}^*(z)/2$  that the pressure at height  $z$  obtained by this integration oscillates around the bulk pressure that corresponds to the chemical potential  $\mu - mgz$ . These unavoidable oscillations are caused by the layering, but we noticed that the pressure at the peak of the density profile as well as the pressure right in the middle between two layers,  $P(z'_n)$ , corresponds almost exactly to the bulk pressure at those heights. This is a nontrivial result, since the gravitational field is rather strong ( $\ell/\sigma = 0.5$ ). Using this result, we can say that layer  $n$  will be crystalline, when the pressure exactly in between layers  $n$  and  $n - 1$ ,  $P(z'_n)$  is higher than the bulk coexistence pressure. In the case of the CP1 at  $L = 0.3\sigma$ , the fitted  $\mu_{\text{coex}}^* = 31.4$  can be inserted in Eq. (4.11) to obtain the chemical potential at which a layer crystallizes. As mentioned, this chemical potential is much lower than the chemical potential at bulk PC-CP1 coexistence, therefore we have no bulk pressure data at this chemical potential. Instead, we use the local pressure  $P(z'_n)$  as a function of local chemical potential  $\mu(z'_n) = \mu - mgz'_n$  in our sediment. Using the result,

$L/\sigma$	phase	$\mu_{\text{trans}}^*$	$\mu_{\text{coex}}^*$	$\Delta z/\sigma$
0.3	PC	$24.75 \pm 0.25$	21.50	1.14
0.3	CP1	$31.5 \pm 0.5$	43.12	1.13
0.6	CP1	$41.75 \pm 0.25$	41.66	1.42
0.92	aper	$38.50 \pm 0.5$	38.47	0.83
0.92	CP1	$49.0 \pm 0.5$	49.15	0.78

**Table 4.2:** The phases found in our simulations versus the center-to-center distance to diameter ratio ( $L/\sigma$ ), the lowest chemical potential at which they were found ( $\mu_{\text{trans}}^*$ ) and the parameters describing the number of layers (see Eq. (4.12)). These parameters are: the chemical potential of the coexistence between the phase of interest and the phase at lower density (see Fig. 4.6) and the thickness of the layers  $\Delta z$ . The expression (4.12) with the parameters as listed here, underestimates the number of layers of CP1 at  $L = 0.3\sigma$  (see text). At  $L = 0.92\sigma$ ,  $\Delta z$  is the thickness of a layer of spheres.

$d^3P(z)/k_BT \simeq 27$  at  $\mu^*(z) = 31.4$ , we can conclude that layer  $n$  will be crystalline when,

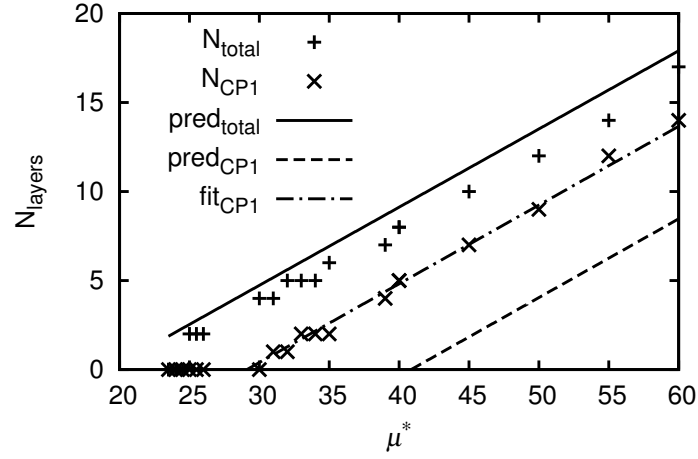
$$P(z'_n) > P_0, \quad (4.13)$$

where  $P_0$  is equal to the coexistence pressure (see Chap. 3 and Refs. [44–46]), except for the PC–CP1 transition at  $L = 0.3\sigma$  where  $d^3P_0/k_BT \simeq 27$ .

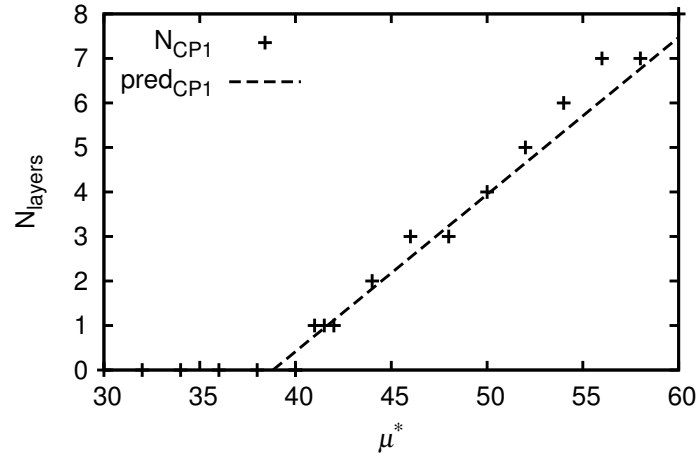
#### 4.4.3 Plastic crystal: hcp or fcc?

The plastic crystal phase of dumbbells can stack in either hcp or fcc. The free energy difference between these two phases in bulk is small ( $\lesssim 0.01Nk_BT$ ), but still much larger than the free energy difference between the fcc and hcp phases of hard spheres (difference is of order  $10^{-3}k_BT$  per particle). Furthermore, the stable phase for dumbbells of any appreciable aspect ratio ( $L > 0.1\sigma$ ) is hcp, while the stable phase for hard spheres is fcc. We investigated whether the small free energy difference between the two types of plastic crystals can be observed in a spontaneously crystallized sediment i.e. starting from a fluid phase. We initiated all runs with zero particles; the number of particles slowly increases during the simulation due to insertion moves. In this case, it is in fact advantageous that the CP1 phase never forms spontaneously, as it allows us to investigate higher chemical potentials than the plastic crystal–CP1 coexistence. In Fig. 4.8 we show the probability to find an hcp layer as obtained from  $\psi_3^{\text{hcp}}/(\psi_3^{\text{fcc}} + \psi_3^{\text{hcp}})$  for layers  $n = 2, 3$  and 4 for hard dumbbells with  $L = 0.3\sigma$  and gravitational field strength  $\ell = \sigma/2$ . We ran 10 simulations at each chemical potential, therefore the measured probabilities are multiples of 0.1. We indeed find that the probability to find an hcp layer is higher than the probability to find an fcc layer, although for higher chemical potentials the data is rather noisy because of the slow equilibration at high pressure. Using the bulk free energy differences between hcp and fcc for hard dumbbells as determined in Chap. 3, one can estimate the probability to find an hcp layer in the bulk. The probability that one layer in the bulk, consisting of  $N_l$  particles, is hcp stacked is given by  $P_{\text{hcp}} = \exp(-\beta N_l f_{\text{hcp}})/(\exp(-\beta N_l f_{\text{hcp}}) + \exp(-\beta N_l f_{\text{fcc}})) = 1/(1 + \exp(\beta N_l \Delta f))$ , where  $f \equiv F/N$  is the bulk free energy per particle, and where the surface tension between fcc

$$L = 0.3\sigma$$



$$L = 0.6\sigma$$



$$L = 0.92\sigma$$

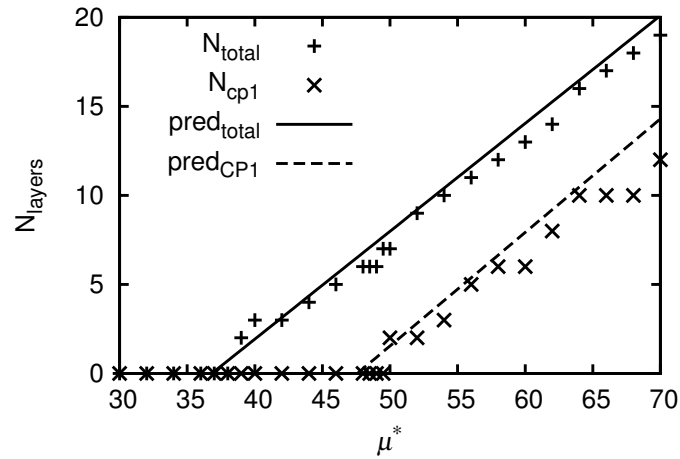


**Figure 4.7:** The number of CP1 crystalline layers and the total number of crystalline layers as a function of reduced chemical potential  $\mu^*$  for (from top to bottom)  $L = 0.3\sigma$ ,  $0.6\sigma$  and  $0.92\sigma$ . The lines labeled by “pred” denote our prediction 4.12 based on the chemical potential at bulk coexistence, while “fit” denotes a fit (see text).

and hcp (which is only known for hard spheres [80]) is ignored. We fit  $\Delta f = (F_{\text{fcc}} - F_{\text{hcp}})/N$  to the bulk free energy difference as a function of  $\rho$  and  $L$ . For  $L = 0.3\sigma$  it is always positive and of order  $0.01k_B T$  per particle. Subsequently, we fit the density as a function of the chemical potential in the bulk and use this expression in the fitted free energy difference to get a free energy difference as a function of the chemical potential ( $\Delta f(\mu)$ ). We use this expression as an approximation for the free energy difference between hcp and fcc for a single layer in our sediment even though it is only valid for a system that is thermodynamically large in all dimensions. Using a variant of the local density approximation,  $F(z) = F_{\text{bulk}}(\mu - mgz)$ , the free energy difference of a layer at height  $z_n$  is found to be  $\Delta f(\mu - mgz_n)$ . Inserting this free energy difference in the expression for the probability, we obtain  $P_{\text{hcp}}(z_n) = 1/[1 + \exp(\beta N_l \Delta f(\mu - mgz_n))]$ , where  $N_l = 124$  is the number of particles in a single layer. We plot this expression along with our simulation results in Fig. 4.8. Although the dependence on  $\mu$  and the layer number can not be confirmed by our data, we see that for low  $\mu$  our simulation results agree roughly with the theoretical prediction. In Fig. 4.8 we also show the number of hcp stacked layers,  $N_{\text{hcp}}$  along with the total number of crystalline layers  $N_{\text{total}}$  and the ratio of the  $N_{\text{hcp}}$  over the number of crystalline for which the stacking can be defined  $N_{\text{total}} - 2$ . Similarly as described above, the average number of layers that are hcp stacked can be calculated using the bulk free energy:

$$\langle N_{\text{hcp}} \rangle = \frac{\sum_{\{s_n\}} \sum_n s_n \exp(+\beta \sum_n s_n \Delta F_n)}{\sum_{\{s_n\}} \exp(+\beta \sum_n s_n \Delta F_n)}, \quad (4.14)$$

where  $n$  denotes the  $n$ th layer,  $s_n$  denotes the stacking of layer  $n$ :  $s_n = 1$  if the layer is hcp stacked,  $s_n = 0$  if the layers is fcc stacked,  $\{s_n\}$  is a particular stacking configuration, such that the sum over  $\{s_n\}$  is over all possible stacking configurations and finally  $\Delta F_n = N_l \Delta f(\mu - mgz_n)$ . This sum can be calculated explicitly because the number of layers is not very large. Furthermore, we can approximate  $\Delta F_n = N_l \bar{\Delta f}$ , where  $\bar{\Delta f}$  is an average free energy difference. In this case the average number of layers is simply equal to  $N_{\text{total}} P_{\text{hcp}}$ . If we set  $\bar{\Delta f} \simeq 0.014$ , we obtain  $\langle N_{\text{hcp}} \rangle / N_{\text{total}} \simeq 0.85$ . From the inset of Fig. 4.8, we see that the full expression and the approximation of 0.85 both overestimate the actual number of layers, except at low chemical potential. We attribute this discrepancy to the statistical noise, which tends to randomize the stacking i.e. bring the stacking probability closer to 0.5.

In ref. [81] it was shown that weakly charged colloidal spheres in a sediment show a much larger fraction of fcc layers than one would expect on the basis of the bulk free energies of such particles [82]. It was reasoned that this mismatch must be related to the gravitational field. To make sure that the difference between the probability of occurrence of hcp and fcc in our simulations is not caused by gravity, we revisited the simulations of hard spheres in gravity of Chap. 2. We measured  $N_{\text{hcp}}/(N_{\text{fcc}} + N_{\text{hcp}})$  using the same method as described in this chapter. Our simulations on hard spheres show that the probability to observe an fcc layer equals the probability to observe an hcp layer within the error bars. The free energy difference for hard spheres is of the order  $10^{-3}k_B T$  per particle, and the sign of the free energy difference is such that fcc is favored. The probability to find an fcc layer is given by  $1/(1 + \exp(\beta N_l \Delta f)) \simeq 0.6$ . Since our error bars are larger than 0.1 our simulations are in agreement with the theoretical estimate. Hence, we do not expect that the deviation of the stacking probability from one half for the dumbbells

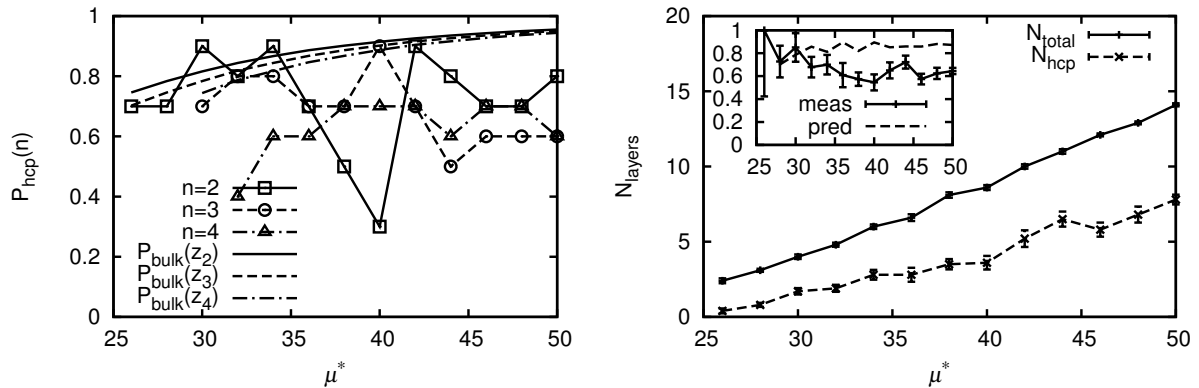


**Figure 4.8:** Left: Probability to find an hcp layer as measured (symbols) using  $\psi_3(z_n)$ , and as calculated from the bulk probability  $P_{\text{bulk}}(z_n)$ . Right: number of hcp layers and total number of crystalline layers; inset:  $N_{\text{hcp}}/(N_{\text{fcc}} + N_{\text{hcp}})$  as measured and as predicted by Eq. (4.14). The stacking of the top and bottom layer is undefined, so  $N_{\text{fcc}} + N_{\text{hcp}} = N_{\text{total}} - 2$ .

is not caused by the gravitational field as reasoned in ref. [81] for spherical colloids, but by the bulk free energy difference for dumbbells.

## 4.5 Summary and discussion

We investigated the structure of a fluid of hard dumbbells in gravity for a gravitational length,  $\ell = \sigma/2$ . We observed pronounced layering of the dumbbells for short elongations, while for long dumbbells layering of the individual spheres of the dumbbells was found, and a more complex center-of-mass density profile. For long dumbbells, we showed that the first peak in this profile corresponds to particles lying flat against the wall, the next to particles standing upright, etc. Furthermore, we measured the density profile and the hexagonal order parameter profiles of crystalline sediments. At  $L = 0.3\sigma$ , we observed a three-phase coexistence with an aligned crystal phase (CP1) at the bottom of the sample, the orientationally disordered plastic crystal in the middle and the fluid on top. For longer dumbbells ( $L = 0.6\sigma$ ) the plastic crystal phase disappears, and we find a direct fluid–CP1 coexistence. For very long dumbbells ( $L = 0.92\sigma$ ) the aperiodic crystal phase appears in between the CP1 phase and the fluid. The density profiles of these crystalline layers are sharply peaked, except for the plastic crystal phases, where the peaks are broadened due to fluctuations of the centers of mass of the dumbbells.

Next, we studied the phase behavior of hard dumbbells in gravity as a function of chemical potential, again for a gravitational length  $\ell = \sigma/2$ . We measured the hexagonal order parameters and order parameters that measured the degree of alignment of the dumbbells at the  $n$ th maximum of the density profile i.e. in the middle of a layer. It was shown that the initial crystallization of all crystal phases appears to be discontinuous, while the following layer-by-layer crystal growth is continuous. An exception occurs for the CP1 crystal, where the crystal growth appears to be discontinuous as well. Using a handwaving argument, one can explain these results using the structure of the fluid layer,

which lies directly on top of the crystal. This fluid layer has some degree of hexagonal ordering, which can be appreciated from the nonzero value of the  $\psi_6(z)$  profiles in Fig. 4.4. The same structuring is also observed for hard spheres and is caused by the top crystalline layer, that serves as a template. However, there is little directional alignment of the fluid layer. Therefore, in order to form a CP1 layer on top of a already formed crystal the rotational symmetry of the direction vectors must be broken, while for the plastic crystal and the aperiodic crystal phase the hexagonally structured fluid can smoothly transform in a crystal. Typically, a transition that breaks a symmetry is discontinuous, which might explain the discontinuous growth of the CP1 crystal. In the initial crystallization the translational symmetry is broken, since the fluid is not hexagonally ordered, and therefore we might expect this transition to be discontinuous. As a word of caution, we note that the same reasoning can be applied to a 2D hard disc solid, while that particular system has a second order (or very weakly first order) freezing transition [83, 84].

The bottom two layers usually crystallized at the same chemical potential, with the exception of the CP1 phase at  $L = 0.6\sigma$  and  $L = 0.92\sigma$ , where only one layer undergoes the phase transition at once. However, for large  $L$  a single layer of CP1 can be identified with two layers of spheres. In conclusion, the same number of layers of spheres crystallize initially for dumbbells as was the case for hard spheres at the same gravitational strength  $g^* = \sigma/\ell = 2$  in Chap. 2.

The lowest chemical potential at which a crystal was found, was compared to the chemical potentials at the bulk coexistences. These chemical potentials corresponded quite well, with the exception of the CP1–PC coexistence at  $L = 0.3\sigma$ . The CP1 phase is stable at a much lower chemical potential than is to be expected from the bulk phase behavior. There are two possible reasons for this discrepancy: Our system has not thermalized yet, although we ran very long simulations to check this. Another explanation is that the plastic crystal phase is frustrated by the CP1 phase that acts as a template and imposes a lattice constant on the plastic crystal which differs from the lattice constant at the same pressure in the bulk. We observed that the bottom layer of the plastic crystal has a lattice constant which differs from the lattice constant of the rest of the layers, which probably gives an additional free energy penalty.

We measured the number of layers of a certain crystal that were formed as a function of chemical potential. The number of layers are mostly described quite well by an expression that has been shown to work for all gravitational lengths in a system of hard spheres in Chap. 2. The exception, again, is the CP1 phase, which has more layers than expected from the bulk chemical potential, presumably for the same reason the chemical potential at which the PC–CP1 transition occurs, was too low. For the other phases, we expect that our expression can be directly applied to other gravitational field strengths. To enable the comparison with (future) experiments, we also gave an expression for the crystallization of layers  $n$  in terms of the local pressure.

Finally, we studied the type of lattice (hcp of fcc) of the plastic crystal. We showed using direct simulations that hcp is favored, which was already shown in the bulk in Chap. 3. We checked that this was not caused by gravity, which has been proposed as a reason for the increased fcc stacking of crystals of weakly charged colloids [81] compared to the bulk crystal [80]. To this end, we measured the stacking probability of hard sphere crystals in gravity, which showed the expected randomly stacked crystal.

---

## Phase behavior and structure of a new colloidal model system of bowl-shaped particles

---

We study the phase behavior of bowl-shaped particles using confocal microscopy and computer simulations. Experimentally, we find the formation of a worm-like fluid phase in which the bowl-shaped particles have a strong tendency to stack on top of each other. However, using free energy calculations in computer simulations, we show that the worm-like phase is out-of-equilibrium and that the columnar phase is thermodynamically stable for sufficiently deep bowls and high densities. In addition, we employ a novel technique based on simulated annealing to predict the crystal structures for shallow bowls. We find four exotic new crystal structures and we determine their region of stability using free energy calculations. We discuss the implications of our results for the development of materials with ferroelectric order.

## 5.1 Introduction

The concept of a mesogenic particle in the form of a bowl is relatively old in the molecular liquid crystal community. Such molecules are expected to form a columnar phase, which can be ferroelectric, i.e., a phase with a net electric dipole moment, when the particles possess a permanent dipole moment. Ferroelectric phases have potential applications for optical and electronic devices. In fact, crystalline (as opposed to liquid crystalline) ferroelectrics are already applied in sensors, electromechanical devices and non-volatile memory [85]. A columnar ferroelectric phase may have the advantage over a crystal, that grain boundaries and other defects anneal out faster due to the partially fluid nature of the columnar phase. In reality, columnar phases of conventional disc-like particles often exhibit many defects, as flat thin discs can diffuse out of a column and columns can split up. The presence of these defects limits their potential use for industrial applications [86]. Less defects are expected in a columnar phase of bowl-shaped mesogens, where particles are supposed to be more confined in the lateral directions. A whole variety of bowl-like molecules have already been synthesized and investigated experimentally [87–90]. However, the number of theoretical studies is very limited as it is difficult to model the complicated particle shape in theory and simulations. In a recent simulation study, the attractive-repulsive Gay-Berne potential generalized to bowl-shaped particles has been used to investigate the stacking of bowl-like mesogens as a function of temperature [86]. The authors reported a nematic phase and a columnar phase. This columnar phase did not exhibit overall ferroelectric order, although polar regions were found.

Recently, a procedure has been developed to synthesize bowl-shaped colloidal particles [91]. This method starts with the preparation of highly uniform silicone oil-in-water emulsion droplets by hydrolysis and polymerization of dimethyldiethoxysilane. Subsequently, the silicone oil droplets were used as templates around which a solid shell with tunable thickness is grown by using tetraethoxysilane. In the next step of the synthesis, the silicone oil in the droplets is dissolved in ethanol and finally, during drying in air, the shells collapse into hemispherical double-walled bowls (Fig. 5.1a). The final shape of the bowls is determined by a trade-off between bending and stretching elastic energy [92]. Axially symmetric bowls are found if the ratio of shell thickness to particle radius is between 0.05 and 0.25 [91, 92]. We also note that recently hemispherical particles were synthesized at an air-solution interface [93] and on a substrate [94]. These hemispherical particles are intended to be used as microlense arrays, but they can also serve as a new type of shape-anisotropic colloidal particle.

In our simulations, we model the particles as the solid of revolution of a crescent (see Fig. 5.1b). The diameter  $\sigma$  of the particle and the thickness  $D$  are defined as indicated in Fig. 5.1b. We define the shape parameter of the bowls by a reduced thickness  $D/\sigma$ , such that the model reduces to infinitely thin hemispherical surfaces for  $D/\sigma = 0$  and to solid hemispheres for  $D/\sigma = 0.5$ . The advantages of this simple model is that it interpolates continuously between an infinitely thin bowl and a hemispherical solid particle (the two colloidal model systems, which we discussed above), and that we can derive an algorithm that tests for overlaps between pairs of bowls, which is a prerequisite for Monte Carlo simulations of hard-core systems.

In this chapter, we study whether columnar liquid crystalline phases with directional

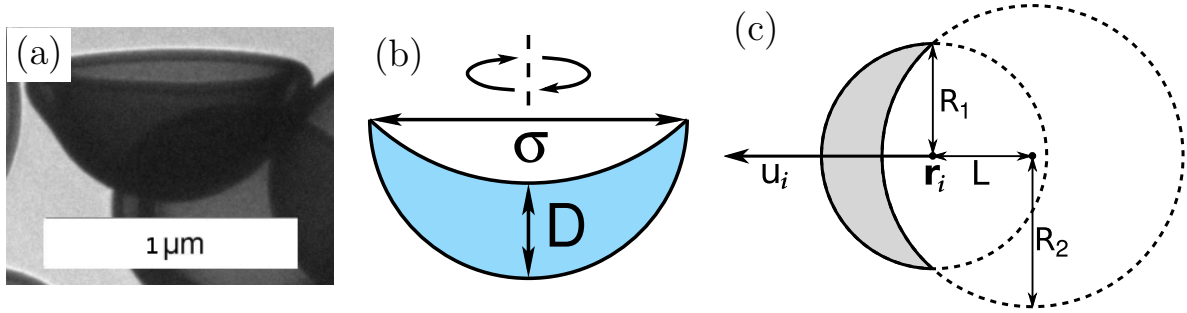


**Figure 5.1:** (a) Transmission electron micrograph of a bowl-shaped colloid. (b) The theoretical model of the colloidal bowl is the solid of revolution of a crescent around the axis indicated by the dashed line. The thickness of the double-walled bowl is denoted by  $D$  and the diameter of the bowl by  $\sigma$ . (c) The shells are defined using two spheres of radii  $R_1$  and  $R_2$ , that are a distance of  $L$  apart. The direction vector,  $\mathbf{u}_i$  and the reference point of the particle,  $\mathbf{r}_i$ , (the dot in the center of the smaller sphere) are indicated.

alignment (polar order) can be driven by entropy alone without any attractive interactions. To this end, we investigate experimentally the stacking and phase behavior of a new colloidal model system of purely repulsive bowl-like particles using confocal microscopy. We complement our study with computer simulations of hard bowls, which allows us to investigate the effect of particle shape on the equilibrium phase behavior of bowl-like particles. First we describe the experiments on which this chapter is based. Subsequently, we elaborate on the model for the collapsed shells; the overlap algorithm is left for the appendix. Also, the (free energy) methods are explained. In the results section, we look at the properties of the isotropic phase. We will investigate the existence and the nature of the transition between the homogeneous fluid phase and the fluid phase that contains the worm-like stacks. Furthermore, we show the packing diagram and the phase diagram with a tentative homogeneous-to-worm-like fluid transition line. In the last section we summarize and discuss the results.

## 5.2 Experiment

Our experimental system consists of hemispherical collapsed shells, which were obtained following the procedure described in Ref. [91]. The only modification was that the dye, rhodamine B-isothiocyanate (RITC), was incorporated in the shell during the coating step. To obtain stable dispersions in the presence of this dye, we used 1% DMDDES and 10%  $\text{NH}_3$  by volume. The radius of the uncoated droplets as determined from static light scattering (SLS) experiments is 520 nm. The thickness of the shell was determined by fitting the SLS data of the coated emulsion droplets with the full Mie solution for the scattering factor of core-shell particles with the core radius kept fixed at 520 nm. The result for the shell thickness was 80 nm. The colloids were dispersed in an index-matched mixture of dimethylsulfoxide (DMSO) and ethanol. A bottomless vial was glued to a cover slip and filled with the suspension and the bowls were allowed to sediment. The gravitational length was estimated to be  $L/\sigma = k_B T / m_B g \sigma \simeq 4$  with  $k_B$  Boltzmann's constant,  $g$  the gravitational acceleration,  $T$  the temperature, and  $m_B$  the buoyant mass of the bowls.

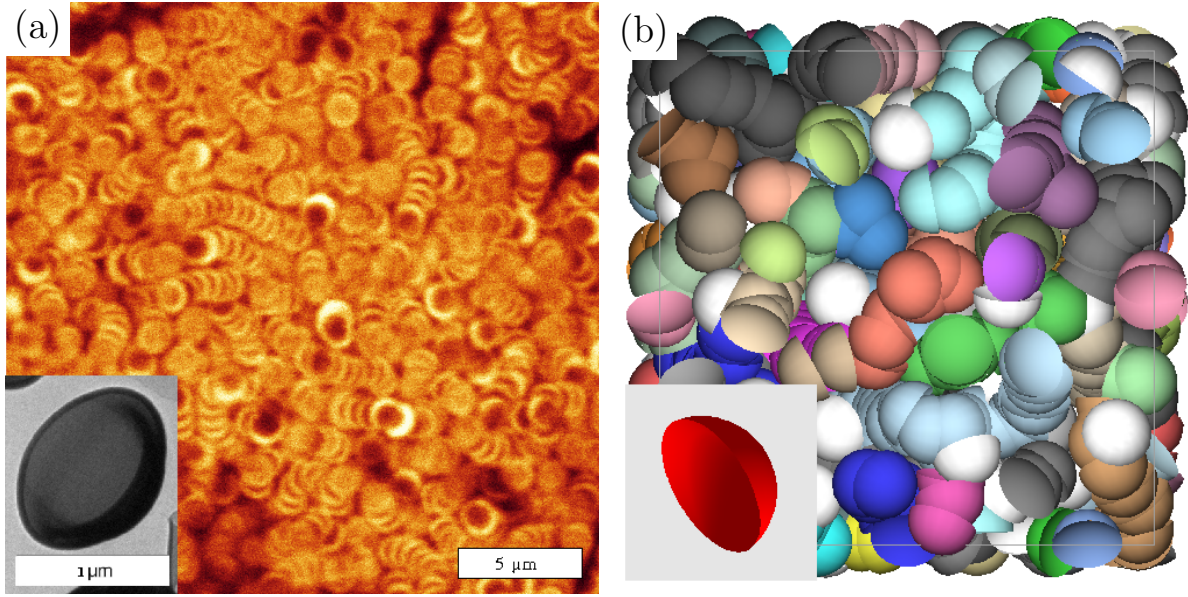


**Figure 5.2:** Confocal microscope image of the bottom layer of the colloidal bowls after 65 days of sedimentation (a). The final configurations obtained from simulations at  $P\sigma^3/k_B T = 50$  and  $D = 0.3\sigma$  (b). The gray values denote different stacks.

Confocal microscopy images of the sediment were recorded at regular intervals with a Leica SP2 and excitation wavelength of 532 nm. The sediment continued to compact for several weeks, while the particles formed stacks. A typical image is shown in Fig. 5.2a taken after 51 days of sedimentation. We clearly observe that the bowls form stacks as can be recognized by the “C” shapes that are stacked on top of each other. These stacks are present throughout the whole sample and can have lengths up to 15 particles running in random directions. We also note that many stacks are bent and bifurcated by forming Y-shaped junctions. The dynamics of the bowls has been slowed down dramatically as the density at the bottom of the sample had increased significantly due to sedimentation. The bowl-shaped particles seem to get caged by the neighboring particles, which may have prevented them from finding a more ordered thermodynamically equilibrium phase. Even after 234 days the structure had not changed noticeably compared to the structure as observed after 51 days of sedimentation.

## 5.3 Simulation methods

### 5.3.1 Model

Now we describe the model that we use to represent the collapsed shells or bowls in more detail. Consider a sphere with a radius  $R_1$  at the origin and a second sphere with radius  $R_2 > R_1$  at position  $-L\mathbf{u}_i$ , where  $\mathbf{u}_i$  is the unit vector denoting the orientation of the bowl and  $L > 0$ . The bowl is represented by that part of the sphere with radius  $R_1$  that has no overlap with the larger sphere, see Fig. 5.1b. We have chosen the values for  $L$  and  $R_2$  such that the bowls are hemispherical and resemble the experimental model system.

We define the thickness of the bowls by  $D = L - (R_2 - R_1)$ , such that the model reduces to the surface of a hemisphere for  $D = 0$  and to a solid hemisphere for  $D = R_1$ . The volume of the particle is  $\frac{\pi}{4} D (\sigma^2 - D\sigma + \frac{2}{3}D^2)$ , where  $\sigma \equiv 2R_1$  is our unit of length. The algorithm to determine overlap between our bowls is described in the appendix.

### 5.3.2 Fluid phase

We employ standard *NPT* MC simulations to obtain the equation of state (EOS) for the fluid phase. In addition, we obtain the compressibility by measuring the fluctuations in the volume:

$$\frac{\langle V^2 \rangle - \langle V \rangle^2}{\langle V \rangle} = \frac{k_B T}{\rho} \frac{\partial \rho}{\partial P}, \quad (5.1)$$

where  $\rho = N/V$  is the number density. We determine the free energy at density  $\rho_1$  by integrating the EOS from reference density  $\rho_0$  to  $\rho_1$ :

$$\frac{F(\rho_1)}{N} = \mu(\rho_0) - \frac{P(\rho_0)}{\rho_0} + \int_{\rho_0}^{\rho_1} \frac{P(\rho)}{\rho^2} d\rho \quad (5.2)$$

where the chemical potential  $\mu(\rho_0)$  is determined using the Widom particle insertion method [79], and  $P(\rho_0)$  is determined by a local fit to the EOS.

To investigate the structure of the fluid phase, we measure the positional correlation function [95],

$$g_c(z) = \frac{1}{N\rho A_{\text{col}}} \left\langle \sum_{i=1}^N \sum_{j=1}^{N_{\text{col}}(i)} \delta(\mathbf{r}_{ij} \cdot \mathbf{u}_i - z) \right\rangle, \quad (5.3)$$

where the sum over  $j$  runs over  $N_{\text{col}}(i)$  particles in a column of radius  $\sigma/2$  with orientation  $\mathbf{u}_i$  centered around particle  $i$ , and where the area of the column is denoted by  $A_{\text{col}} = \pi\sigma^2/4$ . At sufficiently high pressure the particles stack on top of each other to form disordered worm-like piles which resemble the stacks observed in the experiments. As the stacks have a strong tendency to buckle, we cannot use  $g_c(z)$  to determine the length of the stacks. We therefore determine the stack size distribution using a cluster criterion. Particle  $i$  and  $j$  belong to the same cluster if

$$\begin{aligned} |\mathbf{r}_{ij} + (\zeta D/2 + \sigma/4)(\mathbf{u}_j - \mathbf{u}_i)| &< \sigma/2 \quad \text{and} \\ \mathbf{u}_i \cdot \mathbf{u}_j &> 0, \end{aligned} \quad (5.4)$$

and where the first condition has to be satisfied for  $\zeta = -1, 0$  or  $1$  and  $\mathbf{r}_{ij} = \mathbf{r}_j - \mathbf{r}_i$ , with  $\mathbf{r}_i$  denoting the center of the sphere with radius  $R_1$  of particle  $i$ , see Fig. 5.1b. If both conditions are satisfied, particle  $j$  is just above ( $\zeta = 1$ ) or below ( $\zeta = -1$ ) particle  $i$  in the stack, or, when the stack is curved, particle  $j$  can be next to particle  $i$  ( $\zeta = 0$ ). We now define the cluster distribution as the fraction of particles that belongs to a cluster of size  $n$ :  $\mathcal{P}_{\text{stack}}(n) \equiv nN_n/N$ , where  $N_n$  is the number of clusters of size  $n$ . We checked that the cluster size distribution does not depend sensitively to the choice of parameters in Eq. (5.4).

### 5.3.3 Columnar phases

We also perform *NPT* simulations of the columnar phase using a rectangular simulation box with varying box lengths in order to relax the inter-particle distance in  $z$  direction, along the columns, independently from the lattice constant in the horizontal direction. The difference between the free energy of the columnar phase at a certain density and the free energy of the fluid phase at a lower density is determined using a thermodynamic integration technique [96]. We apply a potential which couples a particle to its column:

$$\Phi_{\text{hex}}(\mathbf{r}^N, \lambda) = \lambda \sum_{i=1}^N \cos(2\pi N_x x_i / L_x) \sin(\pi N_y y_i / L_y), \quad (5.5)$$

where  $x_i$  and  $y_i$  are the  $x$  and  $y$  components respectively of  $\mathbf{r}_i$ ,  $N_\alpha$  is the number of columns in the  $\alpha$  direction and  $L_\alpha$  is the size of the box in the  $\alpha$  direction. In our simulations, we calculate Eq. (5.5) while fixing the center of mass. We calculate all four combinations

$$\sum_{i=1}^N \text{trig1}(2\pi N_x x_i / L_x) \text{trig2}(\pi N_y y_i / L_y) \quad (5.6)$$

for  $\text{trig1} = \cos, \sin$  and  $\text{trig2} = \cos, \sin$ , although we are only interested in  $\varphi_{\text{hex}}(\mathbf{r}_i)$ , that is Eq. 5.6 with  $\text{trig1} = \cos$ , and  $\text{trig2} = \sin$ . By using some basic trigonometry one can express the change in these four expressions upon displacement of a single particle in terms of single particle properties and the previous values of the expressions. As a result, we do not have to perform the full summation over all particles in Eq. (5.6) every time we displace a particle. Unfortunately, this calculation requires the evaluation of many more trigonometric functions than the simple expression (5.5), but the extra computation time is negligible compared to the overlap check. In addition to this positional potential, we also constrain the direction of the particle, using the potential

$$\Phi_{\text{ang}}(\mathbf{u}^N, \lambda) = \lambda' \sum_{i=1}^N u_{i,z}, \quad (5.7)$$

where we used  $\lambda' = 0.1\lambda$ . The thermodynamic integration path from the columnar phase to the fluid is as follows: We start from the columnar phase at a certain density  $\rho_2$ . Subsequently, we slowly turn on the two potentials, i.e. we increase  $\lambda$  from 0 to  $\lambda_{\text{max}}$ . Next, we integrate the equation of state to go from  $\rho_2$  to  $\rho_1$ , while keeping  $\lambda = \lambda_{\text{max}}$  fixed. During this step the columnar phase will only be stable below the coexistence density, if  $\lambda_{\text{max}}$  is high, although  $\lambda_{\text{max}} = 20k_B T$  proved to be sufficient. Finally, fixing the density  $\rho_1$ , we gradually turn off the potentials, while integrating over  $\lambda$  from  $\lambda_{\text{max}}$  to 0. During this last step, the columnar phase melts continuously, provided that the density  $\rho_1$  is low enough and that  $\lambda$  is high enough to prevent melting during the density integration step. The resulting free energy difference between the columnar phase and fluid phase is given by

$$F_{\text{col}}(\rho_2) - F_{\text{fluid}}(\rho_1) = \int_0^{\lambda_{\text{max}}} \left\langle \Phi_{\text{hex}}(\mathbf{r}^N, \lambda) / \lambda + \Phi_{\text{ang}}(\mathbf{u}^N, \lambda) / \lambda \right\rangle \Big|_{\rho=\rho_1} + \int_{\rho_1}^{\rho_2} d\rho \frac{NP(\rho)}{\rho^2} \Big|_{\lambda=\lambda_{\text{max}}} - \int_0^{\lambda_{\text{max}}} \left\langle \Phi_{\text{hex}}(\mathbf{r}^N, \lambda) / \lambda + \Phi_{\text{ang}}(\mathbf{u}^N, \lambda) / \lambda \right\rangle \Big|_{\rho=\rho_2} \quad (5.8)$$

Positional potential (5.5) is designed to stabilize a hexagonal array of columns, but, strictly speaking, it does not have the hexagonal symmetry of the columnar phase, since it is not invariant under a 60 degrees rotation of the whole system around a lattice position. However, we have found that replacing Eq. 5.5 by a positional potential that does have this symmetry, does not have a significant effect on the free energy difference.

A second type of columnar phase can be constructed by flipping half of the bowls. In this way we obtain alternating vertical sheets (i.e. rows of columns) of bowls that point upwards and sheets of bowls that point downwards, we will refer to this phase as the inverted columnar phase. We calculate the free energy of this phase using the method described above, with the modification that the angular potential now reads,

$$\Phi_{\text{ang}}(\mathbf{u}^N, \lambda) = \lambda' \sum_i u_{i,z}^2. \quad (5.9)$$

This potential could also have been used for the non-inverted columnar phase, and we have found that the result of the free energy integration for the columnar phase is the same whether we use Eq. (5.9) or Eq. (5.7).

### 5.3.4 Crystals

#### Packing

As the crystal phases of the bowls are not known a priori, we developed a novel pressure annealing method to obtain the possible crystal phases [97], which we named after the common used thermal annealing technique. Fully variable box shape  $NPT$  simulations were performed on system of only 2-6 particles. By construction, the final configuration of such a simulation is a crystal, where the unit cell is the simulation box. One cycle of such a simulation consists of the following steps: We start at a pressure of  $10k_B T/\sigma^3$ . Subsequently, we run a series of simulations, where the pressure increases by a factor of ten each run:  $P\sigma^3/k_B T = 10, 100, \dots, 10^6$ . At the highest pressure ( $10^6 k_B T/\sigma^3$ ) we measure the density and angular order parameters,  $S_1 \equiv \|\langle \mathbf{u}_i \rangle\|$  and  $S_2 \equiv \lambda_2$ , where  $\lambda_2$  is the highest eigenvalue of the matrix whose components are  $Q_{\alpha\beta} = \frac{3}{2} \langle u_{i\alpha} u_{i\beta} \rangle - \frac{1}{2} \delta_{\alpha\beta}$ , where  $\alpha, \beta = x, y, z$ . We store the density if it is the highest density found so far for these values of  $S_1$  and  $S_2$ . We ran 1000 of such cycles for each aspect ratio, which is enough to visit each crystal phase multiple times. After completing the simulations, we tried to determine the lattice parameters of the resulting crystal by hand. Although this last step is not necessary, it is convenient to have analytical expressions for the lattice vectors and the density at hand. The pressure annealing runs were performed at  $D/\sigma = 0.1, 0.15, \dots, 0.5$ . For many of the crystals, we were not able to find analytical expressions for the lattice parameters. For these crystals, we obtain the densities of the close packed crystals for intermittent values of  $L$  by averaging the density in single simulation runs at a pressure of  $10^6 k_B T/\sigma^3$ . The initial configurations for the value of  $L$  of interest were obtained from the final configurations of the pressure annealing simulations for another value of  $L$  by one of the following two methods, depending on whether we needed to decrease or increase  $L$ : When decreasing  $L$  no overlaps are created so the final configuration of the simulation for the previous value of  $L$  can be used as initial configuration. On the other hand, increasing  $L$  results in an overlap, which is removed by scaling the system uniformly. Subsequently,

the pressure is stepwise increased from  $1000k_B T/\sigma^3$  to  $10^6 k_B T/\sigma^3$ , by multiplying by 10 each step.

### Free energies

We calculate the free energy of the various crystal phases by thermodynamic integration using the Einstein crystal as a reference state [9]. The Einstein integration scheme that we employ here is similar to the one, that was used to calculate the free energies of crystals of dumbbells in Chap. 3. We briefly sketch the integration scheme here and discuss the modifications that we applied. We couple both the positions and the direction of the particles with a coupling strength  $\lambda$ , such that for  $\lambda \rightarrow \infty$ , the particles are in a perfect crystalline configuration. First, we integrate  $\partial F/\partial \lambda$  over  $\lambda$  from zero to a large but finite value for  $\lambda$ . Subsequently we replace the hard core particle–particle interaction potential by a soft interaction, where we can tune the softness of the potential by the interaction strength  $\gamma$ . We integrate over  $\partial F/\partial \gamma$  from a system with essentially hard core interaction (high  $\gamma = \gamma_{\max}$ ), to an ideal Einstein crystal ( $\gamma = 0$ ). Some minor alterations to the scheme of Chap. 3 were introduced, which were necessary, because of the different shape of the particle. For the coupling of the orientation of bowl  $i$ , i.e.,  $\mathbf{u}_i$ , to an aligning field, we have to take into account that the bowls have no up down symmetry, while the dumbbells are symmetric under  $\mathbf{u}_i \rightarrow -\mathbf{u}_i$ . The potential energy function that achieves the usual harmonic coupling of the particles to their lattice positions, as well as the new angular coupling, reads:

$$\beta U(\mathbf{r}^N, \mathbf{u}^N; \lambda) = \lambda \sum_{i=1}^N (\mathbf{r}_i - \mathbf{r}_{0,i})^2 / \sigma^2 + \sum_{i=1}^N \lambda (1 - \cos(\theta_{i0})), \quad (5.10)$$

where  $\mathbf{r}_i$  and  $\mathbf{u}_i$  denote, respectively, the center-of-mass position and orientation of bowl  $i$  and  $\mathbf{r}_{0,i}$  the lattice site of particle  $i$ ,  $\theta_{i0}$  is the angle between  $\mathbf{u}_i$  and the ideal tilt vector of particle  $i$ , and  $\beta = 1/k_B T$ . The Helmholtz free energy (Eq. (3.15)) of the noninteracting Einstein crystal is modified accordingly, but the only modification is the integral over the angular coordinates:

$$J(\lambda) = \int_{-1}^1 e^{\lambda(x-1)} dx = \frac{1 - e^{-2\lambda}}{\lambda}. \quad (5.11)$$

Although the shape of the bowls is more complex than the dumbbell, we can still use a rather simple form for the pairwise soft potential interaction:

$$\beta U_{\text{soft}}(\mathbf{r}^N, \mathbf{u}^N; \gamma) = \sum_{i < j} \beta \varphi(\mathbf{r}_i - \mathbf{r}_j, \mathbf{u}_i, \mathbf{u}_j, \gamma) \quad (5.12)$$

with

$$\beta \varphi(\mathbf{r}_j - \mathbf{r}_i, \mathbf{u}_i, \mathbf{u}_j, \gamma) = \begin{cases} \gamma(1 - A(r'_{ij}/\sigma_{\max})^2) & \text{if } i \text{ and } j \text{ overlap} \\ 0 & \text{otherwise} \end{cases}, \quad (5.13)$$

where  $r'_{ij} \equiv |\mathbf{r}_j - \mathbf{r}_i + \frac{\sigma-D}{2}(\mathbf{u}_i - \mathbf{u}_j)|$  i.e. the distance between the “centers” of bowl  $i$  and bowl  $j$ ,  $\sigma_{\max}$  is the maximal  $r'_{ij}$  for which the particles overlap:  $\sigma_{\max}^2 = \sigma^2 + (\sigma - D)^2$ ,  $A$  is an adjustable parameter that is kept fixed during the simulation at a value  $A = 0.5$ ,

and  $\gamma$  is the integration parameter. It was shown in Ref. [62] that in order to minimize the error and maximize the efficiency of the free energy calculation, the potential must decrease as a function of  $r$  and must exhibit a discontinuity at  $r$  such that both the amount of overlap and the number of overlaps decrease upon increasing  $\gamma$ . Here, we have chosen this particular form of the potential because it can be evaluated very efficiently in a simulation, although it does not describe the amount of overlap between bowls  $i$  and  $j$  very accurately. We checked that adding a term that tries to describe the angular behavior of the amount of overlap does not significantly change our results of the free energy calculations. Also, we checked that by employing the usual Einstein integration method (i.e. only hard core interactions) at a relatively low density we obtained the same result as by using the method of Fortini *et al.*[62]. As the final modification, we increase the maximum interaction strength  $\gamma_{\max}$  to 200.

We perform variable box shape NPT simulations [65] to obtain the equation of state for varying  $D$ . In these simulations not only the edge length changes, but also the angles between the edges are allowed to change. We employ the averaged configurations in the Einstein crystal thermodynamic integration. We calculate the free energy as a function of density by integrating the EOS from a reference density to the density of interest:

$$F(\rho_1^*) = F(\rho_0) + \int_{\rho_0}^{\rho_1} d\rho \left\langle \frac{NP(\rho)}{\rho^2} \right\rangle \quad (5.14)$$

## 5.4 Results

### 5.4.1 Stacks

We compare the experimental results from Sec. 5.2 with computer simulations. We perform standard Monte Carlo simulations in the isobaric-isothermal ensemble (NPT). Fig. 5.2b shows a typical configuration of bowl-shaped particles with  $D = 0.3 \sigma$  at  $P\sigma^3/k_B T = 50$ , displaying similar stacking behavior as observed in the experiments. The equation of state (EOS) of the fluid is somewhat peculiar: the pressure as a function of density is not always convex for all densities, although the compressibility does decrease monotonously with packing fraction  $\phi$  for  $D = 0.1\sigma$ , see Fig. 5.3, where the packing fraction is defined as  $\phi = \frac{\pi D}{4}(\sigma^2 - D\sigma + \frac{2}{3}D^2)N/V$ . This behavior persists for all  $D \leq 0.2\sigma$ , but for  $D \geq 0.25\sigma$  the pressure is always convex. We investigate the origin of these peculiarities using  $g_c(z)$ , the positional correlation function along the director of a particle, which includes only the particles in a column around a particle, as defined in Eq. (5.3). As can be seen from  $g_c(z)$  in Fig. 5.4, the structure of the fluid changes dramatically as the pressure is increased. At  $P^* \equiv \beta P\sigma^3 = 1$ , the correlation function is typical for a low density isotropic fluid of hemispherical particles; no effect of the dent of the particles is found at low densities. The only peculiar feature of  $g_c(z)$  for  $P^* = 1$  is that it is not symmetric around zero, but this is caused by our choice of reference point on the particle (see Fig. 5.1b), which is located below the particle if the particle points upwards. In contrast, at  $P^* = 10$   $g_c(z)$  already shows strong structural correlations. Most noteworthy is the peak at  $z = D$ , that shows that the fluid is forming short stacks of aligned particles. Also, note that the value of  $g_c(z)$  is nonzero around  $z = 0$ . This is

caused by pairs of bowls that align anti-parallel and form a sphere-like object, as depicted in Fig. 5.4. Finally, at  $P^* = 50$  and higher, long worm-like stacks are fully formed and  $g_c(z)$  shows multiple peaks at  $z = Dn$  for both positive and negative integer values of  $n$ .

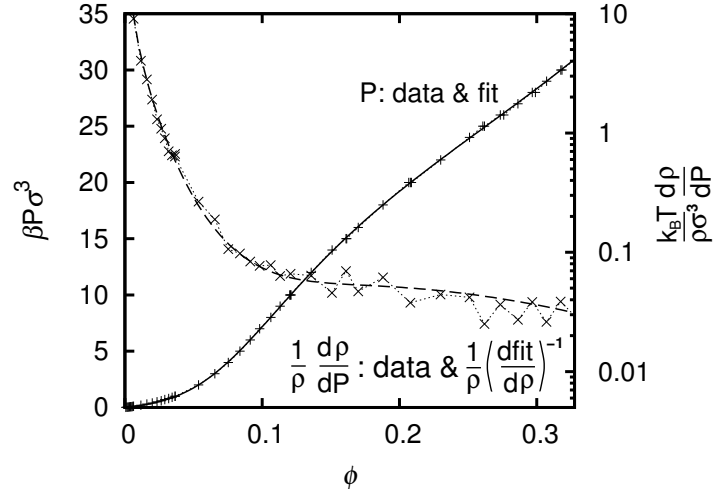


**Figure 5.3:** The equation of state for bowl-shape particles with  $D = 0.1\sigma$ , pressure  $P$  in units of  $k_B T/\sigma^3$  versus packing fraction (left axis), and the reduced compressibility  $\frac{k_B T}{\rho\sigma^3} \frac{\partial \rho}{\partial P}$  on a log scale (right axis). The points are data obtained from  $NPT$  simulations. The solid line is a fit to the pressure; the dashed line is the corresponding reduced compressibility,  $\frac{1}{\rho} \left( \frac{\partial \text{fit}(\rho)}{\partial \rho} \right)^{-1}$ .

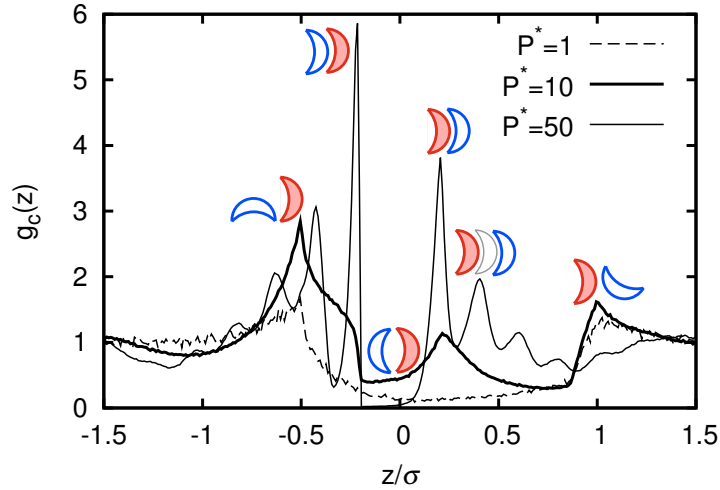


**Figure 5.4:** The pair correlation function,  $g_c(z)$ , of a fluid of bowl-shaped particles with  $D = 0.2\sigma$  as a function of the dimensionless inter-particle distance  $z/\sigma$  along the axis of a reference bowl for various reduced pressures  $P^* \equiv \beta P \sigma^3$ . Only particles within a cylinder of diameter  $\sigma$  around the bowl are considered, as indicated by the subscript ‘c’. We show typical two-particle configurations that contribute to  $g_c(z)$  for  $z/\sigma = -0.5, -0.2, 0.2, 0.4$  and  $1$ , where the filled bowls denote the reference particle, and the open bowls with thick outlines denote the other particle.

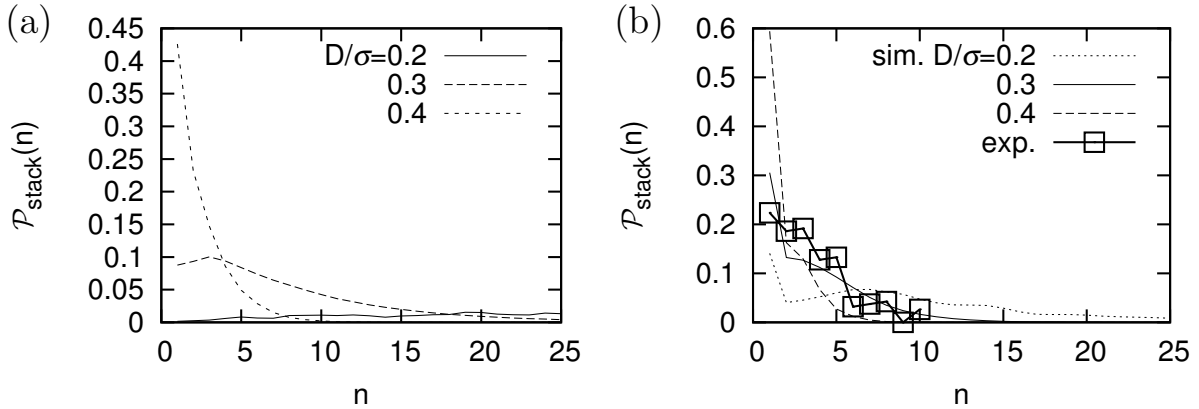


**Figure 5.5:** The probability,  $\mathcal{P}_{\text{stack}}(n)$ , to find a particle in a stack of size  $n$  for  $D/\sigma = 0.2, 0.3$  and  $0.4$  and  $P\sigma^3/k_B T = 50$  (a). Stack distribution for the same state points as in (a), but now in a slab of thickness  $\sigma$  (b).

Furthermore, at these pressures, there are no sphere-like pairs, as can be observed from the value of  $g_c(0)$ . The formation of stacks explains the peculiar behavior of the pressure: At low densities, the bowls rotate freely, which means that the pressure will be dominated by the rotationally averaged excluded volume. The excluded volume of two particles that are not aligned is nonzero, even for  $D = 0$ , and gives rise to the convex pressure which is typical for repulsive particles. As the density increases and the bowls start to form stacks, the available volume increases, and the pressure increases less than expected, which can even cause the pressure to be concave. At even higher densities the worm-like stacks are fully formed, and the pressure is again a convex function for  $D > 0$ , dominated by the excluded volume of locally aligned bowls. The excluded volume of completely aligned infinitely thin bowls is zero, and, therefore, the pressure increases almost linearly with density for  $D = 0$  when the stacks are fully formed.

To quantify the length of the stacks we calculated the stack distribution, both in simulations and in experiments. The cluster distribution of the shells are shown in Fig. 5.5a. As can be seen from the figure, the length of the stacks is strongly dependent on  $D/\sigma$ . However, we have found that above a certain threshold pressure the distribution of stacks is nearly independent of pressure. In the experiments the cluster distribution was determined from a single confocal slice i.e. only shells in a single focal plane were imaged. So in addition to the 3D cluster distribution, we also calculated the cluster distribution of the shells within a slab of thickness  $\sigma$ . Furthermore, a stack seen from above could not be distinguished from a single stack in the experiments. So in the simulations, all bowls with a tilt vector within  $30^\circ$  to the normal of the slab could not be part of a cluster. Instead, for simplicity, they were counted as clusters of size 1, while in the experiments a group of them could be counted as a single particle. For this reason the fraction of particles in a cluster of size 1,  $\mathcal{P}_{\text{stack}}(1)$  can not directly be compared between the experiments and the simulations. Accordingly, the normalization is also slightly affected. The cluster distributions obtained in this fashion are shown in Fig. 5.5b for  $L/\sigma = 0.2\sigma, 0.3\sigma$  and  $0.4\sigma$ , together with the experimental results. From this figure we can conclude that of these values of  $L$ , the cluster distribution for simulated bowls with  $L = 0.3\sigma$  shows the

most similarity to the experimental distribution. Note especially, that, according to both of these distributions, stacks of 8-10 particles occur with an appreciable probability, while larger stacks are nearly never found. We checked that modifying the experimental value of  $\mathcal{P}_{\text{stack}}(1)$  by a factor of two (and adjusting the normalization correspondingly) did not change this conclusion. The thickness of the sediment in the experiment is in the millimeter range, so the gravitational pressure on the bottom layers is very large. Therefore, we can safely assume that the pressure in the experiments exceeds the threshold pressure, that was mentioned above, and that our comparison with the experiments is warranted. In our theoretical model, the distance of closest approach of two bowls is equal to the thickness  $D$  of the bowl-shaped particles. By measuring the inter-particle distance in a short straight stack in the experimental system, we can map the colloidal bowls onto the theoretical model. By equating  $D$  to the measured inter-particle distance, we obtain a reduced thickness  $D/\sigma \simeq 430\text{nm} / 1360\text{nm} \simeq 0.32$ , where we have defined the radius,  $\sigma/2$ , of the double-walled colloids to be the core radius plus two times the shell thickness. This estimate for  $D/\sigma$  is remarkably close to  $D/\sigma = 0.3$  for which we find good agreement for the stack distributions, providing confidence in our theoretical model.

We investigated whether the worm-like stacks could spontaneously reorient to form a columnar phase. We increased the pressure in small steps of  $1 k_B T / \sigma^3$  from well below the fluid-columnar transition to very high pressures, where the system was essentially jammed. At each pressure, we ran the simulation for  $4 \cdot 10^6$  Monte Carlo cycles, where a cycle consists of  $N$  particle and volume moves. These simulations show that the bowls with a thickness  $D \geq 0.25\sigma$  always remained arrested in the worm-like phase, which is similar to the experimental observations. However, for  $D/\sigma = 0.1$  and  $0.2$ , we find that the system eventually transforms into a columnar phase in the simulations (see Fig. 5.6). This might be explained by the fact that the isotropic-to-columnar transition occurs at lower packing fractions for deeper bowls (smaller  $D$ ), which facilitates the rearrangements of the particles into stacks and the alignment of the stacks into the columnar phase. However, using our experimental procedure to synthesize colloidal bowls, it is hard to obtain a thickness  $D \leq 0.2\sigma$ , as theoretical calculations and experiments show that colloidal shells with smaller shell thickness collapse into bowls with wrinkles [92], which makes it harder for them to stack. Preliminary attempts to form ordered phases of the bowl-shaped particles by applying oscillating electric fields (as in Ref. [98]) and sedimentation on a template (as in Ref. [35]) have not been successful. So in the remainder of this chapter, we will study the crystallization of the shells using only simulations.

### 5.4.2 Packing

We found five candidate crystal structures, denoted X, IX, IX', B and IB, using the pressure annealing method. Snapshots of a few unit cells of these crystal phases are shown in Fig. 5.8 along with the fcc<sup>2</sup>, which was not found in the pressure annealing simulations. We will describe these crystal structures using the order parameters  $S_1$ , that measures alignment of the particles, and the nematic order parameter ( $S_2$ ), that is nonzero for both parallel and anti-parallel configurations. Crystal structure X has  $S_1 \simeq 1$  and  $S_2 \simeq 1$ , and

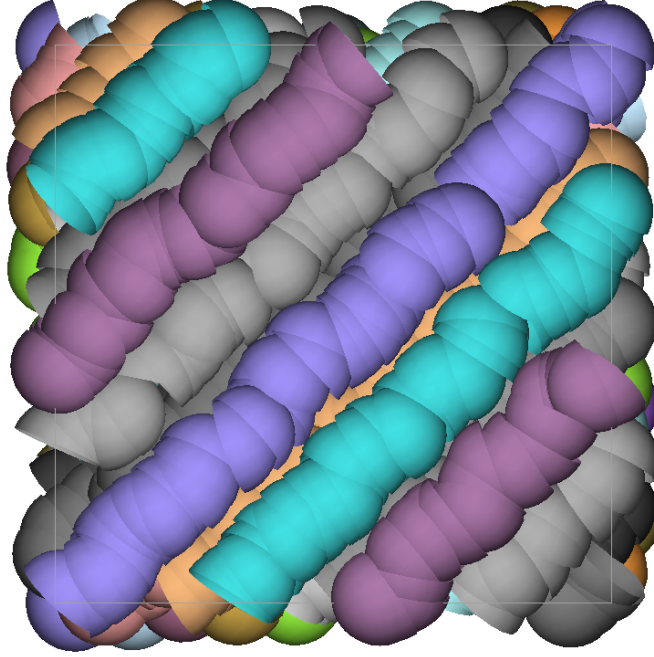


**Figure 5.6:** The final configuration of a simulation of bowls with  $L = 0.1D$  at  $P\sigma^3/k_B T = 38$ . The gray values denote different columns.

the particles are stacked head to toe in columns. The lattice vectors are

$$\begin{aligned} \mathbf{a}_1 &= \sigma \hat{x} & \mathbf{a}_2 &= D \hat{z} \\ \mathbf{a}_3 &= \frac{\sigma}{2} \hat{x} + \frac{1}{2} \sqrt{\sigma^2 - D^2 + 2\sigma \sqrt{\sigma^2 - D^2}} \hat{y} + \frac{D}{2} \hat{z}, \end{aligned} \quad (5.15)$$

and the density is

$$\rho \sigma^3 = \left[ \frac{D\sigma}{2} \sqrt{\sigma^2 - D^2 + 2\sigma \sqrt{\sigma^2 - D^2}} \right]^{-1}. \quad (5.16)$$

The order parameters of the second crystal structure, are  $S_1 \simeq 0$  and  $S_2 \simeq 1$ , which is caused by the fact that one half of the particles point upwards, and the other half downwards. Further investigation shows that there are two phases with  $S_2 \simeq 1$  and  $S_1 \simeq 0$ : one at low  $D$  (IX) and one at  $D \simeq \sigma/2$  (IX'). The structure within the columns of the first (IX) of these two structures is the same as for the X structure, but one half of these columns are upside down, like in the inverted columnar phase (in fact, the IX crystal melts into the inverted columnar phase). The lattice vectors of crystal structure IX are

$$\begin{aligned} \mathbf{a}_1 &= \sigma \hat{x} & \mathbf{a}_2 &= D \hat{z} \\ \mathbf{a}_3 &= \frac{\sigma}{2} \hat{x} + \frac{1}{2} \sqrt{3\sigma^2 - 4D^2} \hat{y}, \end{aligned} \quad (5.17)$$

and the density is

$$\rho \sigma^3 = \left[ \frac{D\sigma}{2} \sqrt{3\sigma^2 - 4D^2} \right]^{-1}. \quad (5.18)$$

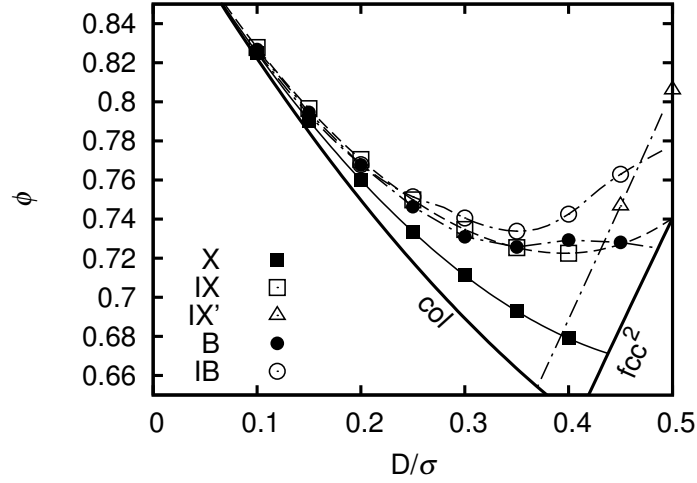


**Figure 5.7:** Packing diagram: maximum packing fraction ( $\phi$ ) of various crystal phases as a function of the thickness ( $D$ ) of the bowls. The points are the results of the pressure annealing simulations. The thin dot-dashed lines are obtained from the pressure annealing results by slowly increasing or decreasing  $L$  as described in Sec. 5.3.4, except for the IX phase (thin dashed line with open squares) and the X phase (thin solid line with filled squares), for which the packing fraction can be expressed analytically. The thick lines denote the packing fractions of the perfect hexagonal columnar phase (col) and the paired fcc phase ( $\text{fcc}^2$ ). Any points that lie below these lines are expected to be thermodynamically unstable (see text).

The columns in the IX crystal are arranged in such a way that the rims of the bowls can interdigitate nicely. The IX' crystal can be obtained from the IX phase at  $D = \sigma/2$  by shifting every other layer by some distance perpendicular to the columns, such that the particles in these layers fit into the gaps in the layers below or above. In this way a higher density than Eq. (5.18) is achieved. The columns of the third crystal phase (B) resemble braids with alternating tilt direction of the particles within each column. Because of this tilt  $S_1$  and  $S_2$  have values between 0 and 1, that depend on  $D$ . Furthermore, the inverted braids structure (IB), that has  $0 < S_2 < 1$  and  $S_1 = 0$ , can be obtained by flipping one half of the columns of the braid-like phase (B) upside down. These braid-like columns piece together in such a way that the particles are nicely interdigitated. In other words, this phase is related to the B phase in exactly the same way as the IX phase is related to the X phase. Finally, in the paired face-centered-cubic ( $\text{fcc}^2$ ) phase, pairs of hemispheres form sphere-like objects that can rotate freely and that are located at the lattice positions of an fcc crystal. The density at close packing is  $2\sqrt{2}/\sigma^3$ , i.e. twice the density of fcc.

In Fig. 5.7 the results of the pressure annealing method are shown, along with the known packing fractions of the perfect hexagonal columnar phase (col) and the paired fcc phase ( $\text{fcc}^2$ ). Since these phases have one-dimensional positional or rotational degrees of freedom, we expect these phases to have a higher entropy (lower free energy) than any crystal phase with the same or lower maximum packing fraction whose degrees of freedom have all been frozen out. Therefore, any crystal structure with a packing fraction below the thick lines in Fig. 5.7 is most likely thermodynamically unstable. We were unable to find the  $\text{fcc}^2$  and the columnar phase using the pressure annealing method as described

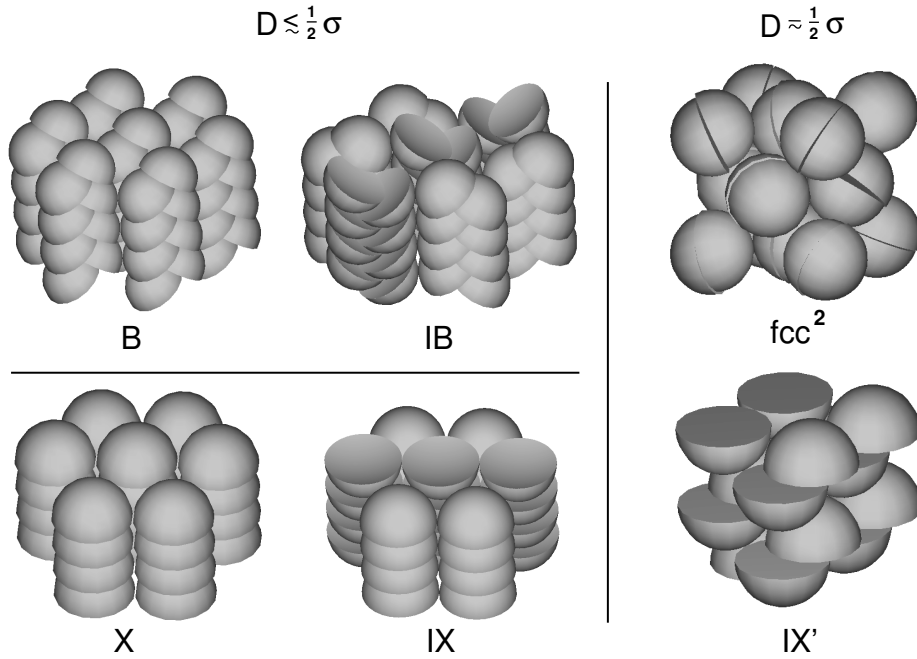


**Figure 5.8:** The various crystal phases that were considered as possible stable structures. Five of these were found using the pressure annealing method: X, IX, B, IB and IX'. X, IX, B and IB are densely packed structures for  $D \lesssim 0.5 \sigma$  and fcc<sup>2</sup> and IX' are densely packed crystal structures for (nearly) hemispherical bowls ( $D \simeq 0.5 \sigma$ ).

in Sec. 5.3.4. The first reason for this is the fact that the columnar and fcc<sup>2</sup> phases are not stable at high pressures. Furthermore, the translational symmetry of the system in the direction of the column decreases the number of degrees of freedom in the columnar phase that are not frozen out to  $N - 1$ , and therefore the entropy decreases as well. However, if we increase the pressure slowly to  $100k_B T / \sigma^3$  in simulations of 12 particles, we did observe the fcc<sup>2</sup> phase for hemispherical particles ( $D = \sigma/2$ ). In these simulations at finite pressure, it is important to constrain the length of all box vectors such that it remains larger than say  $1.5\sigma$ . Otherwise the box will become extremely elongated, such that the particles can interact primarily with their own images. In this way, the system lowers its Gibbs free energy  $G = F + PV$ , because the volume decreases without any decrease in entropy due to restricted translational motion (if a particle moves, its image moves as well, so a particle translation will never cause overlap of the particle with its image). The decrease in Gibbs free energy is of course an extreme finite size effect, which should be avoided if we wish to predict the equilibrium phase behavior. For the pressure annealing simulations at very high pressures, these effects are not important, because the entropy term in the Gibbs free energy is small compared to  $PV$ . We did not attempt to find the columnar phase using the modified pressure annealing method, as we were only interested in finding candidate crystal structures. Furthermore, the columnar phase was already found in more standard simulations with a larger number of particles.

### 5.4.3 Free energies

In the remainder of the chapter we focus on the phase behavior of the bowls. For that purpose we calculated the free energies as explained in the Methods section. The results of the reference free energy calculations are shown in Tbls. 5.1 and 5.2.

We find that the columnar phase with all the particles pointing in the same direction is more stable than the inverted columnar phase, where half of the columns are upside down. However, the free energy difference between the two phases is only  $0.013 \pm 0.002 k_B T$  per particle at  $\phi = 0.5193$  and  $D = 0.3\sigma$ . Based on this small free energy difference we do not expect polar ordering to occur spontaneously. Similar conclusions, based on direct simulations, were already drawn in Ref. [86].

The dense-packed crystal structures in Fig. 5.8 at  $D \lesssim 0.3$ , the worm-like fluid phase (Fig. 5.2) and the columnar phase (Fig. 5.6) show striking similarity in the local structure: in all these phases the bowls are stacked on top of each other, such that (part of) one bowl fits into the dent of another bowl. As a result, the free energies and pressures of the various phases, are often almost indistinguishable near coexistence. For this reason it was sometimes difficult to determine the coexistence densities for  $D < 0.3\sigma$ . Exemplary free energy curves for the various stable phases consisting of bowls with  $D = 0.3\sigma$  are shown in Fig. 5.9.

### 5.4.4 Phase diagram

In Fig. 5.10, we show the phase diagram in the packing fraction  $\phi$  - thickness  $D/\sigma$  representation. The packing fraction is defined as  $\phi = \frac{\pi D}{4}(\sigma^2 - D\sigma + \frac{2}{3}D^2)N/V$ . For  $D/\sigma \leq 0.3$ , we find an isotropic-to-columnar phase transition at intermediate densities, which resembles the phase diagram of thin hard discs [95]. However, the fluid-columnar-crystal triple point for discs is at a thickness-to-diameter ratio of about  $L/\sigma \sim 0.2 - 0.3$ , while in our case the triple point is at about  $D/\sigma \sim 0.3 - 0.4$ . The shape of the bowls stabilizes the columnar phase compared to the fluid and the crystal phase. We find four stable crystal phases IX, IB, IX' and fcc<sup>2</sup>, while we had six candidate crystals: five from the pressure

phase	$D/\sigma$	$\rho_{\text{fluid}}$	$\rho_{\text{col}}$	$f_{\text{diff}}$
fluid-col	0	1.461	4.679	7.33272

phases	$D/\sigma$	$\phi_{\text{fluid}}$	$\phi_{\text{col}}$	$f_{\text{diff}}$
fluid-col	0.1	0.1780	0.2848	3.2630(7)
fluid-col	0.2	0.3116	0.4674	3.268(2)
fluid-col	0.3	0.3760	0.5193	3.802(1)
fluid-inv col	0.3	0.3760	0.5193	3.8155(8)
fluid-col	0.4	0.4440	0.5772	5.843

**Table 5.1:** Free energy differences,  $f_{\text{diff}} \equiv (F_{\text{col}}(\rho_{\text{col}}) - F_{\text{fluid}}(\rho_{\text{fluid}}))/(Nk_B T)$ , between the (inverted) columnar phase at density  $\rho_{\text{col}}$  or packing fraction  $\phi_{\text{col}}$  and the fluid phase at  $\rho_{\text{fluid}}$  or  $\phi_{\text{fluid}}$ . In the column “phases”, “col” denotes the columnar phase and inverted columnar phase is abbreviated to “inv col”.

phase	$D/\sigma$	$\phi$	$f_{\text{exc}}$
IX	0.3	0.6669	15.505(4)
IB	0.3	0.6971	18.407(3)
IX	0.4	0.6177	12.52(1)
IB	0.4	0.6170	13.195(2)
IX	0.45	0.6768	17.918(2)
IB	0.45	0.6662	14.9873(4)
fcc <sup>2</sup>	0.45	0.6192	12.8591(5)
IX'	0.45	0.6950	18.170(5)
fcc <sup>2</sup>	0.5	0.5455	8.7673(7)
IX'	0.5	0.5597	10.854(3)

**Table 5.2:** Excess free energies,  $f_{\text{exc}} \equiv (F - F_{\text{id}})/(Nk_B T)$ , of the various crystal phases, where  $F_{\text{id}}$  is the ideal gas free energy. The various crystal phases are labeled as in Fig. 5.8.

annealing method and fcc<sup>2</sup>. The two phases that were not stable are the X and B crystals, which are very similar to the stable IX and IB crystals respectively, except that X and B have considerable lower close packing densities. Therefore, one could have expected these phases to be unstable. On the other hand, we observe from the phase diagram, that IX is stable at intermediate densities for  $0.25\sigma < L < 0.45\sigma$ , while IB packs better than IX. In other words, stability can not be inferred from small differences in packing densities.

Almost all coexistence densities were calculated by employing the common tangent construction to the free energy curves, except for the col-IX coexistence at  $D = 0.1\sigma$  and  $0.2\sigma$ . At these values of  $D$  the transition occurs at very high pressures, while the free

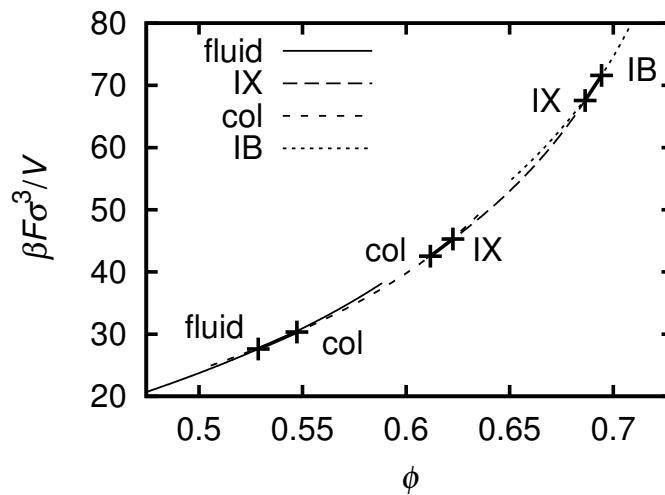


**Figure 5.9:** Dimensionless free energies  $\beta F \sigma^3/V$  for hard bowls with  $L = 0.3\sigma$  and the fluid-columnar, columnar-IX and IX-IB coexistences, which were calculated using common tangent constructions. The columnar phases is denoted “col”. The irrelevant free energy offset is defined in such a way that the free energy of the ideal gas reads  $\beta F/V = \rho(\log(\rho\sigma^3) - 1)$ . The free energies of the various phases are so close, that they are almost indistinguishable.

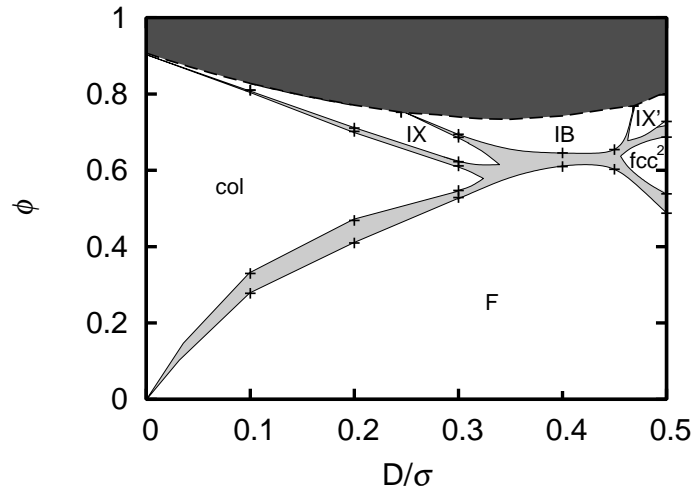


**Figure 5.10:** Phase diagram in the packing fraction ( $\phi$ ) versus thickness ( $D$ ) representation. The light gray areas are coexistence areas, while the state points in the dark gray area are inaccessible since they lie above the close packing line. IX, IB, IX' and fcc<sup>2</sup> denote the crystals as shown in Fig. 5.8, “F” is the fluid and “col” is the columnar phase. The lines are a guide to the eye. Worm-like stacks were found in the area marked “worms” bounded from below by the dashed line. On this line the probability to find a particle in a cluster that consists of more than two particles,  $\mathcal{P}_{\text{stack}}(n > 2)$ , is equal to one half.

energy of the columnar phase is calculated at the fluid–col transition, which occurs at a low pressure. To get a value for the free energy of the columnar phase we would have to integrate the equation of state up to these high pressures, accumulating integration errors. Furthermore, we expect the coexistence to be rather thin, which would further complicate the calculation. So, instead we just ran long variable box shape  $NPT$  simulations to see at which pressure the IX phase melts into the inverted columnar phase. As the free energy difference between the inverted columnar phase and the columnar phase is small, we assume that this is the coexistence pressure for the col–IX transition, although technically it is only a lower bound. The density of the columnar phase at this pressure is determined using a local fit of the equation of state. All coexistences are tabulated in Tbl. 5.3. We draw a tentative line in the phase diagram to mark the transition from a structureless fluid to a worm-like fluid i.e. a fluid with many stacks. In a dense but structureless fluid, stacks of size 2 are quite probable, but larger stacks occur far less frequently. We calculate the probability to find a particle in a stack that contains more than 2 particles  $\mathcal{P}_{\text{stack}}(n > 2) = 1 - \mathcal{P}_{\text{stack}}(1) - \mathcal{P}_{\text{stack}}(2)$  and define when the system is worm-like by the criterion  $\mathcal{P}_{\text{stack}}(n > 2) \geq 1/2$ . We do not imply that the transition to the worm-like phase is a true phase transition; the transition is rather continuous.

## 5.5 Summary and discussion

We have studied the phase behavior of hard bowls in Monte Carlo simulations and in experiments. In both systems, we find that the bowls have a strong tendency to form

$D/\sigma$	phase 1	phase 2	$\rho_1\sigma^3$	$\rho_2\sigma^3$	$\beta P\sigma^3$	$\mu^*$
0	fluid	col	4.083	4.824	26.11	15.22

$D/\sigma$	phase 1	phase 2	$\phi_1$	$\phi_2$	$\beta Pd^3$	$\mu^*$
0.1	fluid	col	0.2778	0.3297	26.35	15.59
0.1	col	IX	0.8095	0.8104	$2.7 \cdot 10^3$	-
0.2	fluid	col	0.4096	0.4688	27.23	16.68
0.2	col	IX	0.7021	0.7108	325	-
0.3	fluid	col	0.5286	0.5472	49.52	26.13
0.3	col	IX	0.6864	0.6944	281.4	91.03
0.3	IX	IB	0.6117	0.6226	110.9	44.92
0.4	fluid	IB	0.609765	0.645511	105.9	51.06
0.45	fluid	IB	0.6026	0.6545	87.92	46.90
0.5	fluid	fcc <sup>2</sup>	0.4878	0.5383	28.34	22.10
0.5	fcc <sup>2</sup>	IX'	0.6870	0.7278	139.2	67.36

**Table 5.3:** Reduced densities, pressures and chemical potentials  $\mu^* = \beta\mu - \ln(\Lambda_t^3\Lambda_r/\sigma^3)$  of the coexisting phases for hard bowl-shaped particles with thickness  $D$ .

stacks, but the stacks are bent and not aligned. We measured the equation of state and the compressibility in Monte Carlo *NPT* simulations. The pressure we obtained from these simulations is concave for some range of densities for deep bowls. This is due to the increase in free volume when large stacks form. Using  $g_e(z)$ , the pair correlation function along the direction vector, we showed that the concavity of the pressure coincides with a dramatic change in structure from a homogeneous fluid to the worm-like fluid. We measured the stack distribution both in the experiments and in the simulations. The experimental distribution shows excellent agreement with the simulation results for  $D = 0.3\sigma$ , where  $D$  is the thickness of our model particle. This is in agreement with the distance between two neighboring particles within a stack in experiments, which is equal to the thickness  $D$  for large pressure in simulations. When the pressure is increased slowly the deep bowls (which are difficult to achieve experimentally with our synthesis route) spontaneously order into a columnar phase in our simulations. This poses severe restrictions on the thickness of future bowl-like mesogens (molecular or colloidal), which are designed to easily order into a globally aligned lyotropic columnar phase. As the experimental system did not show spontaneous ordering, we determined the phase diagram using free energy calculations in computer simulations for a particle shape ranging from an infinitely thin bowl to a solid hemisphere. We find that the columnar phase is stable for  $D \leq 0.3\sigma$  at intermediate packing fractions. In addition, we show using free energy calculations that the stable columnar phase possesses polar order. However, the free energy penalty for flipping columns upside down is very small, which makes it hard to achieve complete polar ordering in a spontaneously formed columnar phase of bowls. Future work should be focused on new routes to synthesize deeper bowl-shaped particles or on additional control to obtain polar ordering by applying external fields.

## Acknowledgments

The experiments that were described in this chapter were performed by Rob Kortschot, Ahmet Demirors and Arnout Imhof. We especially thank Arnout Imhof for useful discussions concerning the experiment and the relation between the colloidal particle and the model particle that was used in the simulations.

## Appendix 5.A Overlap algorithm

The overlap algorithm for our bowls checks whether the surfaces of two bowls intersect. Fig. 5.1 shows that the surface of the bowl consists of two parts. Part  $p$  of the surface contains the part of the surface of the sphere of radius  $R_p$ , within an angle  $\theta_p$  from the  $z$ -axis, where  $p = 1$  denotes the smaller sphere and the larger sphere is labeled  $p = 2$ . We set  $\theta_1 = \pi/2$ , to get a hemispherical outer surface. The edges of both surfaces have to coincide, such that our particles have a closed surface. Using this restriction  $L$ ,  $\theta_2$  and  $R_2$  can all be expressed in terms of the radius of the smaller sphere,  $R_1$ , and the thickness of the bowl  $D$ , in the following way:

$$R_2 = R_1 + \frac{D^2}{2(R_1 - D)} \quad (5.19)$$

$$\theta_2 = \arcsin(R_1/R_2) \quad (5.20)$$

$$L = R_2 \cos(\theta_2). \quad (5.21)$$

Overlap occurs if either of the two parts of the surface of a bowl overlaps with either of the two parts of another bowl. So we have to check four pairs of infinitely thin (and not necessarily hemispherical) bowls, labeled  $i$  and  $j$ , for overlap. The existence of such an overlap or intersection is checked in three steps.

- First, we check whether the full surfaces of the spheres intersect, i.e.  $|R_i - R_j| < r_{ij} \equiv |\mathbf{r}_j - \mathbf{r}_i| < R_i + R_j$ . If this intersection does not exist, there is no overlap, otherwise we proceed to the next step.
- Secondly, we determine the intersection of the surface of each sphere with the other bowl. The intersection of bowl  $i$  with the sphere of bowl  $j$  exists if

$$|\omega_{ij} + \zeta\phi_{ij}| < \theta_i \quad (5.22)$$

for  $\zeta = 1$  or  $-1$ , where

$$\cos(\phi_{ij}) = \frac{R_i^2 - R_j^2 + r_{ij}^2}{2r_{ij}R_i} \text{ and} \quad (5.23)$$

$$\cos(\omega_{ij}) = \frac{\mathbf{u}_i \cdot \mathbf{r}_{ij}}{r_{ij}}. \quad (5.24)$$

see Fig. 5.11a. This intersection is an arc, which is part of the circle that is the

intersection between the two spheres. If in fact this arc is a full circle and the other particle has a nonzero intersection, the particles overlap. This is the case when Eq. (5.22) holds for  $\zeta = 1$  and  $\zeta = -1$ . If, on the contrary, either of the two arcs does not exist, there is no overlap. Otherwise, if both arcs exist, but neither of them is a full circle, proceed to the next step.

- Finally, if the two arcs overlap there is overlap, otherwise the particles do not overlap. The arcs overlap if

$$|\alpha_{ij}| < |\gamma_i| + |\gamma_j|, \quad (5.25)$$

where

$$\cos(\alpha_{ij}) = \frac{\mathbf{n}_i^\perp \cdot \mathbf{n}_j^\perp}{|\mathbf{n}_i^\perp| |\mathbf{n}_j^\perp|} \quad (5.26)$$

$$\cos(\gamma_i) = \frac{\cos(\theta_i) - \cos(\phi_{ij}) \cos(\omega_{ij})}{\sin(\phi_{ij}) \sin(\omega_{ij})}, \quad (5.27)$$

where  $\mathbf{n}_i^\perp = \mathbf{n}_i - (\mathbf{r}_{ij} \cdot \mathbf{n}_i) \mathbf{r}_{ij} / r_{ij}^2$  and the expressions for  $\gamma_j$  and  $\mathbf{n}_j^\perp$  are equal to the expressions for  $\gamma_i$  and  $\mathbf{n}_i^\perp$  with  $i$  and  $j$  interchanged. The arcs together with the relevant angles are drawn in Fig. 5.11b.

The inequalities (5.22) and (5.25) are expressed in cosines and sines using some simple trigonometry. In this way no inverse cosines need to be calculated during the overlap algorithm.

For  $D = 0.5\sigma$  the bottom surface is a disk rather than an infinitely thin bowl. So the overlap check consists of bowl–bowl, bowl–disc and disc–disc overlap checks. For brevity,

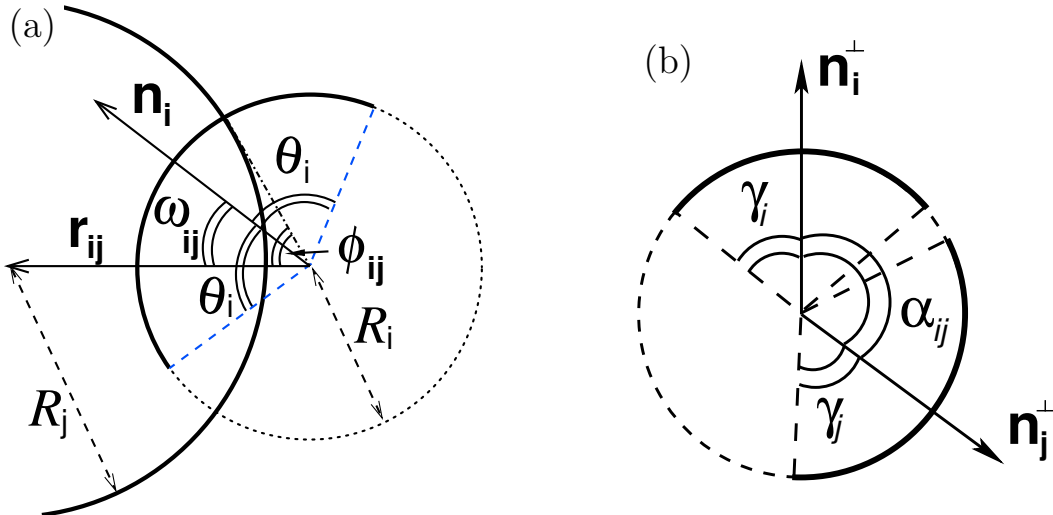


**Figure 5.11:** The relevant lengths and angles which are used in the first and second steps (a) and in the third step (b) of the overlap algorithm. Shown are bowl  $i$  and (part of) the sphere of bowl  $j$  (a), the arcs of  $i$  and  $j$  and the circular intersection of the spheres of  $i$  and  $j$  (b). In (a)  $\mathbf{r}_{ij}$  lies in the plane, while the plane of view in (b) is perpendicular to  $\mathbf{r}_{ij}$ . In this case, the sphere of particle  $j$  overlaps with bowl  $i$ , but the arcs do not overlap, so particle  $i$  and particle  $j$  do not overlap.

we will not write down the bowl–disk overlap algorithm, but it can be implemented in a similar way as the algorithm for bowl–bowl overlap described above. The disk–disk overlap algorithm was already implemented by Eppenga and Frenkel [99].

---

## Phase behavior of cusp-free platelets

---

In this chapter we investigate the phase behavior of a cusp-free model for platelets: the hard oblate spherocylinder (OHSC) using free energy methods. We confirm some of the results from an earlier study [100], although we find one columnar phase and two crystal structures instead of three columnar phases. We compare the results to the phase diagram of cut spheres [95], which have two circular cusps. Since the cut sphere has a similar shape to the OHSC, the phase diagram of the two types of particles are quite similar. However, we find an additional crystal phase for the OHSC, which is of a type of crystal that is frequently found in experiments on disc-like molecules. Furthermore, although we have found a cubatic phase, it was shown to be unstable, unlike the cubatic phase of cut spheres. Finally, we also show that the phase boundaries shift significantly compared to cut spheres. These are remarkable consequences of a subtle change in shape, which show that for a detailed comparison to the phase behavior of experimental particles, which usually do not have appreciable cusps, the OHSC should be used as a model particle.

## 6.1 Introduction

Disk-like molecules are one of the most common particles that form liquid crystal phases, in particular columnar phases, which are interesting for applications [90]. The most common model for hard discs or platelets that form a columnar phase is the cut sphere [95, 101, 102], which is a sphere where a top and bottom section are chopped off. Some concern has been expressed [100] that the sharp edges or cusps of the top and the bottom plane of the particle make the cut sphere a poor model for the shape of molecular mesogens. Furthermore, it is difficult to add attractions to the model that have the same shape anisotropy as the core. As there is no upper limit on the size of the molecules that can display liquid crystalline behavior, as long as sufficient thermal motion is present, also colloidal rods [71, 103] and disks [104, 105] can form liquid crystals. These colloids are stabilized either by charge repulsive or steric interactions, which tend to round off any sharp features of the underlying bare particles. So a model particle without cusps is required to model these colloidal mesogens. The rod-like colloids are usually modeled as spherocylinders and disc-like colloids as cut spheres [102, 106]. Cut spheres, unlike spherocylinders, have cusps on their surfaces, so it is interesting to investigate the effect of these cusps, by comparing the phase behavior of cut spheres to the phase behavior of cusp-free platelets. In analog to the (prolate) spherocylinder, where the particle is defined as the volume within a certain distance from a line, an oblate spherocylinder can be defined by the volume within a certain distance to a circle [107]. For both prolate and oblate spherocylinders the particle-particle interactions are defined using a closest distance between the lines and circles respectively. For hard particles an overlap occurs if this closest distance is smaller than a certain distance. This hard core interaction can be replaced by a soft and/or attractive potential, that is a function of only one variable, the closest distance. Defining the potential in this way preserves the shape of the particles. In Ref. [100] the phase diagram of oblate hard spherocylinders (OHSC) was tentatively explored using direct simulations. Three columnar phases were found for  $0.2 \leq L/D \leq 0.5$ , where  $L$  is the thickness of the platelet and  $D$  its diameter. At high densities the particles form columns that are interdigitated in the so-called interdigitated columnar phase ( $D_{hi}$ ). As the density is decreased this  $D_{hi}$  phase melts into a columnar phase ( $D_{ho}$ ) with local ordering within the columns, which melts into a disordered columnar phase ( $D_{hd}$ ) at even lower density. In this chapter we study the phase behavior of this system of cusp-free platelets using free energy calculations. We first explain the method we used to find candidate crystal structures, and the free energy methods we employed. Subsequently, we show our results, which include the packing diagram and the phase diagram. Finally, we summarize our results.

## 6.2 Model

We consider a system consisting of cusp-free hard platelets. We model the platelets as oblate hard spherocylinders (OHSC), which have been extensively described in previous work [100, 107–113]. Therefore, we will only briefly describe the shape of our platelets. The OHSC consists of a flat cylindrical core with diameter  $\sigma$  and height  $L$ , and a toroidal

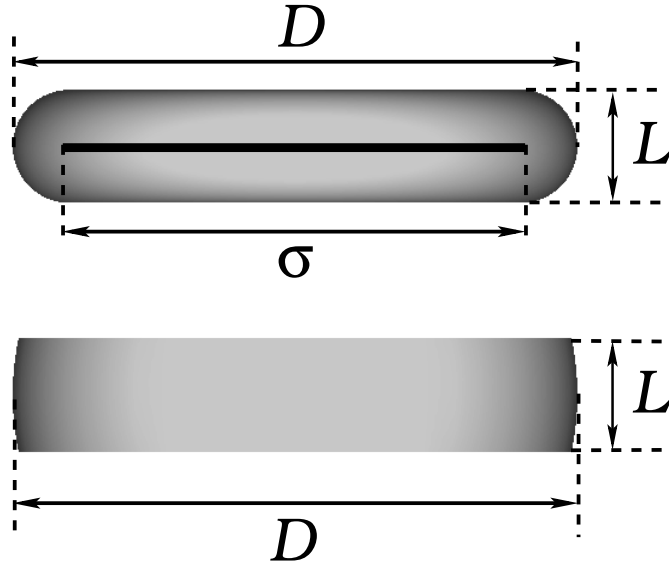


**Figure 6.1:** The oblate hard spherocylinders (OHSC) considered in this study (top), compared to cut spheres (bottom), for  $L = 0.2D$ , where  $L$  is the thickness of the platelets and  $D$  the diameter. An OHSC is obtained by padding a circle of diameter  $\sigma$ , as indicated by the black line, with a layer of uniform thickness  $L/2$ .

rim, with tube diameter  $L$ , see Fig. 6.1. Consequently the total diameter of the OHSC is  $D = L + \sigma$ . We detect overlaps between OHSC using the efficient, although partially numerical algorithm, which was introduced in Ref. [100].

### 6.3 Methods

In this section we briefly reiterate the methods we employed to study the phase behavior using Monte Carlo simulations, as these methods have been described extensively in Chaps. 3 and 5. First, we use the pressure annealing method to obtain candidate crystal structures. Then we use the modified Einstein integration method as described by Eqs. (3.13) to (3.15), to obtain the free energy of these crystals at a certain reference density. Since our particles, like the dumbbells, have an up-down symmetry, we use the same angular potential energy function as in Eq. (3.13). The interpenetrable particle-particle potential in this case is set to Eq. (5.13), with  $r'_{ij}$  equal to the closest distance between the circles in the middle of the particles and  $\sigma_{\max} = L$ . We also use Widom insertion [79] to obtain the chemical potential and therefore the free energy of the isotropic fluid and the nematic phase at a reference density (see Eq. (5.2)). Thirdly, we use the method by Bates and Frenkel [96] as described in Eqs. (5.5) to (5.9), to get the free energy difference between the columnar phase at a reference density and the fluid phase at a lower density. Finally, we integrate over the equation of state as described in Eq. (5.14), to obtain the free energy as a function of density. The equations of state for the crystal and the columnar phase were calculated using  $NPT$  simulations, where the length of the box vectors were allowed to change, but the angles between the box vectors were fixed at 90

degrees. It was not necessary to allow these angles to adjust as the stable crystals all have rectangular unit cells. We checked that there was no difference between the equations of state that were obtained using *NPT* simulations with a rectangular box shape and simulations with a fully adjustable box shape. The equations of state of the fluid and the nematic phase were obtained from Ref. [100] and Ref. [114] when available. Otherwise, the equation of state of the fluid was obtained from event driven molecular dynamics (MD) simulations, as described below. Two oblate spherocylinders overlap, when the closest distance between the two central discs (see Fig. 6.1) is shorter than  $L$ . Therefore, one can easily determine a collision event, that occurs when the closest distance between two particles is equal to  $L$ . As a result, we can use event driven MD simulations to investigate the phase behavior of the hard oblate spherocylinders. The advantage of event driven MD simulations over Monte Carlo simulations is the fast accumulation of statistics of the pressure [7]. In our *NPT* Monte Carlo simulations the density changes by volume moves, which makes the density equilibrate slowly, especially for large numbers of particles. In the MD the pressure is calculated from the collisions [7], and therefore comes for free with the integration of the equations of motion. Unfortunately, the shape of the simulation box needs to be known a priori, since the equilibration of the shape is just as slow or slower than the equilibration of the density. Therefore, the event driven MD simulations were most useful for the isotropic fluid and nematic phases. We implemented the event driven simulation similarly as described in Ref. [115], except for the way we checked for grazing collisions (i.e. near misses). In an event driven MD of anisotropic particles, one searches for collisions on a grid in time i.e. pairs of particles are moved forward in time and checked for overlap at regular intervals. In the event of a grazing collision, an overlap occurs in between two grid points, while no overlap is found at the grid points. Without a way to check for these grazing collisions, they will be missed, resulting in overlaps. In Ref. [115], a change in sign of the time derivative of the closest distance signals the presence of a minimum, which is a necessary condition for a grazing collision. Unfortunately, we were unable to find a robust and efficient way to calculate the time derivative of our numerical closest distance. Instead, we look for a minimum by comparing the closest distance at the middle of three grid points to the closest distance at the other two. If this closest distance is smaller than a certain cut off, we use a standard numerical routine to find the minimum and check whether this closest distance is smaller than  $L$ , in which case a collision is detected. Once a collision has been found we use a standard numerical root finder to locate the exact time of the collision.

To determine the isotropic–nematic coexistence we use a rather simple method: We simply measure the pressure from the collisions and the chemical potential by the Widom particle insertion method [79]. Subsequently, we fit lines through the chemical potential as a function of pressure and define the coexistence as the crossing point of these two lines. This would not have been possible using an *NPT* Monte Carlo simulation, because (i) very long simulations would be required to sufficiently reduce the statistical error and (ii) the large system size required to prevent the system from fluctuating between the isotropic and the nematic phase would slow down the *NPT* simulations even further.

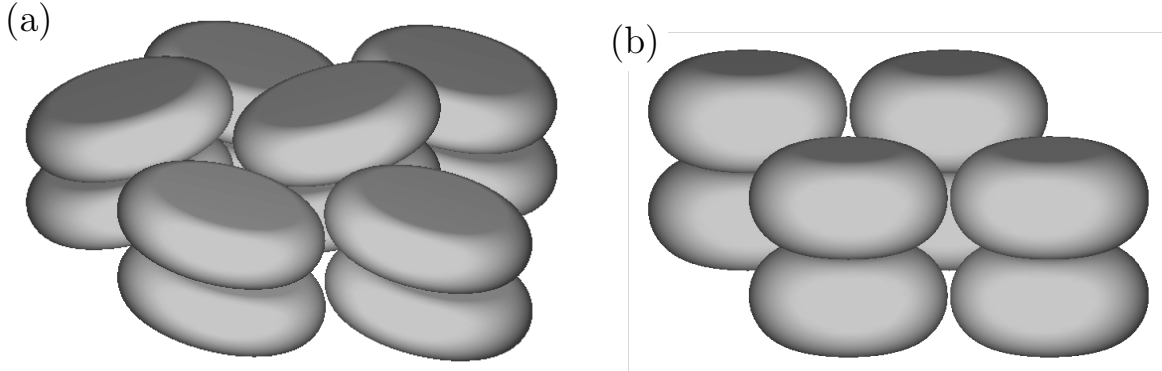


**Figure 6.2:** The unit cells of the tilted crystal phase for  $L = 0.3D$  (a) and the aligned crystal phase for  $L = 0.5D$  (b).

## 6.4 Results

We employ the pressure annealing method to find candidate crystal structures for the oblate hard spherocylinders. We find only two crystal structures for  $0 < L/D < 0.5$ , while we found 6 structures for the bowls in Chap. 5. The particles in both crystal structures are stacked in columns and both crystals have a body centered orthorhombic unit cell, see Fig. 6.2. One phase that we expected to find is the equivalent of the close packed phase for cut spheres, although slightly stretched to accommodate the slightly different form of the OHSC. This phase consists of columns of platelets that are aligned along the  $z$ -axis i.e.  $\mathbf{u}_i$  is along  $z$  for all particles  $i$ , where the  $z$ -direction is in the direction of the column. The columns are shifted with respect to each other in the  $z$ -direction, such that each column interdigitates with 4 of its neighboring columns, while each particle is at the same  $z$ -position as two particles in the other two neighboring columns. In the other crystal phase, particles again form columns. The particles in half of these columns tilt compared to the  $z$ -axis in the  $x$ -direction, where the  $x$ -axis is along the lattice vector perpendicular to  $z$ . The other half of the particles is tilted by the same angle in the  $-x$ -direction. In this way each column interdigitates with all six of its neighbors. Some molecular mesogens also form tilted crystals [90], which were explained by calculating packing energies [116], but cut spheres do not [95]. The packing fractions of these phases are shown in Fig. 6.3 as a function of  $L$ . We see that the OHSC always pack less dense than the cut spheres. We determined the lattice vectors (of the primitive unit cell) of the first, aligned crystal phase ( $X_{\text{aligned}}$ ):

$$\begin{aligned} \mathbf{a}_1 &= D\hat{x} & \mathbf{a}_2 &= L\hat{z} \\ \mathbf{a}_3 &= \frac{D}{2}\hat{x} + \sqrt{\left(\sigma + \frac{L}{2}\sqrt{3}\right)^2 - \left(\frac{D}{2}\right)^2} \hat{y} + \frac{L}{2}\hat{z}, \end{aligned} \tag{6.1}$$

and the particles are aligned along  $z$ . These lattice vectors result in a density:

$$\rho D^3 = DL \sqrt{\left(\sigma + \frac{L}{2}\sqrt{3}\right)^2 - \left(\frac{D}{2}\right)^2}. \tag{6.2}$$

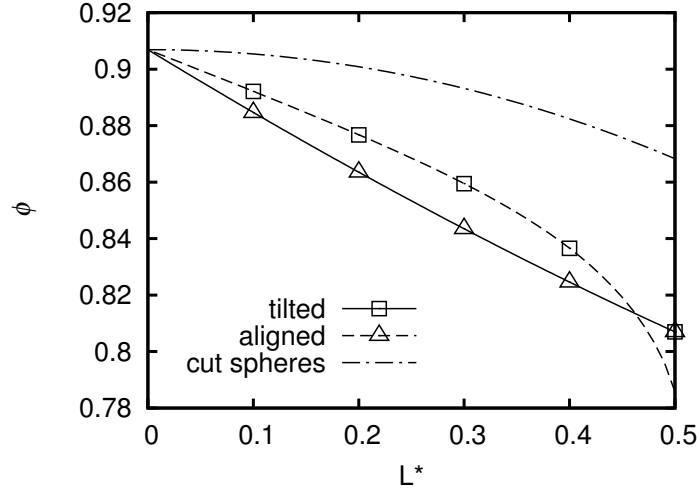


**Figure 6.3:** Packing diagram: maximum packing fraction,  $\phi \equiv (\frac{\pi}{6}L^3 + \frac{\pi^2}{8}\sigma L^2 + \frac{\pi}{4}\sigma^3)N/V$ , of the tilted and aligned crystal phases as a function of dimensionless thickness,  $L^* \equiv L/D$ , for the OHSC. The points are the results of the pressure annealing. The thin lines are obtained from the analytical expression for the aligned crystal phase (solid line), while, for the more complex tilted crystal phase, we used single high pressure runs with most of the degrees of freedom fixed, as described in the text (dashed line). The packing fraction,  $\phi \equiv \frac{\pi}{4}L(D^2 - L^2/3)N/V$ , of the cut spheres as a function of  $L^* \equiv L/D$ , is shown for comparison (dot-dashed line).

We determined the lattice vectors and the direction vectors ( $\mathbf{u}_\pm$ ) of the tilted crystal phase ( $X_{\text{tilted}}$ ) up to a free parameter  $b$ ,

$$\begin{aligned} \mathbf{a}_1 &= \left( \sigma u_z + L \sqrt{L^2 - \sigma^2 \sin^2 \theta_0} \right) \hat{x} & \mathbf{a}_2 &= b \hat{y} \\ \mathbf{a}_3 &= (L / \cos \theta_0) \hat{z} & \mathbf{u} &= \pm \sin \theta_0 \hat{x} + \cos \theta_0 \hat{z}, \end{aligned} \quad (6.3)$$

where  $\cos(2\theta_0) = \sqrt{1 - (L/\sigma)^2}$  and  $\theta_0$  is the angle between the direction vectors and the  $z$ -axis. The free parameter,  $b$ , cannot be determined analytically, since the closest distance between some of the neighboring particles in the tilted crystal can only be determined numerically. Instead,  $b$  was determined in  $NPT$  Monte Carlo simulations, which only include moves that change  $b$ . To be precise, we ran a single simulation of two particles at a pressure of  $10^6 k_B T / D^3$  for each value of  $L/D = 0.01, 0.02, \dots, 0.5$ . The resulting average packing fractions are shown in Fig. 6.3 along with the analytical result for the aligned phase as continuous lines. The packing fraction is defined as  $\phi = vN/V$ , where

$$v = \frac{\pi}{6}L^3 + \frac{\pi^2}{8}\sigma L^2 + \frac{\pi}{4}L\sigma^2 \quad (6.4)$$

is the volume of a OHSC. Additionally, we show the packing fraction of the close packed crystal for cut spheres in Fig. 6.3, which is clearly higher than the maximum packing fraction of OHSC for all elongations.

The coexistence between the isotropic fluid phase and the nematic phase were determined from the pressure and the chemical potential, that were both directly measured in

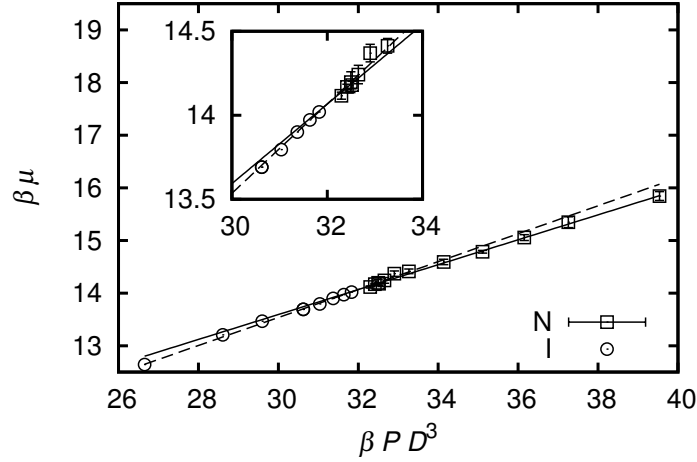


**Figure 6.4:** The dimensionless chemical potential ( $\beta\mu$ ) versus the dimensionless pressure ( $\beta PD^3$ ) for the isotropic (I) and the nematic phase (N) near coexistence for a system of OHSC with  $L/D = 0.1$ . The chemical potential is shifted such that the ideal gas chemical potential reads  $k_B T \log(\rho D^3)$ . The errors in the pressure and the errors in the chemical potential data for the isotropic phase are smaller than the symbol size. The lines are fits to the data.

event driven MD simulations. In Fig. 6.4, the chemical potential as a function of pressure is plotted for  $L/D = 0.1$  along with fits to the data. The coexistence pressure defined by the intersection of these fits is  $D^3 P_{IN}/k_B T = 32.0 \pm 0.1$ . The coexistence packing fractions as obtained using local fits to the equation of state, are shown in the phase diagram (Fig. 6.5a). The aligned crystal ( $X_{\text{aligned}}$ ) changed spontaneously into the  $X_{\text{tilted}}$  crystal phase for  $L/D \leq 0.4$  in a diffusionless transition (which is not a Martensitic transition, because there is no shearing involved). Aside from the nematic phase and the two crystal phases, that were already mentioned, the phase diagram also features a columnar phase. The coexistences between the isotropic fluid and the crystal and columnar phases were calculated using common tangent constructions on the free energy curves. The columnar–crystal coexistence pressure is the pressure at which the crystal melted and the corresponding coexistence densities are found using a fit to the equation of state. This means that these coexistence densities are actually lower bounds, except for  $L = 0.3D$ , where the columnar phase crystallized spontaneously with very little hysteresis. The free energy calculations at  $L = 0.3D$  show that the columnar phase-to-crystal phase transition is only very weakly first order or even second order.

We compare the phase diagram from this work with the phase diagrams of Refs. [100] and [95] in the panel on the right in Fig. 6.5. Our coexistence areas (in gray) are plotted into the phase diagram (Fig. 6.5b) as obtained using direct simulations of OHSC in Ref. [100]. At a first glance, there are almost no similarities between our phase diagram and the phase diagram from Ref. [100], since there is only one columnar phase, instead of three distinct columnar phases, while there are two crystal phases in our phase diagram. The simulations in Ref. [100] were initiated in a columnar phase, which might be the reason why no crystal phases were reported. We also see that the strongly first order phase transitions, i.e. from the isotropic to the columnar or crystal phases, are shifted.

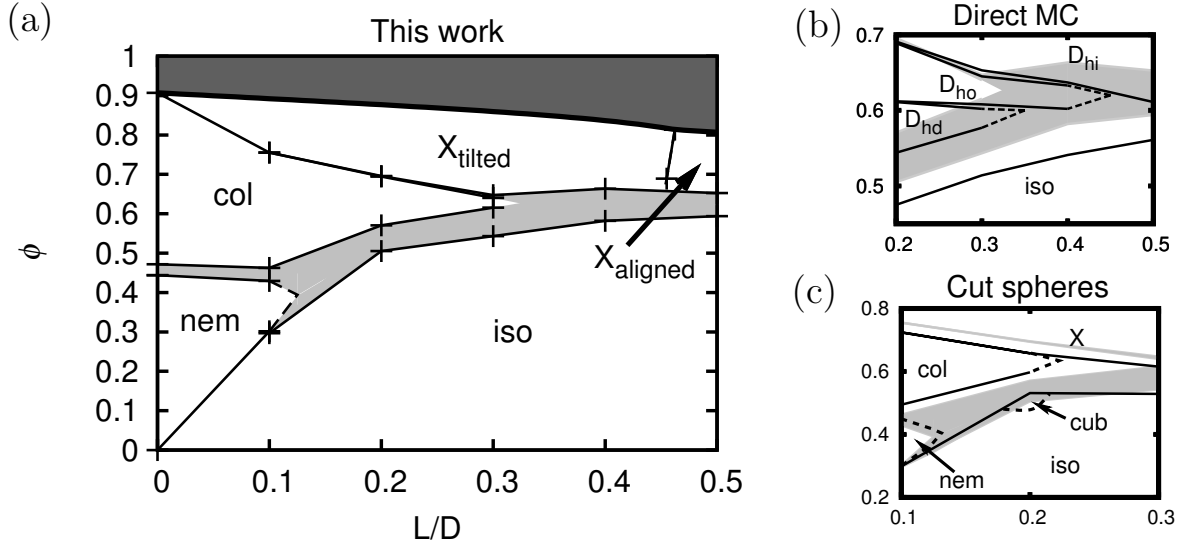


**Figure 6.5:** Phase diagram in the packing fraction ( $\phi$ ) versus dimensionless thickness ( $L/D$ ) representation as obtained by free energy calculations in this work (a). The state points in the dark gray area are inaccessible since they lie above the maximum close packing line.  $X_{\text{aligned}}$  and  $X_{\text{tilted}}$ , denote the aligned and tilted crystal structures as shown in Fig. 6.2, “iso” is the isotropic fluid, “nem” the nematic phase, and “col” is the columnar phase. The dashed lines enclose estimated areas of stability for phases where we do not have simulation data. The solid lines are a guide to the eye, connecting coexistence points found in our simulations and, for  $L/D = 0$ , from Ref. [96]. In the panel on the right, we compare our results for OHSC (gray coexistence areas) to the phase diagrams in  $L/D$ – $\phi$  representation as obtained by direct simulations of OHSC (b) in Ref. [100] and free energy calculations on cut spheres (c) in Ref. [95]. The various phases are labeled as in the previous works, and include, aside from the phases already mentioned, the three columnar phases  $D_{\text{hd}}$ ,  $D_{\text{ho}}$  and  $D_{\text{hi}}$  (see text) from Ref. [100] and the cubatic (cub) and crystal (X) phases of the cut spheres from Ref. [95].

This is to be expected, as for such first-order transitions usually a large free energy barrier needs to be overcome to crystallize. The transition from the columnar phase to the tilted crystal phase, occurs at nearly the same packing fraction as the  $D_{\text{ho}}$  to  $D_{\text{hi}}$  transition in Ref. [100]. This, combined with the fact that the equation of state of the  $D_{\text{hi}}$  and the  $X_{\text{tilted}}$  phases are very similar, leads to the conclusion that the  $D_{\text{hi}}$  columnar phase from Ref. [100] is actually an  $X_{\text{tilted}}$  or  $X_{\text{aligned}}$  crystal with many defects. In Fig. 6.5a, we do not distinguish between the other two columnar phases  $D_{\text{ho}}$  and  $D_{\text{hd}}$ , where the first has more order than the second. It should be noted, that, at least for  $L \geq 0.3D$ , the  $D_{\text{hd}}$  phase was found at packing fractions below the melting transition of the columnar phase as calculated using our full free energy calculations. In other words, we find only one columnar phase for the OHSC, with the possible exception of a small pocket in the phase diagram around  $L = 0.2D$ . In summary, we find that our phase boundaries deviate considerably from the earlier work in Ref. [100], but this can easily be explained by the fact that our phase diagram is obtained using free energy calculations and the pressure annealing method to find crystal structures, while the previous work was obtained from direct simulations starting from a columnar phase.

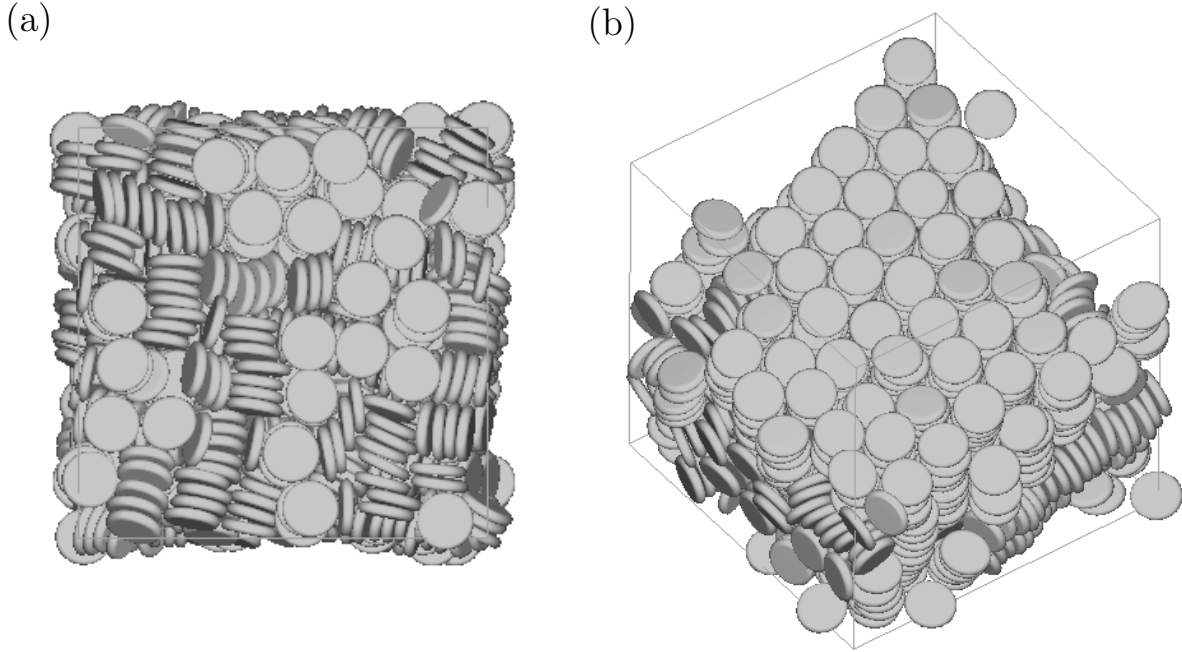


**Figure 6.6:** The configuration at  $t = 1200\tau$  (a) and the final configuration at  $t = 6700\tau$  (b), where  $\tau^2 = mD^2/k_BT$ , of an event driven MD simulation of OHSC for  $L = 0.2D$  at packing fraction,  $\phi = 0.6$ . In the final configuration some particles are removed to expose a columnar cluster.

The other popular model for platelets, the cut sphere, has a phase diagram which is quite similar to our phase diagram (see Fig. 6.5c), which is to be expected, since the shape of the cut sphere is not very different from the OHSC shape. There are a few interesting differences, such as the position of the isotropic–columnar–crystal triple point. This triple point is located in the range  $0.1 < L/D < 0.2$  for cut spheres, where  $L/D$  is the thickness-to-diameter ratio of the cut spheres, while in our case it lies in the range  $0.2 < L/D < 0.3$ . This is caused by the increased stability of the crystal of the cut spheres compared to the  $X_{\text{tilted}}$  phase, which can probably be related to the much better packing of the cut sphere crystal, see Fig. 5.7. The other difference between the OHSC and the cut sphere, is the absence of the cubatic phase in the phase diagram of the OHSC. Upon compression of the isotropic phase, we did indeed find a phase which resembled the cubatic phase. In Fig. 6.6a, a configuration with cubatic order is shown, which was obtained in the early stages of an event driven MD simulation of OHSC with  $L = 0.2D$  at packing fraction  $\phi = 0.6$ . We show the evolution of the nematic order parameter,  $S_2$  (as defined in Chap. 4), during this event driven MD simulation in Fig. 6.7. Note, that the nematic order parameter is zero for both the isotropic fluid and the cubatic phase (actually for our system size of 1500 particles,  $0.05 \lesssim S_2 \lesssim 0.1$  [101]). Therefore, we also show the probability distribution  $\mathcal{P}(\theta, \varphi)/\sin\theta$  of the polar ( $\theta$ ) and azimuthal ( $\varphi$ ) angles, which shows four distinct peaks around the equator ( $\theta \simeq \pi/2$ ) and two more peaks near  $\theta = 0$  and  $\pi$ , which are smeared out due to the mapping of the unit sphere onto the  $\theta, \varphi$  plane. The presence of these 6 peaks shows that there is cubatic order, however, there is one dominant nematic axis, since the nematic order parameter is considerably larger

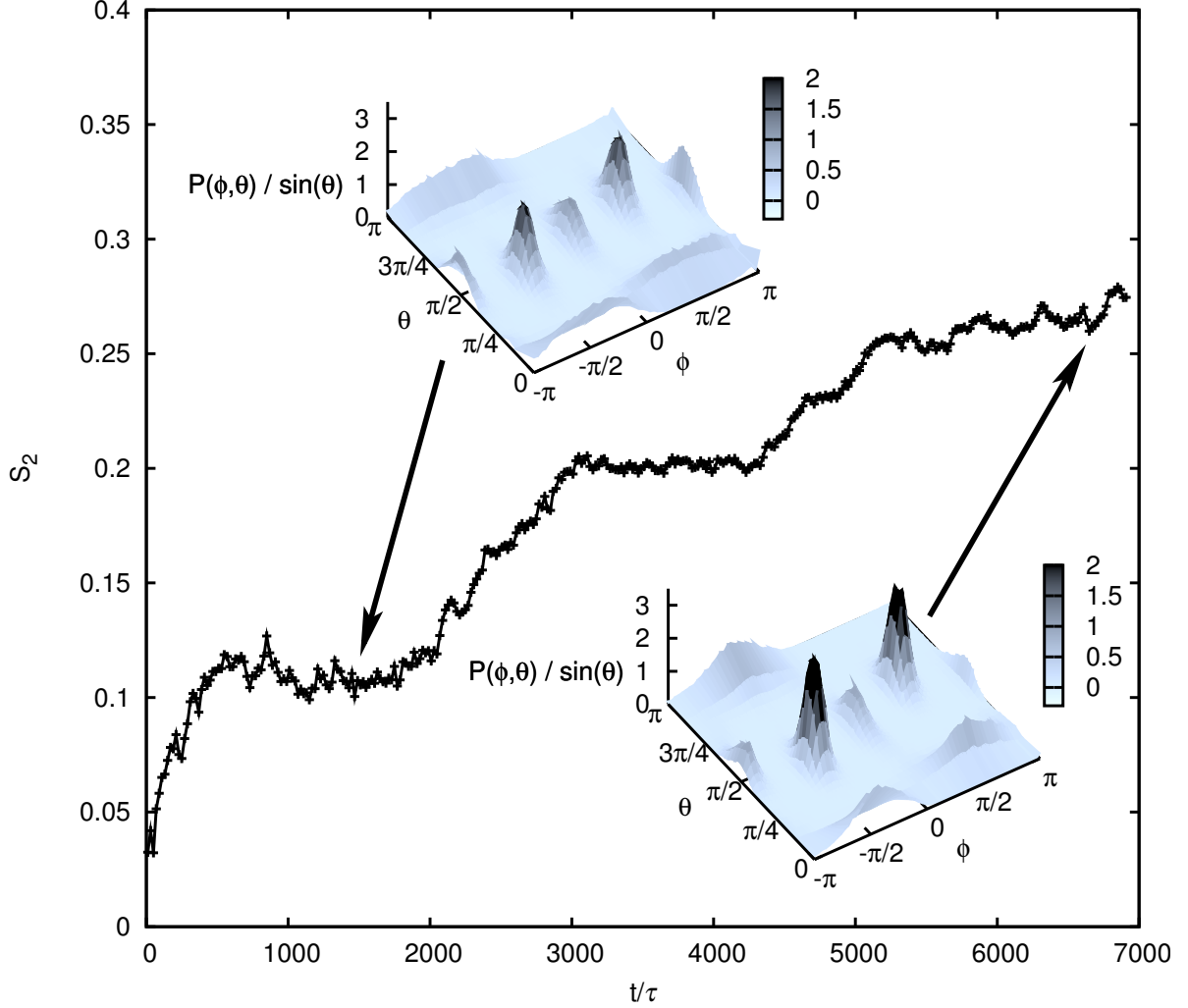


**Figure 6.7:** The nematic order parameter  $S_2$  versus time  $t/\tau$ , where  $\tau^2 = mD^2/k_BT$ , for the event driven MD simulation, for which snapshots are shown in Fig. 6.6. The insets show the angular probability distribution function  $\mathcal{P}(\theta, \varphi)/\sin\theta$ , where  $\theta$  is the polar angle (measured from the  $z$ -axis) and  $\varphi$  is the azimuthal angle.  $\mathcal{P}(\theta, \varphi)/\sin\theta$  is averaged over a time interval of  $500\tau$  centered on the time indicated by the corresponding arrow.

than zero. This can also be seen from the angular probability distribution in the insets of Fig. 6.7. Two of the peaks in this distribution are considerably higher than the other four peaks, and the difference in peak heights increases with time, as does the nematic order parameter. In other words, the cubatic phase transformed into an aligned phase during the simulation. The final snapshot of the simulation, Fig. 6.6b, shows a large columnar cluster in the system. Since the packing fraction  $\phi = 0.6$ , is above the coexistence density of the columnar phase i.e.  $\phi \simeq 0.57$ , we expect this cluster to grow until it contains all particles. Here, we find an advantage of our platelets over the cut spheres, for which it was not possible to design a simulation, which allowed a transition from the cubatic

to the columnar phase, or vice versa [101]. At packing fractions below the coexistence packing fraction of the columnar phase, we have not found any evidence of the cubatic phase. In conclusion, for the OHSC, the cubatic phase is an unstable intermediate phase, which is formed during the initial stages of the crystallization of an isotropic fluid into the columnar phase. The presence of the cubatic phase in the phase diagram for cut spheres is probably caused by the almost cylindrical shape or the cut sphere with  $L \simeq 0.2D$  (see Fig. 6.1, which stabilizes stacks of around four particles, that are rotated by 90 degrees compared to adjacent stacks (see Fig. 6.6a).

## 6.5 Summary

We determined the phase behavior of a model for hard cusp-free platelets: oblate hard spherocylinders (OHSC). Two crystal phases were found using the pressure annealing method. The first crystal is similar to the crystal structure of cut spheres, albeit with a considerably lower packing fraction. The second crystal that we found, consists of columns of particles that are tilted with respect to the column and with respect to each other. Interestingly, tilted crystals are also commonly found for disc-like molecules [90]. However, only an aligned crystal phase was found for cut spheres, which shows that the OHSC is a better model for molecular mesogens. Crystal phases have a lower close packed density than the cut spheres. We calculated the phase diagram using free energy methods. We did not find further evidence for the existence of the two separate non-interdigitated columnar phases, that were found for the OHSC in Ref. [100]. The third (interdigitated) columnar phase that was found in Ref. [100] is most likely a defect-rich variant of one of our crystal phases. The shape of the phase diagram is very similar to the phase diagram of cut spheres, with isotropic, nematic, columnar and crystal phases. However, we have found two stable crystal phases instead of one. Furthermore, we did not find a stable cubatic phase, which was found for cut spheres. These differences were explained using subtle differences in the shape of the respective particles. The isotropic-columnar-crystal triple point for the OHSC is shifted to lower  $L$  compared to cut spheres, which can be understood from packing arguments. It is surprising that the phase behavior depends so sensitively on the precise details of the particle shape, which justifies the current work and motivates the use of the OHSC as a model for particles that do not have sharp edges.

## Acknowledgments

This chapter is based on work, which was performed in collaboration with Alejandro Cuetos and Bruno Martinez Haya, whose equation of state data we used and with whom we have had many fruitful discussions.



# References

- [1] J.-B. Perrin, *Annales de Chimie et de Physique* **18**, 1 (1909).
- [2] J. Perrin, *J. Phys.* **9**, 5 (1910).
- [3] W. W. Wood and J. D. Jacobson, *J. Chem. Phys.* **27**, 1207 (1957).
- [4] B. J. Alder and T. E. Wainwright, *J. Chem. Phys.* **27**, 1208 (1957).
- [5] W. G. Hoover and F. H. Ree, *J. Chem. Phys.* **49**, 3609 (1968).
- [6] P. G. Bolhuis, D. Frenkel, S. C. Mau, and D. A. Huse, *Nature* **388**, 235 (1997).
- [7] P. Bolhuis and D. Frenkel, *J. Chem. Phys.* **106**, 668.
- [8] C. P. Royall, M. E. Leunissen, A.-P. Hynninen, M. Dijkstra, and A. van Blaaderen, *J. Chem. Phys.* **124**, 244706 (2006).
- [9] D. Frenkel and B. Smit. *Understanding molecular simulation: from algorithms to applications*. Academic Press, (2002).
- [10] D. J. Courtemanche and F. van Swol, *Phys. Rev. Lett.* **69**, 2078 (1992).
- [11] D. J. Courtemanche, T. A. Pasmore, and F. van Swol, *Mol. Phys.* **80**, 861 (1993).
- [12] M. Dijkstra, *Phys. Rev. Lett.* **93**, 108303 (2004).
- [13] M. Schmidt and H. Löwen, *Phys. Rev. Lett.* **76**, 4552 (1996).
- [14] A. Fortini and M. Dijkstra, *J. Phys. Cond. Matt.* **18**, L371 (2006).
- [15] M. Heni and H. Löwen, *J. Phys. Cond. Matt.* **13**, 4675 (2001).
- [16] A. van Blaaderen, R. Ruel, and P. Wiltzius, *Nature* **385**, 321 (1997).
- [17] J. P. Hoogenboom, A. K. van Langen-Suurling, J. Romijn, and A. van Blaaderen, *Phys. Rev. Lett.* **90**, 138301 (2003).
- [18] J. P. Hoogenboom, A. K. van Langen-Suurling, J. Romijn, and A. van Blaaderen, *Phys. Rev. E* **69**, 51602 (2004).
- [19] T. Biben, J. P. Hansen, and J. L. Barrat, *J. Chem. Phys.* **98**, 7330 (1993).
- [20] T. Biben, R. Ohnesorge, and H. Löwen, *Europhys. Lett.* **28**, 665 (1994).
- [21] D. C. Hong, *Phys. A* **271**, 192 (1999).
- [22] J. A. Both and D. C. Hong, *Phys. Rev. E* **64**, 061105 (2001).
- [23] W. Nuesser and H. Versmold, *Mol. Phys.* **96**, 893 (1999).
- [24] A. Mori, S. ichiro Yanagiya, Y. Suzuki, T. Sawada, and K. Ito, *J. Chem. Phys.* **124**, 174507 (2006).
- [25] H. Chen and H. Ma, *J. Chem. Phys.* **125**, 024510 (2006).
- [26] S. C. Kim and S. H. Suh, *J. Phys. Cond. Matt.* **15**, 6617 (2003).
- [27] R. Piazza, T. Bellini, and V. Degiorgio, *Phys. Rev. Lett.* **71**, 4267 (1993).
- [28] M. A. Rutgers, J. H. Dunsmuir, J.-Z. Xue, W. B. Russel, and P. M. Chaikin, *Phys. Rev. B* **53**, 5043 (1996).
- [29] J. P. Hoogenboom, P. Vergeer, and A. van Blaaderen, *J. Chem. Phys.* **119**, 3371 (2003).

- [30] S. Hachisu and K. Takano, *Adv. Coll. Int. Sci.* **16**, 233 (1982).
- [31] R. Evans, *Adv. Phys.* **28**, 143 (1979).
- [32] M. Heni and H. Löwen, *Phys. Rev. Lett.* **85**, 3668 (2000).
- [33] Y. Levin, *Phys. A.* **287**, 100 (2000).
- [34] R. J. Speedy, *J. Phys. Cond. Matt.* **10**, 4387 (1998).
- [35] A. van Blaaderen, R. Ruel, and P. Wiltzius, *Nature* **385**, 321 (1997).
- [36] J. E. G. J. Wijnhoven and W. L. Vos, *Science* **281**, 802 (1998).
- [37] P. V. Braun, R. W. Zehner, C. A. White, M. K. Weldon, C. Kloc, S. S. Patel, and P. Wiltzius, *Adv. Mater.* **13**, 721 (2001).
- [38] A. A. Zakhidov, R. H. Baughman, Z. Iqbal, C. Cui, I. Khayrullin, S. O. Dantas, J. Marti, and V. G. Ralchenko, *Science* **282**, 897 (1998).
- [39] M. Holgado, F. Garcia-Santamaria, A. Blanco, M. Ibisate, A. Cintas, H. Miguez, C. J. Serna, C. Molpeceres, J. Requena, A. Mifsud, F. Meseguer, and C. Lopez, *Langmuir* **15**, 4701 (1999).
- [40] A. Blanco, E. Chomski, S. Grabtchak, M. Ibisate, S. John, S. W. Leonard, C. Lopez, F. Meseguer, H. Miguez, J. P. Mondia, et al., *Nature* **405**, 437 (2000).
- [41] D. J. Tildesley and W. B. Streett, *Mol. Phys.* **41**, 85 (1980).
- [42] S. J. Smithline, S. W. Rick, and A. D. J. Haymet, *J. Chem. Phys.* **88**, 2004 (1988).
- [43] J. D. McCoy, S. J. Singer, and D. Chandler, *J. Chem. Phys.* **87**, 4853 (1987).
- [44] C. Vega, E. P. A. Paras, and P. A. Monson, *J. Chem. Phys.* **96**, 9060 (1992).
- [45] C. Vega, E. P. A. Paras, and P. A. Monson, *J. Chem. Phys.* **97**, 8543 (1992).
- [46] C. Vega and P. A. Monson, *J. Chem. Phys.* **107**, 2696 (1997).
- [47] V. N. Manoharan, M. T. Elsesser, and D. J. Pine, *Science* **301**, 483 (2003).
- [48] G. R. Yi, V. N. Manoharan, E. Michel, M. T. Elsesser, S. M. Yang, and D. J. Pine, *Adv. Mater.* **16**, 1204 (2004).
- [49] C. M. Liddell and C. J. Summers, *Adv. Mater.* **15**, 1715 (2003).
- [50] P. M. Johnson, C. M. van Kats, and A. van Blaaderen, *Langmuir* **21**, 11510 (2005).
- [51] R. Biswas, M. M. Sigalas, G. Subramania, and K.-M. Ho, *Phys. Rev. B* **57**, 3701 (1998).
- [52] Z.-Y. Li, J. Wang, and B.-Y. Gu, *J. Phys. Soc. Jpn.* **67**, 3288 (1998).
- [53] Y. Xia, B. Gates, and Z. Y. Li, *Adv. Mater.* **13**, 409 (2001).
- [54] K. W. Wojciechowski, D. Frenkel, and A. C. Brańka, *Phys. Rev. Lett.* **66**, 3168 (1991).
- [55] K. W. Wojciechowski, *Phys. Rev. B* **46**, 26 (1992).
- [56] A. C. Brańka and K. W. Wojciechowski, *Mol. Phys.* **56**, 1419 (1985).
- [57] K. W. Wojciechowski, *Physics Letters A* **122**, 377 (1987).
- [58] C. Vega and L. G. MacDowell, *J. Chem. Phys.* **114**, 10411 (2001).
- [59] S. C. Mau and D. A. Huse, *Phys. Rev. E* **59**, 4396 (1999).
- [60] A. D. Bruce, N. B. Wilding, and G. J. Ackland, *Phys. Rev. Lett.* **79**, 3002 (1997).

- 
- [61] A. D. Bruce, A. N. Jackson, G. J. Ackland, and N. B. Wilding, Phys. Rev. E **61**, 906 (2000).
- [62] A. Fortini, M. Dijkstra, M. Schmidt, and P. P. F. Wessels, Phys. Rev. E **71**, 051403 (2005).
- [63] J. F. Nagle, Phys. Rev. **152**, 190 (1966).
- [64] S. J. Singer and R. Mumaugh, J. Chem. Phys. **93**, 1278.
- [65] M. Parrinello and A. Rahman, Phys. Rev. Lett. **45**, 1196 (1980).
- [66] C. Vega, L. G. MacDowell, C. McBride, F. J. Blas, A. Galindo, and E. Sanz, J. Mol. Liq. **113**, 37 (2004).
- [67] C. Radin and L. Sadun, Phys. Rev. Lett. **94**, 015502 (2005).
- [68] H. Koch, C. Radin, and L. Sadun, Phys. Rev. E **72**, 016708 (2005).
- [69] S. V. Savenko and M. Dijkstra, Phys. Rev. E **70**, 051401 (2004).
- [70] J. D. Bernal and I. Fankuchen, J. Gen. Physiol. **25**, 111 (1941).
- [71] S. Fraden, G. Maret, D. L. D. Caspar, and R. B. Meyer, Phys. Rev. Lett. **63**, 2068 (1989).
- [72] E. B. Mock, H. De Bruyn, B. S. Hawkett, R. G. Gilbert, and C. F. Zukoski, Langmuir **22**, 4037 (2006).
- [73] E. B. Mock and C. F. Zukoski, Langmuir **23**, 8760 (2007).
- [74] M. Heni and H. Löwen, Phys. Rev. E **60**, 7057 (1999).
- [75] R. L. Davidchack and B. B. Laird, Phys. Rev. Lett. **85**, 4751 (2000).
- [76] Y. Mu and X. Song, Phys. Rev. E. **74**, 031611 (2006).
- [77] V. W. A. de Villeneuve. *Structure and Dynamics at Colloidal Boundaries*. PhD thesis, Utrecht University, (2008).
- [78] R. P. A. Dullens, D. G. A. L. Aarts, and W. K. Kegel, Proc. Natl. Acad. Sci. **103**, 529 (2006).
- [79] B. Widom, J. Chem. Phys. **39**, 2808 (1963).
- [80] S. Pronk and D. Frenkel, J. Chem. Phys. **110**, 4589 (1999).
- [81] J. P. Hoogenboom, D. Derks, P. Vergeer, and A. van Blaaderen, J. Chem. Phys. **117**, 11320 (2002).
- [82] S. Auer and D. Frenkel, J. Phys. Cond. Matt. **14**, 7667 (2002).
- [83] A. Jaster, Phys. Rev. E **59**, 2594 (1999).
- [84] S. Sengupta, P. Nielaba, and K. Binder, Phys. Rev. E. **61**, 6294 (2000).
- [85] K. M. Rabe, M. Dawber, C. Lichtensteiger, C. H. Ahn, and J.-M. Triscone. Modern physics of ferroelectrics: Essential background. In *Physics of Ferroelectrics*, pages 1–30. Springer Berlin / Heidelberg, (2007).
- [86] M. Ricci, R. Berardi, and C. Zannoni, Soft Matter **4**, 2030 (2008).
- [87] M. Sawamura, K. Kawai, Y. Matsuo, K. Kanie, T. Kato, and E. Nakamura, Nature **419**, 702 (2002).
- [88] B. Xu and T. M. Swager, J. Am. Chem. Soc. **115**, 1159 (1993).
- [89] J. Malthete and A. Collet, J. Am. Chem. Soc. **109**, 7544 (1987).
- [90] C. D. Simpson, J. Wu, M. D. Watson, and K. Müllen, J. Mater. Chem. **14**, 494 (2004).

- 
- [91] C. I. Zoldesi, C. A. van Walree, and A. Imhof, *Langmuir* **22**, 4343 (2006).
  - [92] C. Quilliet, C. Zoldesi, C. Riera, A. van Blaaderen, and A. Imhof, *Eur. Phys. J. E* **27**, 13 (2008).
  - [93] T. Higuchi, H. Yabu, and M. Shimomura, *Colloids Surf. A* **284**, 250 (2006).
  - [94] Y. Lu, Y. Yin, and Y. Xia, *Adv. Mater.* **13**, 34 (2001).
  - [95] J. A. C. Veerman and D. Frenkel, *Phys. Rev. A* **45**, 5632 (1992).
  - [96] M. A. Bates and D. Frenkel, *Phys. Rev. E* **57**, 4824 (1998).
  - [97] L. Filion, M. A. T. Marechal, F. Smalenburg, and M. Dijkstra. Prediction of crystal structures in isotensial ensembles. submitted to *Phys. Rev. Lett.*
  - [98] B. M. I. Van der Zande, G. J. M. Koper, and H. N. W. Lekkerkerker, *J. Chem. Phys. B* **103**, 5754 (1999).
  - [99] R. Eppenga and D. Frenkel, *Mol. Phys.* **52**, 1303 (1984).
  - [100] A. Cuetos and B. Martinez-Haya, *J. Chem. Phys.* **129**, 214706 (2008).
  - [101] P. D. Duncan, M. Dennison, A. J. Masters, and M. R. Wilson, *Phys. Rev. E* **79**, 031702 (2009).
  - [102] S.-D. Zhang, P. A. Reynolds, and J. S. van Duijneveldt, *J. Chem. Phys.* **117**, 9947 (2002).
  - [103] M. P. B. Van Bruggen, F. M. Van der Kooij, and H. N. W. Lekkerkerker, *J. Phys. Cond. Matt.* **8**, 9451 (1996).
  - [104] F. M. Van der Kooij and H. N. W. Lekkerkerker, *J. Chem. Phys. B* **102**, 7829 (1998).
  - [105] F. M. van der Kooij, K. Kassapidou, and H. N. W. Lekkerkerker, *Nature* **406**, 868 (2000).
  - [106] D. van der Beek, T. Schilling, and H. N. W. Lekkerkerker, *J. Chem. Phys.* **121**, 5423 (2004).
  - [107] M. Wojcik and K. E. Gubbins, *Mol. Phys.* **53**, 397 (1984).
  - [108] T. Boublik and I. Nezbeda, *Collect. Czech. Chem. Commun.* **51**, 2301 (1986).
  - [109] W. R. Cooney, S. M. Thompson, and K. E. Gubbins, *Mol. Phys.* **66**, 1269 (1989).
  - [110] J. Šedlbauer, S. Labík, and A. Malijevský, *Mol. Phys Phys Rev E* **49**, 3179 (1991).
  - [111] M. J. Maeso, J. R. Solana, and J. Amoros, *Mater. Chem. Phys.* **33**, 134 (1993).
  - [112] B. M. Mulder, *Mol. Phys.* **103**, 1411 (2005).
  - [113] F. Gamez, S. Lago, B. Garzon, P. J. Merkling, and C. Vega, *Mol. Phys.* **106**, 1331 (2008).
  - [114] A. Cuetos and B. Martinez-Haya. private communications, (2009).
  - [115] L. H. de la Peña, R. van Zon, J. Schofield, and S. B. Opps, *J. Chem. Phys.* **126**, 074105 (2007).
  - [116] A. Gavezzotti and G. R. Desiraju, *Acta Crystallogr. Sec. B* **44**, 427 (1988).



# Summary

In this thesis we studied the phase behavior of anisotropically shaped (i.e. nonspherical) colloids using computer simulations. Because we were interested in the effects of shape alone, only hard-core interactions between the colloids were taken into account. In the introductory first chapter, we first gave a general introduction on colloids. Then we remarked that the number of different shapes that can be achieved in the synthesis of colloids has grown spectacularly in recent years, and that with these new nonspherical shapes, new phase behavior, such as liquid crystals, is found. In the remainder of Chap. 1, we introduced computer simulations and briefly discuss the two most common types of simulations that can be used to simulate hard particles. We also briefly introduce the free energy methods that we employ to calculate the regions of stability for most of the systems in this thesis.

Gravity is often non-negligible for the relatively large colloids that can be observed using a confocal microscope. Although this thesis is about anisotropic colloids, we first studied the crystallization of hard spheres in the presence of a gravitational field in Chap. 2. In previous work, discontinuous crystallization of the first few layers was found to occur, while the subsequent growth of the number of crystalline layers proceeded continuously as the gravity was increased. We showed that the same behavior is obtained when the chemical potential (or number of particles per unit area) is increased. Furthermore, a simple expression for the chemical potential at which a certain layer crystallizes was shown to quantitatively describe the results from the simulations. We also measured the lattice constant of the crystal and showed that the particles are spaced further apart than one would expect on the basis of the bulk crystal at the same chemical potential (even if the latter is averaged over the entire crystal).

The simplest anisotropic molecule imaginable is a dimer, such as nitrogen. The colloidal equivalents of dimers are the dumbbells, that consist of two overlapping spheres. In chapter 3, we investigated two crystal phases of dumbbells with intrinsic disorder: the plastic crystal and the aperiodic crystal. For almost spherical dumbbells, we showed using multicanonical Monte Carlo simulations (MCMC) that the stable plastic crystal is of the face-centered cubic (FCC) type, as is the case for spheres. However, the hexagonal close packed (HCP) type of plastic crystal phase becomes stable as the aspect ratio increases only slightly, especially at large densities. Using Einstein integration it was shown that the free energy difference between the two types of stacking can be up to 25 times larger than the (absolute) free energy difference between the FCC and HCP crystals of hard spheres (which is only  $10^{-3} k_B T$  per particle). For the aperiodic crystal, we first calculated the degeneracy using a method related to MCMC and confirmed an earlier theoretical result, which was obtained using a series expansion. We used this result and the results of free energy calculations to determine the region of stability of the aperiodic crystal phase and showed that this region is not very large. To enable the system to equilibrate the configuration of bonds, we implemented a bond switch move. The region of stability that was obtained using simulations that included these moves is somewhat larger than the region that was obtained without bond switch moves.

The simulations of the previous chapters were combined in Chap. 4 to simulate hard dumbbells in gravity. The rich phase behavior of the bulk phase diagram, manifests itself in the structure of the sediment of hard dumbbells, which is fluid on top, aligned crystal (CP1) at the bottom and possibly a plastic crystal or an aperiodic phase in between. We investigated the order of the crystallization transitions of the various crystals and showed that apart from the aligned crystal, the hard sphere behavior is recovered. The simple expression that was posed in Chap. 2 to describe the chemical potential at which a certain layer crystallizes was shown to describe our results reasonably well, except for the freezing of the orientational degrees of freedom in the plastic crystal–CP1 transition. Finally, we studied the type of plastic crystal that forms in gravity and showed that the preference for HCP for notably nonspherical dumbbells can be observed directly in a sediment. We wrote down an expression based on the bulk free energy difference that qualitatively described the number of HCP layers compared to the number of FCC layers.

In Chap. 5, we studied bowl-shaped colloids in the form of collapsed shells. It was shown that these colloids form long curved stacks in the fluid at high density (the worm-like phase). We implemented an algorithm for the overlap between two model bowls (as described in the appendix of Chap. 5), which share the features of the colloidal bowls that are important for the phase behavior. We showed that the experimental stack distribution is similar to the distribution from simulations of model particles that have a similar bowl thickness as the experimental particles. For thinner bowls the stacks align and order hexagonally to form a columnar phase at high pressure. As the colloidal bowls remained arrested in the worm-like phase, we studied the crystallization of bowls using only simulations. The columnar phase was shown to be stable for bowls that are thinner or equally thick as the experimental bowls, showing that the worm-like phase, as observed in the experiments (and in our simulations that were started from a fluid), is metastable. We calculated the free energies of the columnar phase where all particles point in the same direction and the columnar phase with alternating orientations and showed that the free energy difference is very small, although the fully aligned columnar phase is favored.

The last shape that is studied in this thesis is a platelet. Usually, platelets are described using a so-called cut sphere, a model particle which has sharp edges or cusps. In Chap. 6, we investigate the phase behavior of cusp-free platelets, which are expected to better describe both colloidal platelets and disk-like molecules. We found two candidate crystal phases using the method described in Chap. 6: one crystal is the equivalent of the stable crystal of cut spheres, while the other crystal is reminiscent of the crystal that is often observed for disk-like molecules at low temperatures. The latter crystal is not stable for cut spheres. Cut spheres have been shown to form a fluid-like phase with cubatic orientational order. We show that, although our particles do form such a phase, the cubatic phase always slowly transforms into the columnar phase. The phase diagram is calculated using free energy methods and compared to that of cut spheres. While the general shape of the phase diagram is the same (except of course for the additional crystal phase and the absence of the cubatic phase in our phase diagram), the positions of the phase boundaries are sensitive to the precise shape of the particle. We also compared our results to the previous work on the same particles where direct simulations were used to determine the phase boundaries. The difference is shown to be large for the strongly first order phase transitions (i.e. the isotropic or nematic fluid to crystal transitions).

# Samenvatting voor een breder publiek

In dit proefschrift wordt het fase gedrag van anisotrope (dwz. niet-bolvormige) colloïden bestudeert door middel van computersimulaties. In deze samenvatting zal allereerst een poging gedaan worden om de woorden colloïden, fase gedrag en computersimulaties uit te leggen, voordat we overgaan tot de daadwerkelijke samenvatting van dit proefschrift.

Colloïden zijn deeltjes die beduidend groter zijn dan atomen, maar wel zo klein dat ze niet met het blote oog zichtbaar zijn, zelfs niet met een vergrootglas. De deeltjes waar mijn collega's experimenten aan doen bijvoorbeeld, zijn ongeveer honderd keer zo klein als de dikte van een gemiddelde menselijke haar. Dit is groot genoeg om ze waar te nemen met een microscoop, die gewoon met zichtbaar licht werkt. Een verdere eigenschap van colloïden is dat ze altijd in een vloeistof (bijv. water) zweven. Zo'n combinatie van zwevende colloïden in een vloeistof wordt een colloïdale suspensie genoemd. Voorbeelden van zo'n colloïdale suspensie zijn melk, latex verf en bloed, waar de colloïden respectievelijk vetbolletjes, latex bolletjes en rode bloedcellen zijn. Zoals deze voorbeelden laten zien zijn de meeste colloïden bolvormig, maar niet allemaal.

In 1827 nam de botanist Robert Brown pollen waar, die op een willekeurige manier leken rond te bewegen, alsof ze levend waren. Hij liet zien dat stofdeeltjes, die zeker niet levend zijn, ook hetzelfde gedrag vertonen. Als dit gedrag dus niet door leven werd veroorzaakt, waar door dan wel? Albert Einstein beargumenteerde dat de atomen in de vloeistof, waar de colloïden in zweven, tegen de colloïden op botsen. Voor een klein genoeg deeltje kan het voorkomen dat er merkbaar meer atomen aan een kant tegen de colloïd opbotsen dan aan de andere kant. Dit verschil wordt veroorzaakt door de willekeurige bewegingen van de atomen, en veroorzaakt dus ook een willekeurige verplaatsing van de colloïd. Deze willekeurige verplaatsingen hebben tot gevolg dat de colloïden zich in zekere zin gedragen als grote atomen. Ter illustratie beschrijven wij een experiment van Jean Perrin in de introductie van dit proefschrift (hoofdstuk 1). Dit experiment laat zien dat de suspensie van colloïden in het altijd aanwezige zwaartekrachtsveld op vergelijkbare manier ijler wordt op grotere hoogte als de lucht in de atmosfeer. Het grote verschil is dat zoals gezegd colloïden veel groter en dus zwaarder zijn dan luchtmolekulen. Ander belangrijk gedrag van atomen is dat ze in verschillende fases kunnen voorkomen, zoals vloeibaar, gasvormig en vast. Dit zogenaamde fasegedrag vertonen colloïden ook, maar dan op een schaal die waargenomen kan worden met een licht microscoop. De analogie met colloïden stelt ons dus in staat om experimenten te doen aan atomaire fases, die met atomen niet mogelijk zijn.

In de wetenschap worden, als het goed is, experimenten altijd ondersteund door theorie, die dan weer bewezen of ontkracht wordt met behulp van experimentele resultaten. Het onderscheid tussen de twee was traditioneel altijd heel duidelijk: experimenten werden in het lab gedaan en theorie op papier. Met de komst van (steeds snellere) computers is deze situatie een beetje gewijzigd. Allereerst moeten theoretici steeds vaker computers gebruiken om hun vergelijkingen op te lossen en zijn veel experimentele wetenschappers vaak minstens evenveel tijd bezig om hun data op de computer te analyseren als ze daadwerkelijk in het lab aan het meten zijn. Maar ook is er een derde soort wetenschap gekomen, die

een beetje tussen theorie en experimenten instaat: de zogenaamde computersimulaties. Hierbij wordt allereerst de beweging van een deeltje met een basale theorie beschreven, bijv. een deeltje voelt een kracht van rechts en beweegt dus naar links met een bepaalde snelheid. Vervolgens worden veel (100-100000) van dit soort deeltjes in de computer geprogrammeerd en worden interacties tussen de deeltjes in het programma voorgeschreven. Het programma wordt daarna gedraaid op de computer en de veranderende posities en/of snelheden en krachten van de deeltjes worden gemeten, alsmede andere daarvan afgeleide eigenschappen. Het voordeel van simulaties boven experimenten is dat ze soms sneller en in ieder geval goedkoper zijn: geavanceerde experimentele opstellingen kunnen makkelijk meer dan honderd keer duurder zijn dan de computers, waar de meeste simulaties op gedaan worden. Bij het bedrijven van pure theorie zijn vaak ingrijpende benaderingen nodig om oplosbare vergelijkingen te krijgen, terwijl bij de basale theorie, die in computersimulaties gebruikt wordt, veel minder benaderingen gedaan worden. Daarom zijn de resultaten van computer simulaties vaak betrouwbaarder dan de resultaten van theorie, mits de simulaties met voldoende zorg uitgevoerd zijn.

Colloïden zijn de droom van een computer simulator, omdat de interacties tussen de colloïden naar harte lust aan te passen zijn. In de inleiding van dit proefschrift (hoofdstuk 1) wordt beschreven hoe colloïden tot een soort zeer kleine knikkers gemaakt kunnen worden, dat wil zeggen: de colloïden worden dan beschreven als harde bollen die verder geen interacties hebben met elkaar. Dit wordt gedaan omdat dit de theorie en simulaties heel veel eenvoudiger maakt. Behalve de interacties, is ook de vorm van de colloïden door recent ontwikkelde geavanceerde scheikundige methoden aan te passen. Zo kunnen colloïden de vorm aannemen van staafjes, schijfjes, kommetjes, dubbele bollen, etc. Het beschrijven van deze deeltjes als enkel harde deeltjes (dwz. geen interacties door lading e.d.) heeft als voordeel dat we puur het effect van de vorm van de deeltjes op het fasegedrag kunnen bekijken. Daarentegen is bij molekulen het effect van de vorm van het deeltje op het fasegedrag vaak lastig te scheiden van het effect van de interacties. Vooral het fasegedrag van zeer lange staafvormige of zeer platte schijfvormige colloïden is zeer anders dan dat van bollen, zoals dit ook voor zeer lange of zeer platte molekulen het geval is. Deze deeltjes kunnen fases vormen die tussen een vloeistof en een kristal fase inzitten, de zogenaamde vloeibare kristallen, zie het plaatje in hoofdstuk 1. Verder worden in hoofdstuk 1 de verschillende soorten computersimulaties in wat meer detail dan hierboven beschreven en worden de zogenaamde vrij energie berekeningen uitgelegd die ons instaat stellen om het fasegedrag precies te bepalen.

Eén eigenschap van colloïden, die lastig is aan te passen, is dat ze door hun grootte vaak ook vrij zwaar zijn (ten opzichte van hetzelfde volume aan vloeistof). Zwaartekracht is dus meestal niet te verwaarlozen in colloïdale systemen. Hoewel dit proefschrift over niet bolvormige deeltjes gaat, bekijken we in hoofdstuk 2 eerst het fasegedrag van harde bollen in zwaartekracht. Hier is al eerder naar gekeken in de literatuur, maar wij poneren in dit hoofdstuk voor het eerst een uitdrukking die de kristallisatie van een bepaalde laag bollen beschrijft in termen van de zogenaamde chemische potentiaal, die gerelateerd is aan het aantal deeltjes in het system. Deze uitdrukking beschrijft de kristallisatie van de lagen, die geobserveerd werd tijdens onze simulaties, vrij goed. Verder hebben we nog de roosterconstante van het uiteindelijke kristal gemeten in onze simulaties en laten zien dat die hoger is dan de roosterconstante van het bulk kristal bij dezelfde chemische potentiaal.

In het volgende hoofdstuk word ons eerste niet-bolvormige colloïd bekeken. Dit deeltje bestaat uit twee bollen, naar analogie van molekulen die uit de twee atomen bestaan. Deze twee bollen worden aan elkaar geplakt en de vorm wordt gevarieerd door een laag van hetzelfde materiaal om de twee bollen heen te groeien. Deze deeltjes worden halters (Engels: dumbbells) genoemd, omdat ze een beetje lijken op de halters die gebruikt worden bij het gewichtheffen (hoewel de bollen niet door een stok verbonden worden). De halters zijn interessant omdat berekeningen hebben aangetoond dat bepaalde kristallen van halters een zogenaamd fotonisch kristal kunnen vormen. Fotonische kristallen zouden een toepassing kunnen hebben in schakelingen die met licht werken, in tegenstelling tot de elektrische schakelingen in een computer. Helaas blijkt dat deze kristallen, die naar analogie van kristallen van atomen verzonnen zijn, niet stabiel te zijn voor harde halters. Zoals is aangetoond in eerder werk, ordenen de halters zich wel in drie andere kristal fases. In de eerste van deze kristalfases, het plastische (vervormbare) kristal, kunnen de halters ronddraaien terwijl ze op roosterposities staan. Wij hebben gekeken naar het specifieke type plastisch kristal wat de halters vormen. Bollen (of sinaasappels bij de groenteboer) kunnen op verschillende manieren gestapeld worden, waar de twee uitersten kubisch vlakgecentreerd (FCC naar het Engelse face-centered cubic) en de hexagonale dichtste pakking (HCP naar hexagonal close packed) zijn. Deze twee types kristalroosters zijn ook mogelijk bij halters: bijna bolvormige halters vormen het FCC type plastic crystal, terwijl langere halters het HCP type vormen. Verder is er nog een kristal (CP1) waarin alle deeltjes dezelfde richting opstaan. Dit kristal is bijna altijd stabiel bij een (zeer) hoge druk. Het laatste kristal is een aperiodisch kristal wat gemaakt kan worden van een kristal van bollen waar de bollen paarsgewijs verbonden worden tot halters op een willekeurige manier. We hebben gekeken naar de competitie van dit aperiodische kristal en het CP1 kristal. Het blijkt dat alleen halters waar maar een kleine laagje over de bollen heen gegroeid is (die dus maar nauwelijks aan elkaar vast zitten) in een aperiodisch kristal kunnen ordenen.

De vorige twee hoofdstukken worden gecombineerd in hoofdstuk 4, waarin halters in zwaartekracht worden bestudeerd. Hierbij is het mogelijk om twee verschillende kristallen en een vloeistof in één systeem te krijgen, doordat de druk afneemt als functie van de hoogte. Op de bodem vormt zich dan CP1, dat ook zonder zwaartekracht stabiel is bij de hoogste drukken. Daarop ligt ofwel een plastisch kristal of een aperiodische kristal en helemaal bovenaan vormen de halters en vloeibare fase. De kristallisatie van de verschillende lagen van deze kristallen werd meestal redelijk beschreven door de uitdrukking die we in hoofdstuk 2 al gebruikten voor de kristallisatie van harde bollen in zwaartekracht. Alleen voor de overgang van het plastische kristal naar CP1 werkte deze uitdrukking niet. We hebben ook in zwaartekracht gekeken naar de formatie van FCC of HCP types van het plastische kristal. Deze resultaten konden althans kwalitatief beschreven worden met behulp van de berekeningen uit hoofdstuk 3.

De volgende twee hoofdstukken gaan over colloïden waarvoor de equivalente molekulen vloeibare kristal fases vormen. Deze fases vinden tegenwoordig vrij veel toepassingen, bijvoorbeeld in LCD schermen. Hoofdstuk 5 gaat over komvormige deeltjes, waarvan de hoop is dat ze opstapelen in rechte kolommen die dan ordenen in een zogenaamde columnaire fase. De colloïdale kommetjes worden gemaakt door een schilletje van een soort latex in te laten klappen. We presenteren zowel experimenten, die door onze collega's

uitgevoerd zijn, als simulaties, zodat een goede vergelijking gemaakt kan worden. In de experimenten vormen de deeltjes wel stapels, maar de stapels zijn gebogen en wijzen niet allemaal in dezelfde richting. In de simulaties gebeurt dit ook, tenzij we vrij diepe kommetjes bekijken, die wel een columnaire fase vormen. Deze diepe kommetjes zijn helaas lastig te maken met de hierboven beschreven methode. Het verdere fasegedrag is alleen bepaald met behulp van computersimulaties, omdat het experimentele systeem vast bleef zitten in de fase met de gebogen stapels. Behalve de columnaire fase en de vloeistof (al dan niet met stapels), zijn er ook nog vier kristal fases, waar de deeltjes in kunnen kristalliseren. Zo is er bijvoorbeeld een kristalfase waar paren van kommetjes bolletjes vormen, die dan een kristal vormen.

Als laatste vorm hebben we schijfjes of plaatjes bestudeerd. Colloïdale plaatjes kunnen op verscheidene manieren gemaakt worden, maar over het algemeen zal een schijfvormige colloïde een glad oppervlak hebben zonder scherpe randen. Het meest gebruikte simulatiemodel is een bol waarvan een boven- en een onderstuk zijn afgesneden. Deze zogenaamde afgesneden bol heeft scherpe randen waar de snijvlakken en de rand van de bol bij elkaar komen. Deze deeltjes worden gebruikt omdat het relatief makkelijk is om ze te simuleren. Wij hebben een ander modeldeeltje bestudeerd wat geen scherpe randen heeft, om te kijken wat het effect is van die scherpe randen op het fase gedrag. Allereerst vonden we een kristal wat niet gevonden is voor afgesneden bollen, maar wel voor schijfvormige molekulen. Deze molekulen hebben ook nog andere interacties dan onze deeltjes, maar we kunnen speculeren dat de kristalfase van de molekulen in ieder geval gedeeltelijk veroorzaakt wordt door hun vorm, die meer op ons deeltje dan op een afgesneden bol lijkt. Verder is er nog een zogenaamde cubatische fase die (mogelijk) stabiel is voor afgesneden bollen, maar die in ons geval overgaat in de columnaire fase, maar alleen na een lange tijd. Het verdere fasegedrag van afgesneden bollen komt in grote lijnen overeen met onze resultaten, behalve dat de kristallisatiedichtheden niet volledig overeenkomen.

# Acknowledgements

Although many people think of a computer scientist as a person working on unintelligible problems at his desk by himself, this thesis is not the work of just one person. First of all, I would like to thank my supervisor Marjolein who has always made time for me, especially during the last few months. Writing this thesis and having my work corrected by Marjolein has taught me a lot about scientific English writing. The last two chapters of this thesis are dedicated to work which was performed in collaboration with others. I thank Arnout for having patience with me when we discussed experimental details about the collapsed shells and Rob for doing the experimental work on the shells (including counting hundreds of colloids by eye). Alejandro asked us to do free energy calculations for the oblate hard spherocylinders, so without him Chap. 6 would not have come to be. I thank him, Bruno and Alessandro for fruitful discussions, and Alejandro for the nice time Jellie and I had in Alm ria. It is a shame that Ahmet and I never really got to combine his experiments and my simulations of dumbbells, but I have occasionally pestered him for experimental properties of his dumbbells. Alfons was not my direct supervisor (although initially, he was to be my promotor), but his remarks during the work discussions always had a positive effect on my work. The fcc versus hcp plastic crystal issue and the fcc<sup>2</sup> phase, for instance, were his suggestions. I thank Niels for the opportunity to supervise him during his M.Sc. project and apologize for not always having read the newest version of his thesis in time. For four years I have been (and still am) a computer simulator that was *not* sitting at his desk by himself, thanks to my room mates, Andrea, who has helped me start up my simulations, Michiel with whom I have shared almost everything during my PhD and Djamel who always kindly put up with my music. Laura, Andrea, Frank, Joost, Ran, and Michiel, I thank you for the many discussions we had about simulations and Teun, Ahmet, Michiel and Rao for discussions about colloids. The SCM group would not function as well as it does, without our secretary Maria (and Eva for a short while). I would also like to thank all current and former members of the SCM group for many coffee breaks and official or unofficial group outings and dinners, that obviously would have been a lot less enjoyable without them: Andrea, Miriam, Astrid, Joan, Carmen, Anti-Pekka, Kristina, Job, Slava, Andy, Alejandro, Eduardo, Esther, Carlos, Peter, Michiel, Teun, Laura, Frank, Ahmet, Rao, Djamel, Michiel, Johan, Dannis, Anke, Joost, Bart, Christina, Marjolein, Ran, Bo, Linh, Stephane and Alessandro. Computer simulations without computers are not really possible, so I would like to thank Henk Mos and Peter Helfferich for fixing marts, printers etc. almost as soon as something was broken.

Although it might seem somewhat surprising that science and sports go well together, I nevertheless enjoyed many games of sport with my colleagues. In that respect, I would like to thank Laura, Peter, Teun, Anke and for never letting me down (at least while wall climbing) and Michiel and Laura for allowing me to win a few games at squash. It has also been good to see other people than my colleagues to take my mind off work, so I owe a debt of gratitude to my former and current fellow band members, wall climbing non-colleagues, and my beach volleyball team. I thank my parents and Ineke, without whom I would not have been the person I am today, and my sister for her kindness and

---

support; Pap, Mam, Ineke, Erica, bedankt! And finally, the most important person in my life, Jellie, thank you for your support, your timely reminders when I was about to forget something and your understanding during the times I worked on my thesis every evening. Although I have no idea where I will be in a few years, I hope you will be with me.

# Curriculum Vitae

I was born in Hilversum (a town 20 km north of Utrecht) on the eleventh of August 1981. I attended primary school at the Vondel School in Hilversum and secondary school at the Comenius College also in Hilversum, where I recieved my high school diploma in 1999. I began my physics and astronomy studies at the Utrecht University the same year. After an initial interest in Astronomy, I finished my combined bachelor and master education at the theoretical institute of physics (ITF) in Utrecht. My M.Sc. project was performed partially at Philips at the High Tech campus in Eindhoven, where I was supervised by Lou Fé Feiner. In the resulting thesis, *Multi-band excitons in nanowires*, I investigated the effects of confinement on excitons in a nanowire. In september 2005, I started my PhD under the supervision of Marjolein Dijkstra at the soft condensed matter group, which resulted in this thesis. Part of my PhD research has been published in scientific journals and was presented as poster and/or oral presentations at national and international conferences. As part of my PhD, I have been a teaching assistant for undergraduate courses in physics and I have supervised a master student on a combined theoretical and simulation project.